TECHNICAL UNIVERSITY OF CRETE

DIPLOMA THESIS

Visualizing blood perfusion through LASER speckle imaging.

Author:
Efstratios Ch. Marinou

Comittee:
Dr. Costas Balas
Dr. George Karystinos
Dr. Konstantinos Giftakis

A thesis submitted in fulfillment of the requirements for the integrated master's degree of Electrical and Computer Engineering

in the

Department of Electrical and Computer Engineering

July 8, 2025

Declaration of Authorship

I, Efstratios Ch. Marinou, declare that this thesis titled, "Visualizing blood perfusion through LASER speckle imaging" and the work presented in it are my own. I confirm that:

- This work was done wholly or mainly while in candidature for an integrated master's degree at this University.
- Where any part of this thesis has previously been submitted for a degree or any other qualification at this University or any other institution, this has been clearly stated.
- Where I have consulted the published work of others, this is always clearly attributed.
- Where I have quoted from the work of others, the source is always given. With the exception of such quotations, this thesis is entirely my own work.
- I have acknowledged all main sources of help.
- Where the thesis is based on work done by myself jointly with others, I have made clear exactly what was done by others and what I have contributed myself.

Signed:

_____

Date:

_____

“ εγώ πάλι άλλοτε κάνω πως κοιμάμαι άλλοτε

πως μαντάρω ένα ζευγάρι κάλτσες παλιές

γιατί έχουν όλα γύρω μου παράξενα παλιώσει ”

Μίλτος Σαχτούρης

TECHNICAL UNIVERSITY OF CRETE

Abstract

Technical University of Crete

Department of Electrical and Computer Engineering

Electrical and Computer Engineering

Visualizing blood perfusion
through LASER speckle imaging.

by Efstratios Ch. Marinou

Laser Speckle Contrast Imaging (LSCI), a specific method within the broader field of Laser Speckle Imaging, is a non-invasive optical technique, able to visualize motion and flow dynamics through the analysis of speckle patterns. These patterns are formed when the sampling surface is illuminated by coherent light and are captured by a CCD sensor. The simplicity and cost-effectiveness of this configuration are the main factors contributed to LSCI's growing popularity in the biomedical field. After the acquisition of the raw speckle frames, image processing is performed to extract local intensity contrast. This contrast is indicative of speckle pattern's decorrelation which, in turn, is related to motion. In fact, through a complex statistical analysis, contrast can be linked to blood flow velocity. Among biomedical applications, blood perfusion imaging is the most prevalent, as it benefits significantly from the technique's real-time and label-free operation. This work is structured in two main parts. First, a general review of speckle metrology and its applications, along with a description on the biological importance of blood perfusion – providing all the essential foundation for the specific experimental section. The second part of the Thesis focuses on the laboratory work which investigates the application of LSCI in two distinct use cases. The primary application is the visualization of blood perfusion, specifically superfisial skin perfusion. While LSCI is widely used for blood flow imaging, its application to skin perfusion is limited by the lack of resolvable vascular structure, which restricts the method's ability to produce vascular maps. For this reason, our system was assessed through well-established occlusion-reperfusion protocol. The secondary use case is a novel application of LSCI: visualizing mechanical oscillations on vibrating membranes. LSCI's sensitivity proved suitable for the visualiazation of stationary field on oscillating drum' membranes, a widely unexplored application in the literature. We completed this part of our research by applying the technique to controlled osccilation of a speaker's membrane providing a semi-quantitative analysis. As per our algorithmic choices, a spatial contrast method (LASCA) was implemented using an open-source toolbox and extended with custom post-processing algorithms. Experimental validation demonstrates that, even with low-cost hardware, LSCI can effectively capture both perfusion trends and dynamic motion. The results highlight the technique's versatility and potential for accessible biomedical and motion analysis applications.

Acknowledgements

Almost one year and a half year since this topic excited me for the first time, after a lot of work and challenges, and just before presenting my master's thesis, I find myself deeply grateful to the people who stood by me and made all of this possible.

First and foremost, I would like to thank my advisor, Prof. Costas Balas, for introducing me to research and guiding me towards exciting topics, as well as for providing his expertise on both the theoretical and practical parameters of this work. I am also greatful to him for granting me access to his company's facilities and equipment, which made the experimental part of this thesis possible. I would like to thank his collaborators as well, who supported me with technical matters and shared their knowledge throughout the process — particularly Gianni Nteroli, a research associate of C. Balas' group at TUC.

I am also thankful to many of my other Professors of TUC for the knowledge and inspiration, they shared among those years. And of course, nothing would have been possible without my family.

To those loved ones who stood by me, inspired me and supported me, near or far, then or now.

Contents

List of Figures

List of Abbreviations

LSCI	**L**aser **S**peckle **C**ontrast **I**maging
LASCA	**La**ser **S**peckle **C**ontrast **A**nalysis
ROI	**R**egion **o**f **I**nterest
LDI	**L**aser **D**oppler **I**maging
MRI	**M**agnetic **R**esonance **I**maging
LSI	**L**aser **S**peckle **I**maging
CNR	**C**ontrast to **N**oise **R**atio
PET	**P**ositron **E**mission **T**omography
ICG	**I**ndo**c**yanine **G**reen Fluorescence Imaging
CCD	**C**harge-**C**oupled **D**evice
CEUS	**C**ontrast-**E**nhanced **U**ltra**s**ound
NIRS	**N**ear-**I**nfra**r**ed **S**pectroscopy
FSM	**F**luorescent **S**peckle **M**icroscopy
HSI	**H**yper**s**pectral **I**maging
ESPI	**E**lectronic **S**peckle **P**attern **I**nterferometry
DSPI	**D**igital **S**peckle **P**attern **I**nterferometry
DIC	**D**igital **I**mage **C**orrelation
THSP	**T**ime **H**istory of the **S**peckle **P**attern
SESP	**S**ingle **E**xposure **S**peckle **P**hotography
LSTCA	**L**aser **S**peckle **T**emporal **C**ontrast **A**nalysis
CC	**C**reative **C**ommons
TUC	**T**echnical **U**niversity of **C**rete

Physical Constants

Plank constant	$h = 6.62607004 \times 10^{-12}\ m^2 kg/s$
Euler's number	$\mathrm{e} \approx 2.71828$
PI	$\pi \approx 3.14159$

General Part

Chapter 1

Laser Physics

1.1 Fundamental Principles in Laser Operation

Understanding light-matter interactions is the first step in developing the theory of laser operation. Two fundamental processes that need to be introduced, are absorption and emission. Let us consider an atom or molecule of a given material with two energy levels E_1, E_2, where $E_1 < E_2$. Assuming that state $n = 1$ with energy E_1, is the ground state, an atom in this state will remain there, unless some form of stimulation is applied. This atom can transition to state $n = 2$ by absorbing thermal radiation with an energy density J and frequency v. The frequency v of the wave, is given by the well-known expression:

$$v = (E_2 - E_1)/h$$

where h is Planck's constant. This phenomenon is called absorption. Additionally, other forms of excitation exist that do not require the absorption of electromagnetic radiation.

On the other hand, let us now assume that the atom is initially in state $n = 2$. Since $E_1 < E_2$, the atom will tend to decay to state $n = 1$, as lower energy states are more stable and thus favorable. During this transition, the energy difference $E_2 - E_1$ must be released by the atom. If this energy is emitted as a photon with a frequency v, such as $v = (E_2 - E_1)/h$, the process is called spontaneous emission. De-excitation can occur either in a radiative way or non-radiatively. Radiative decay, where the energy is released as an electromagnetic wave, is known simply as emission. In non-radiative decay, energy is delivered in some other form, like kinetic or internal energy of the surrounding atoms or molecules.

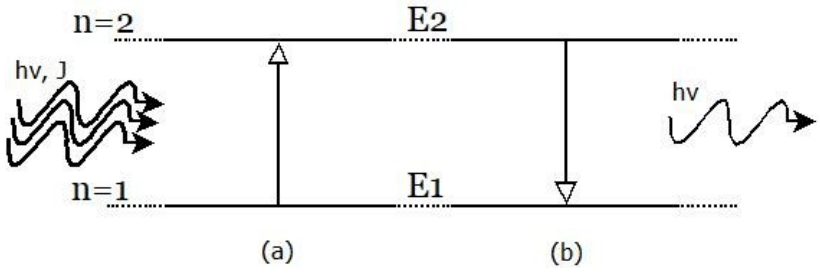

Figure 1.1: Graphical illustration of the process of absorption (a) and emission (b).

Spontaneous emission happens naturally as the electron returns to the lower energy level available. However, let us now suppose that an electromagnetic wave of frequency v corresponding to the energy difference between the two states, is present in the material. There is a finite probability that this radiation will interact with an electron in state $n = 2$ and force it to de-excite to state $n = 1$. This phenomenon is called stimulated emission which is the second way, an emission can occur. In this case, the photon emitted has the same phase, direction and frequency with the stimulating wave. Stimulated emission with its properties introduces the concept of optical amplification (where one photon enters and two photons exit).

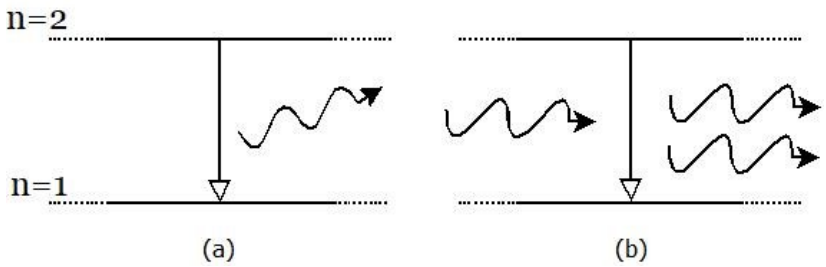

Figure 1.2: Graphical illustration of the process of spontaneous (a) and stimulated (b) emission.

In thermodynamic equilibrium, the excitation rate equals to the de-excitation rate. De-excitation occurs either spontaneously within 10^{-15} to 10^{-8} seconds or is stimulated by the interaction with another photon, as described previously. The probability of stimulated emission and absorption depends on the number of photons with energy equal to the difference between the energy levels. In contrast, spontaneous de-excitation is independent of the presence photons, naturally. In order to calculate the probabilities for these light-matter interaction processes, let us refer to Einstein's approach.

Let N_1, N_2 be the populations of particles existing in the energy states E_1, E_2. The probability of spontaneous emission can be determined by the decay rate of the upper state population, $(\mathrm{d}N_2/dt)_{\mathrm{sp}}$. The decay rate is proportional to the population N_2 and is described by:

$$\left(\frac{\mathrm{d}N_2}{dt}\right)_{\mathrm{sp}} = -A_{21}N_2$$

A_{21} is the Einstein A coefficient, a positive constant value that describes the rate of spontaneous emission. The negative sign accounts for the fact that the population of the energy state decreases over time. Similarly, the coefficients B_{12} and B_{21} describe the rates of absorption and stimulated emission, respectively. All coefficients depend on intrinsic atomic properties. If J is the energy density of the incident radiation (Joule/m³), then the decay rate from Energy level 2 to level 1, due to stimulation from a photon is:

$$\left(\frac{\mathrm{d}N_2}{dt}\right)_{\mathrm{st}} = -JB_{21}N_2$$

And the rate of the transitions from level 1 to level 2, due to absorption:

$$\left(\frac{\mathrm{d}N_1}{dt}\right)_{\mathrm{a}} = -JB_{12}N_1$$

JB_{12} and JB_{21} are the probabilities of excitation and stimulated de-excitation and depend on the energy density of the electromagnetic radiation.

In state of thermal equilibrium, the rate of absorption from level 1 to level 2 is equal to the decay rates from level 2 to level 1 combined. This is due to the population distribution remaining stable over time, thus the following holds:

$$JB_{12}N_1 = A_{21}N_2 + JB_{21}N_2 \Leftrightarrow J = \frac{N_2A_{21}}{N_1B_{12} - N_2B_{21}} \Leftrightarrow J = \frac{A_{21}}{\frac{N_1}{N_2}B_{12} - B_{21}} \quad (1)$$

Furthermore, it was shown by Einstein that if two levels are non-degenerate, then

$$B_{12} = B_{21}$$

If two energy levels are non-degenerate, each level corresponds to a single quantum state rather than multiple states with the same energy. In this case, probability of a photon interacting with an electron of either energy, to excite or de-excite it, is the same.

An important function to this analysis is Boltzmann's relation. This is a function that describes the population ration of our particles in the two energy states. According to the relation:

$$\frac{N_1}{N_2} = e^{-(E_2 - E_1)/KT} \quad (2)$$

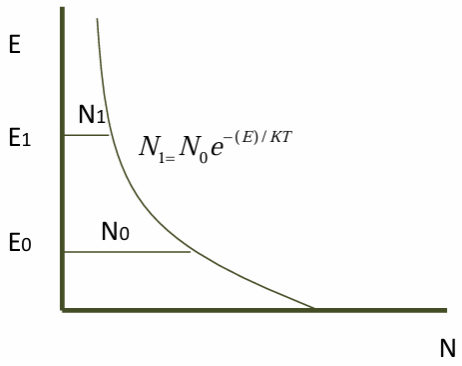

Figure 1.3: Graphical presentation of energy level population as a function of energy

Using Boltzmann's relation (2) and $B_{12} = B_{21}$, we obtain:

$$J = \frac{A_{10}}{e^{(E_2-E_1)/KT}B_{12} - B_{21}} = \frac{A_{21}}{e^{\mathrm{hv}/KT}B_{21} - B_{21}}$$

$$\frac{JB_{21}}{A_{21}} = \frac{1}{e^{\mathrm{hv}/KT} - 1}$$

The final relationship describes the ratio of stimulated to spontaneous emission probabilities. For typical light sources, the ratio is typically very small. Thus, in thermal equilibrium, the spontaneous emission mechanism dominates.

Laser's operating principle is based on the stimulated emission of photon packets. From the previous analysis, a question as to how the stimulated emission mechanism can dominate over spontaneous emission, arises. This appears to require population inversion of electrons in the energy states involved.

Equation (1) holds from the fact that stimulated excitation follows the same rate as the combined de-excitation (stimulated and spontaneous). As a consequence, the probability of emission would be always higher than the probability of absorption, when only two energy states are involved. Thus, lasing cannot take place, using a system of two energy levels because population inversion would be impossible.

In contrast, it is proven that a system of three or more energy states enable population inversion phenomenon. However, this requires a state with a long lifetime involved that provides longer spontaneous de-excitation periods than the common 10^{-15} seconds mentioned. Having enough time before the spontaneous emission occurs, is crucial in order to gather a large number of electrons on an excited state before they are triggered by the first de-excitation, resulting in a chain effect of packets of photons being released at the same time. This phenomenon is the essence of a laser's operation. Such long lifetime before the de-excitation can be observed in metastable states. A transition between energy levels is allowed when conservation principles of energy are satisfied. When Momentum, Angular Momentum, Spin, or Parity are not appropriate, the transition is forbidden and the probability of the transition is approaching zero, while the transition time theoretically goes towards infinity. In reality, though, such transitions are possible and their life time is relatively long. These states are called metastable. Typical metastable states are when a transition from singlet to a triplet state takes place.

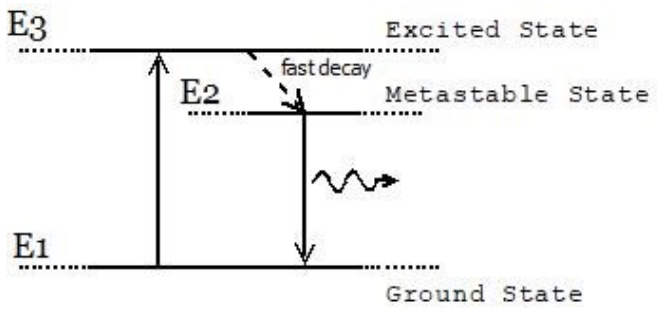

Figure 1.4: Jablonski Diagram of a 3-energy state laser system

As described on the diagram, photons or another means of stimulation, induce the excitation of electrons to the excited state. Shortly after, electrons rapidly de-excite from level 3 to the metastable state (level 2), spontaneously, releasing energy as photons or heat. Since level 2 is metastable, electrons remain there for a significantly longer period. As a large number of electrons follow, they accumulate, until population inversion is succeeded. When the first electron spontaneously transitions from level 2 to the ground state 1, it emits a photon with frequency v_{10}. As previously mentioned this photon can stimulate the emission of additional photons, trigerring a chain reaction of stimulated emission that initiates the lasing process. This bunch of photons have identical phase and frequency v_{10}, corresponding to the energy difference between the two levels.

1.2 Laser Pumping

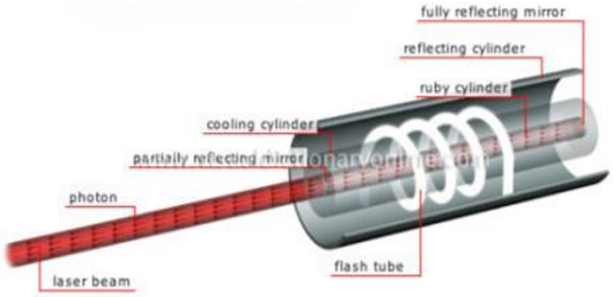

Figure 1.5: Optical pumping Illustration

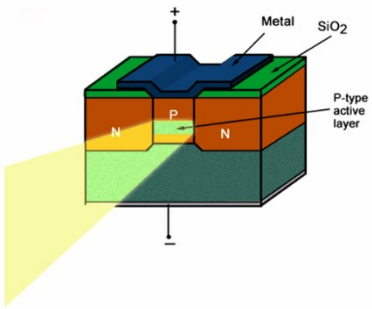

Figure 1.6: Electrical pumping illustration

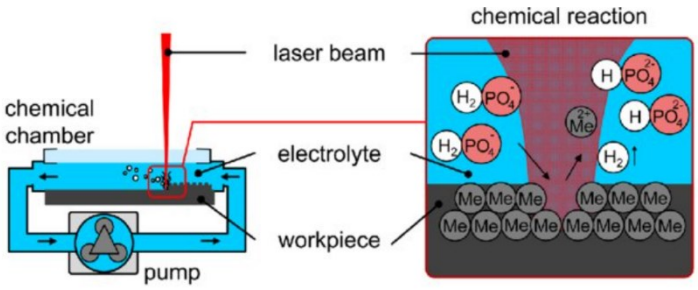

Figure 1.7: Chemical pumping Illustration [Reproduced from [1], under CC BY 4.0]

Pumping is called the procedure of exciting an active medium, through external energy supply, to produce light emission. The three different types of pumping are photo, electro and chemi-luminescence. Photo-luminescence refers to population excitation of atoms to higher energy levels through photon absorption. To this category Gas and some semiconductor lasers apply. Electro-luminescence refers to excitation through energy transfer via collisions or resonant energy transfer. This category includes arc discharge (excimer lasers - collisional excitation) and carrier injection (diode lasers – voltage application to p-n junction). Lastly, chemi-luminescence involves excitation of

atom populations through chemical bonding with metastable derivatives or derivatives in higher energy states. lasers that fall in this category are usually high-powered, such as Chemical Oxygen-Iodine and HF lasers, produced by achieving chemical bonding to emit photons.

Beyond their excitation method, lasers can also be categorized based on other important parameters. The active medium's state categorizes lasers by the three main states: solid, gas and liquid. However, hybrid systems can also be found, such as laser diode light being used to pump other lasers (diode-pumped solid-state lasers). Another form of categorizing is by emission mode. A laser can be either continuous wave (C.W.) or Pulsed, with pulse duration varying from femtoseconds (10^{-15}) to nanoseconds.

lasers can be designed with various advancements and optimizations in their engineering. Regardless, all lasers fundamentally rely on three main features: an active medium, an optical resonator and a means of excitation. The active medium requires at least three or more transition levels exploitable, with one acting as a metastable state. The optical resonator (cavity) is typically constructed with a reflective and a semi-reflective mirror. The active medium is required to be placed inside. The means of excitation simply involves a way to excite the particles of the active medium to the higher energy levels needed for the process.

1.3 Laser diode

The laser diode is one of the most commonly used, if not the most common in recent years. This section will go into detail in the specifications of laser diodes, as it was also the type of lasers that was utilized for the laboratory work of this Thesis. Their popularity is mainly due to their cost-effectiveness, small size and efficiency, making them the best option for a number of applications, including medical diagnosis.

Laser diodes are made of a semi-conductor junction, from which they inherit their other name (semi-conductor laser). One of the simplest laser diodes are made from GaAs (Gallium – Arsenide) but more complex compositions of semiconductors are usual, such as GaAlAs, InGaAs, InGaAsP. The composition, determines the emission wavelength as it is defined by the width of the energy bandgap. One of the main reasons why, semiconductor lasers are so popular is because of the flexibility on the emitting wavelength. The P-N layers are created using doping techniques that adjust the material's properties and alter the bandgap of the semiconductor to achieve emission at various wavelengths. In ternary (three element conjunction) and quaternary (four element) semiconductor compositions such as AlxGa1-xAs (Aluminum – Gallium – Arsenide), the bandgap transition energy (thus photon energy) can be adjusted with alternating doping ratios.

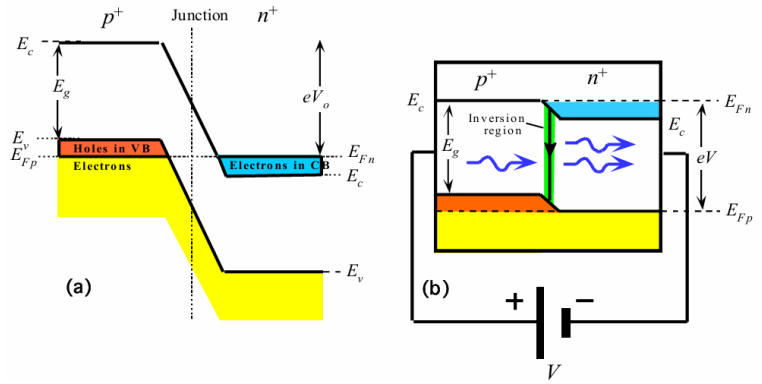

Figure 1.8: a. The potential barrier without diode biasing. b. Under forward bias, with current flowing, the barrier is reduced. Due to the applied potential, electrons transition to a higher energy state, and within a narrow region on either side of the junction (green line), population inversion occurs.

But how pumping work in laser diodes? In most cases, laser diodes excitation occurs through carrier injection, meaning that the semiconductor is forward biased by external voltage. When current flows through, the potential barrier at the p-n junction gets reduces and electrons from the n-region proceed into the conduction band, while holes from the p-region move into the valence band.

Electrons accumulate until the phenomenon result in population inversion, that is needed to operate a laser. At this part of the process, if a photon, of bandgap energy, happens to enter the junction region, it cannot excite an electron from the valence band to the conduction band; Simply because there would be no electrons present at this region.

Photons of suitable energy will stimulate the transition of electrons from the conduction band back to valence band, where they get recombined with a hole. In direct bandgap semiconductors, electrons in the conduction band directly recombine with holes in the valence band, with photons of bandgap energy, being emitted. This is a process called radiative recombination and it is highly efficient in semiconductor lasers like GaAs, which is widely used. In comparison, indirect bandgap semiconductors like silicon are not suitable. This is because direct photon emission is inefficient and electron transitions between bands require assistance.

An important detail worth noting at this point, is that some photons, interact with electrons of the conduction band and excite them to higher energy states. However, these electrons quickly de-excite to lower energy conduction band states, with emission of heat or photons. In the meantime, the holes created in the valence band move toward the higher valence band states. This is when the chain effect of emission begins with a spontaneous emission that quickly escalates, to the amplification of an optical wave at the corresponding frequency. This process is described by the following diagram.

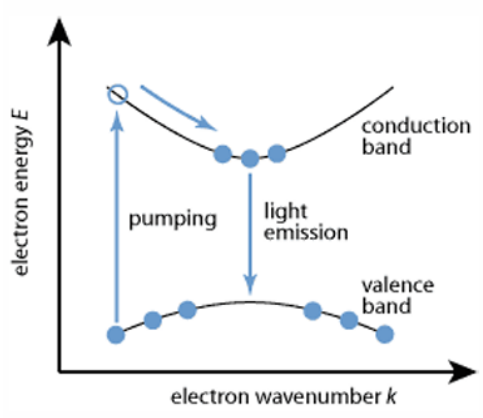

Figure 1.9: Jablonski Diagram of the 2 states involved in a laser diode

It is important to note that the diode emits light even when population inversion has not been achieved. This emission comes from spontaneous emissions, which produces light with a common broad spectrum, lacking coherence and directionality, similar to an LED source.

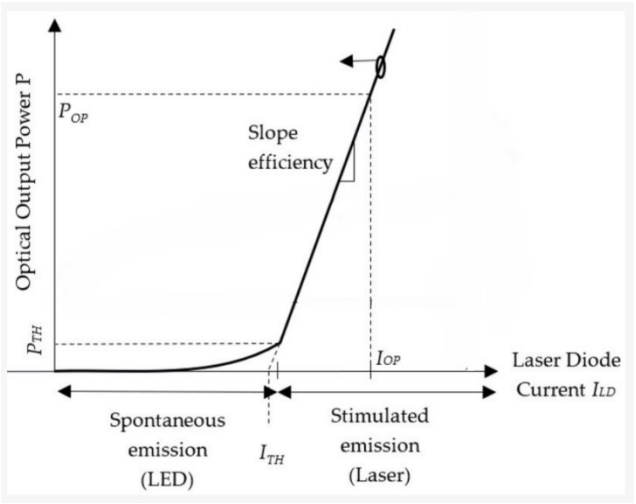

Figure 1.10: Graphical presentation of power output as a function of current of a laser diode. [Edited and reproduced from [2], under Open Access]

For the population inversion to be achieved, forward bias current need to increase until a certain value, that the threshold is met. Before that, the semiconductor acts as a light source, with LED properties. After current surpasses the threshold value, lasing occurs, as the stimulated emission mechanism dominate over the mechanism of spontaneous emission.

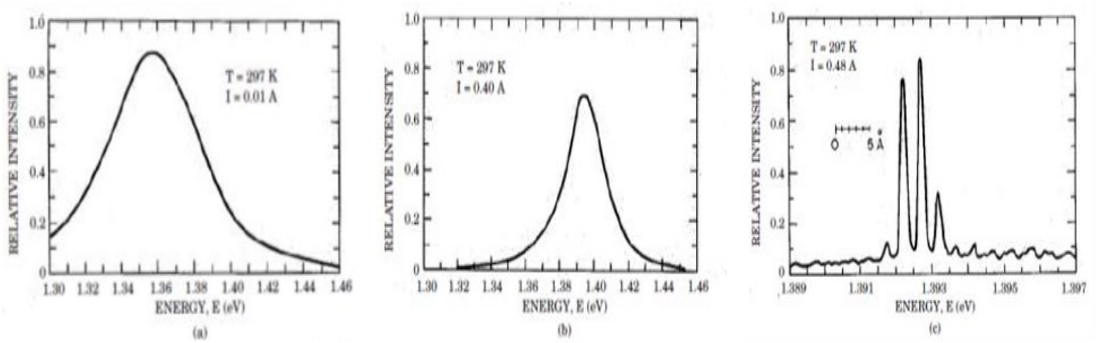

Figure 1.11: The graphs of the figure show the energy (spectral) range of a diode laser for different values of the bias current. In the first graph the spectral width is broad, as the device operates as an LED. In the middle graph, the current is near the threshold, and the spectral width narrows. In the last image, the current has exceeded the threshold, leading to further spectral narrowing and the appearance of peaks corresponding to the amplified modes.

1.4 Optical Cavity

In order to sustain laser emission, feedback must be introduced to maintain stimulated excitation, amplifying the lasing frequency. For clarification, we consider optical amplification when photons stimulate the emission of more photons of the same properties by de-exciting electrons from the metastable state. For this purpose, a cavity must be introduced in order for photons of the needed energy to continue stimulating electrons. The active medium of the laser is placed between two mirrors, this way emitted photons undergo multiple passes from one mirror to the other, and while following this route they continuously activate a chain reaction of electrons de-excitement, creating more identical photons.

The two opposing mirrors that face each other in the laser source, form a region of resonance around the gain medium, which is the active material of the laser. The total path length between the mirrors (from the first mirror until the light returns to it again) determines which wavelengths can be sustained within this region of resonance. During the operation of the laser, the standing waves that are formed within the cavity have wavelengths proportional to the path length. Let the distance between the two mirrors be equal to L, then the path length is equal to $2L$. More specifically, only wavelengths that are whole-number multiples of $2L$ can exhibit constructive interference and get amplified by the cavity. Any other wavelength gets canceled out by destructive interference.

Considering, the refractive index $n = C_0/C$, where C_0 is the speed of light in a vacuum and C, the speed of light in the given medium and given that $C = C_0/n = \lambda f$, the amplified wavelengths of the cavity are given by:

$$\lambda = 2L/k$$

where k is an integer.

Using wave speed equation $C_0/n = \lambda f$, the above relation becomes:

$$v = C_0 k/2Ln$$

For example, if we solve for two wavelengths with a $\Delta k = 1$, then the difference between their wavelengths would be $\Delta v = C_0/2Ln$.

From the above relationship between two allowed wavelengths, an important observation is made. As the length of the cavity decreases, the difference between the allowed wavelengths of the laser increases. The importance of cavity length selection for a laser is thus, highlighted. Both monochormacity and temporal coherence rely on this factor and they will be discussed further on.

It has also become clear that the amplification or gain increases with the total path length that photons travel within the active medium. The gain of the material itself is effectively lower. To clarify, the amplification is achieved, due to multiple passes through the gain medium inside the resonator (total path length), while the intrinsic gain of the material itself remains relatively low, in a single pass. A sufficient optical path length is required for significant amplification.

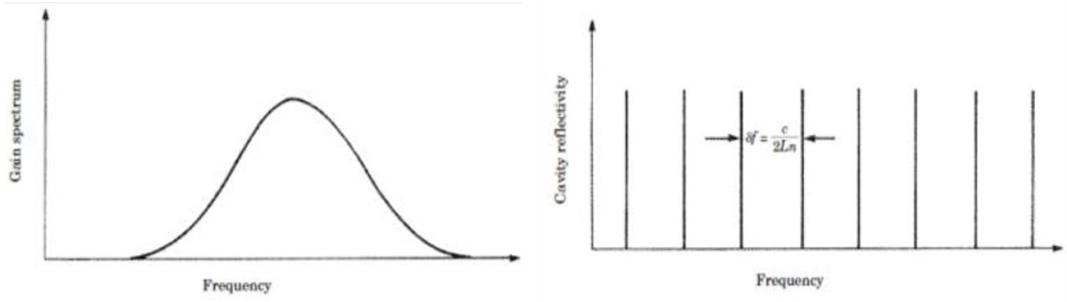

Figure 1.12: Gain spectrum curve of the laser (left) and diagram of the frequencies that can be amplified by the cavity (right)

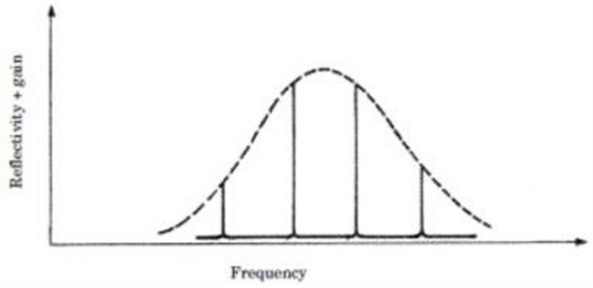

Figure 1.13: Final spectral profile of the laser as it exits the cavity

The allowed wavelength or in other words the number of the spectral lines a laser supports, do not only depend on the cavity structure. Another factor is the current, driving the laser. Current actively, controls the level of population inversion that takes place during operation. There are, of course, multimode lasers that emit a beam with multiple peaks around their central wavelength. But even a strictly single-mode laser can become multimode if, the bias current (and power) of a diode laser is lower than the typical operating level.

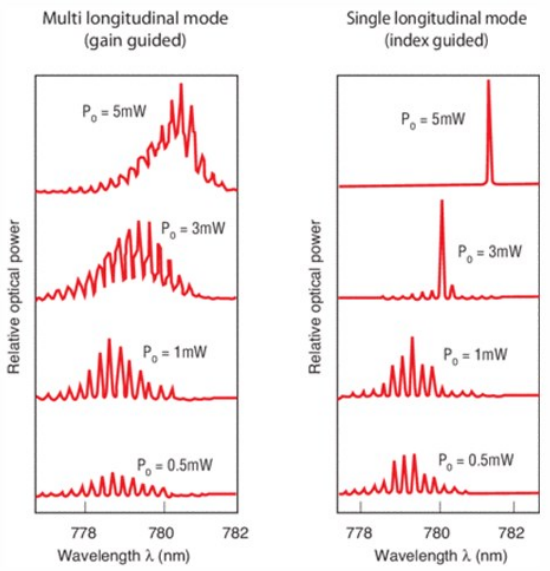

Figure 1.14: multi longitudinal (left) and single longitudinal (right) lasers at different bias current values

To achieve single longitudinal mode operation, various techniques can be employed. An approach, in the process of designing the cavity, would be replacing one of the mirrors with a Littrow reflecting grating. The Littrow grating acts as a filter reflecting the different frequencies of the modes at different angles. This way, the cavity can be precisely engineered to allow only the most amplified mode to propagate.

A closer look at the technical details of the mirrors reveal the need of a mean for photons to escape the cavity. A common approach is one mirror to be partially reflective at its center. This allows a group of the photons to exit while a significant amount undergoes multiple passes through the medium.

In addition, mirror systems may not be parallel, and there are many different setups, such as horizontal and at an angle. With these configurations, multiple propagation modes can be implemented, including multimode propagation, where different optical modes exist within the cavity. Therefore, L is not the same for all propagation directions, and thus the cavities enhance more than one distinct optical frequency, which leads to multimode operation. Another thing that should be mentioned here is that cavities can be designed to achieve a monomodal spectral profile, as well as incorporate wavelength selection mechanisms.

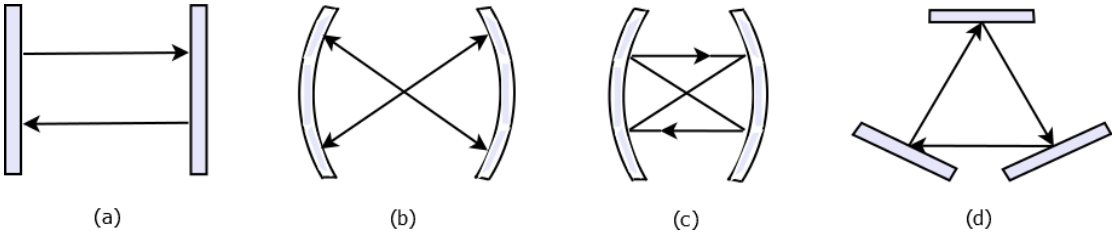

Figure 1.15: Graphical presentation of different optical resonator types. (a) Plane parallel resonator with cavity length $L = n\lambda/2$, n: integer value, λ: lasing wavelength (b) Concentric resonator with $L = 2R$, R: radius of the carvature (c) Confocal resonator with $L = 2f$, f: focal length (d) Ring resonator with $L = n\lambda/6$

1.5 Laser Properties

As a result of the technical specifications that were previously described, lasers are unique optical sources with special characteristics that distinguish them. First of all, laser beams are highly directional and focused, since oscillation and amplification occur only in the cavity with its properties. In addition, lasers are extremely monochromatic because of the narrow range of the difference between the levels that de-excitation occurs. As consequence, the same is true for the frequencies of the emitted photons. Another feature of a laser, is its coherent radiation, the vast majority of photons have the same phase. This occurs as only photons that are amplified contribute to the phase coherence. Last but not least, the resulted beam is typically very bright, with high intensity per unit solid angle; A result of the amplification photons, are subjected to.

1.5.1 Directionality

The output of a laser can potentially consist of nearly ideal plane wavefronts, meaning that the wavefronts (surfaces of constant phase) are perfectly flat and travel in a straight line. However, some divergence of the beam is unavoidable due to imperfect spatial coherence and even if we consider ideal spatial coherence, divergence is also caused by diffraction. The wavelength λ and the area D of the laser output aperture determine the divergence of the beam's vertex angle. Let's examine, first, the case of a beam with perfect spatial coherence. For an arbitrary amplitude distribution, from diffraction theory, the following relation is derived:

$$\theta_d = \beta\lambda/D$$

Where β is a numerical coefficient of the order of unity, depending on the aperture shape and intensity distribution.

In the case of partial spatial coherence, the divergence is significantly greater and its value is given by:

$$\theta = \beta\lambda/(S_c)^{1/2}$$

Where S_c is the coherence area.

1.5.2 Monochromaticity

The laser beam is mainly composed of stimulated emission photons. As was previously described photons trigger a chain of stimulated emissions while they are passing through the cavity and so spontaneous emission is unlikely. On top of that, photons emitted spontaneously, propagate in random directions, thus it is also unlikely that they will end up in resonance pathways. Still, there are "spontaneous" photons that will finally get amplified. This of course, affects temporal coherence of the laser but should not affect monochromaticity. Since laser de-excitation occurs between energy levels with a well-defined energy difference, the emission frequency (or wavelength) should be strictly monochromatic, with a frequency equal to the de-excitation frequency given by $v = h/(E_1 - E_0)$. However, this is not the case, because the lifetime of an energy level is large but not infinite, and due to Heisenberg's uncertainty principle, it is true that $\Delta E \Delta t > h/2\pi$. This means that the uncertainty in Energy ΔE is inversely related with the uncertainty in time Δt. In our condition, a state that has a broad lifetime, acquires energy with a narrow spread. Thus, perfect monochromaticity is impossible. There are additional effects on Monochromaticity. For example, in gas lasers, additional spectral broadening is happening, due to the Doppler effect, as the emitting molecules move at high velocities. In any case, from this broadened spectral profile only the allowed wavelengths by the cavity will be amplified. Despite these effects, the typical spectral range of laser remain really narrow, often on the order of sub-nanometers.

1.5.3 Temporal Coherence

The presence of a finite spectral bandwidth Δv means that the different frequencies in a laser beam can gradually get out of phase with each other. Temporal coherence is the time interval, over which the beam remains coherent (maintains its stable phase relationship). The time required for two oscillations with a frequency difference of Δv to get completely out of phase (by a full cycle) is $1/\Delta v$. Thus, coherence time is defined as $\Delta \tau = 1/\Delta v$. This definition applies to all type of light sources and is not unique to laser light. However, lasers exhibit uniquely high coherence values and are the only sources with such extraordinary long coherence times due to their extremely low spectral bandwidth Δv. For instance, a laser with $\Delta v \approx 1$ MHz, which is a large value for a laser, has a coherence time equal to 1 μs. This is significantly longer than typical atomic fluorescence lifetimes, which are of the order of nanoseconds. As a conclusion, lasers provide a beam with coherence time much longer than the typical timescales in atomic transitions. That's why it is considered spectrally pure and temporally stable, when interacting with atoms or molecules.

1.5.4 Spatial Coherence

The speed of light is so high that a light beam can travel a significant distance even with a short coherence time. Spatial coherence is the distance, over which the beam remains coherent. For example, when using a laser with a coherence time approximately $\Delta\tau \approx 1\ \mu s$, the distance its beam will travel in that time interval is $\Delta z \approx \left(3 \times 10^8 \frac{m}{s}\right) \times (1\ \mu s) = 300\ m.$ Coherence length is defined as $\Delta z = c\Delta\tau$ and represents the maximum separation over which portions of the beam remain phase-correlated. Only regions of the same beam that are separated by less than Δz can interfere constructively, within this range, the wave front maintains its phase relationship.

The book “Principles of Lasers” by O. Svelto [3], along with the lecture notes of “Optoelectronics” course by professor C. Balas [4], my supervisor, were a major influence for the previous section of this thesis. Both sources included a detailed introduction and analysis on laser physics. The book “Laser Physics” by P. W. Milonni and J. H. Eberly [5] offered a clear explanation of laser properties. Finally, another important scientific paper by H. Weber et. al. [6] further contributed to my work.

Chapter 2

Industrial Applications of Speckle Metrology

2.1 Introduction

Several unique phenomena arise due to the special properties of lasers. One of them is laser speckle, a direct result of illumination of a surface with monochromatic and coherent light.

Laser speckle is a phenomenon which occurs when laser light illuminates a diffuse surface. Speckle patterns are observed as, apparently, random variations of intensity on the surface, illuminated by the beam. As it seems, the illuminated region consists of tiny, irregularly shaped regions of light which are known as speckles. Speckles are caused by the interference of highly coherent light, produced by the laser as it is being scattered from different regions of the rough surface. Specifically, this is more apparent when the alterations of the roughness - the height variations - are comparable to the wavelength of the light.

Since different regions of the surface scatter light at different angles and it traverses different path lengths to reach the image plane, the intensity of the scattered field at any point is determined by the summation of the waves reaching there. Considering the monochromatic nature of the laser light, the superposition of these waves results in the amplitude of the field varying at different points. Destructive interference leads to dark speckles, while constructive interference produces an amplitude maximum, with various intermediate values observable between them.

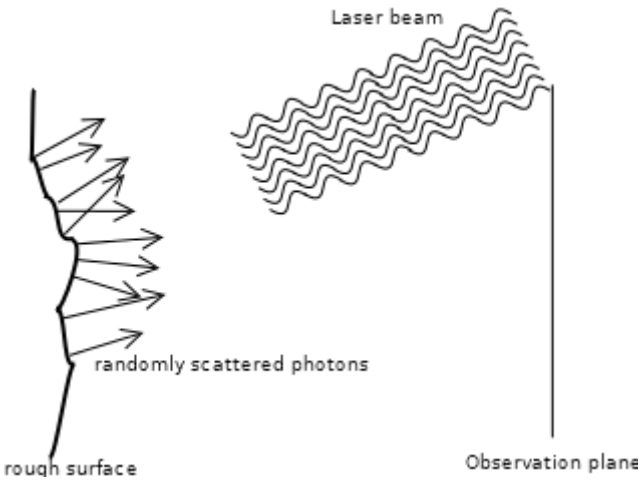

Figure 2.1: Reflection of coherent laser light from a rough surface

Speckle patterns are classified as either subjective or objective, depending on how and where the speckle is observed. When a speckle pattern forms in the image plane of an optical system, it is called an objective speckle. This term comes from the fact

that speckle's structure depends on the viewing system parameters, such as the lens aperture, position, and focus. Alternatively, if laser light which has been scattered off a rough surface falls on another surface without imaging optics, it forms an objective speckle. If a photographic plate or another optical sensor is introduced without imaging optics such as lenses, speckle characteristics depend only on the geometry of the system and the wavelength of the light. Objective speckle is typically observed in the far field (Fraunhofer region) but can also be observed near the scattering object, in the near field (Fresnel region). In conclusion, speckle structure relies on whether it is formed by free-space propagation or from an optical imaging system and is classified accordingly as objective or subjective.

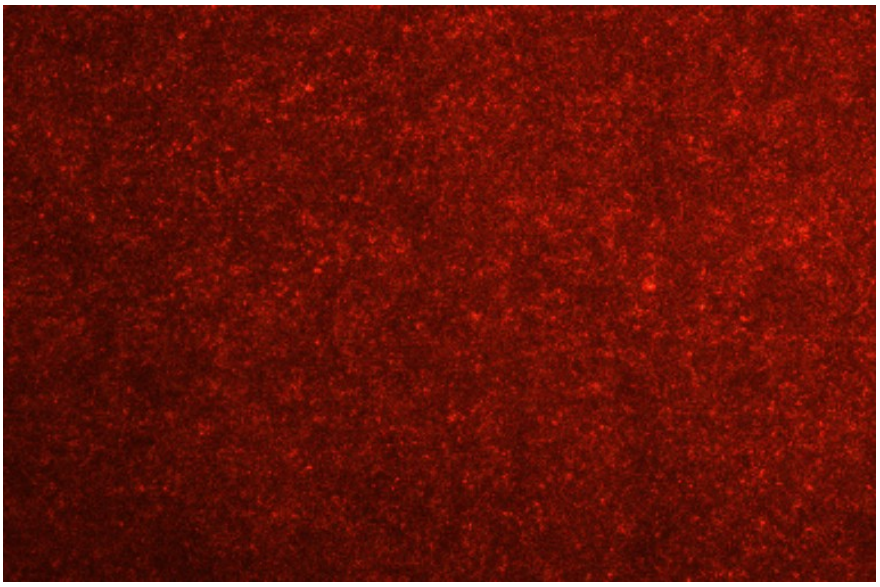

Figure 2.2: A magnified laser speckle pattern (captured at this Thesis laboratory work)

This subsection describing the speckle phenomenon is heavily influenced by the work of Fontelle [7] in their doctoral thesis and partly, by another doctoral thesis by Wei An [8]. The latter work, however, was a valuable resource for the following subsection too, which describes laser speckle metrology.

2.2 Laser Speckle metrology

Metrology application of lasers was one of the earliest that followed their development in 1960s. Holographic interferometry was the first method developed, a precursor to speckle methods and capable for a range of imaging measurement applications. This method led to the realization of speckle metrology in an, somehow, indirect way. This method's results were always accompanied by speckle patterns that limited its precision, and were initially considered noise.

However, around 1967, it was found that speckle patterns could be a carrier of unique information and not just an unwanted artifact. This realization led to the introduction of speckle metrology and eventually it was used to improve the performance of

holographic interferometry as a metrology tool. Over time, research concluded that the state of an object can be described through the speckle behavior, as this information is transferred through the modified mutual coherence function. This information is extracted by analyzing phase variations, speckle displacement or decorrelation effects, individually or in a combination of these factors.

Two major approaches arose in the way speckle fields are captured and analyzed, each based on a distinct optical configuration. The first relies on capturing images directly from the image plane, where the speckle is formed on the surface of the illuminated object and focused onto a camera or sensor using imaging optics. This configuration defines imaging-based speckle metrology and it involves subjective speckle, as the speckle structure depends on the lens and the imaging system in general. The second approach aims to observe the speckle pattern after light's diffraction from the sample, effectively capturing the result of their interaction, in a follow up step. This is the principle behind diffraction-based techniques, where speckle is typically observed in the Fourier or far field plane and computations usually involve the interference fringes that form in these configurations. In many diffraction-based setups, no imaging optics are required, and in such cases, objective speckle is observed. As a result, these two different branches of speckle metrology are closely associated with the division of speckle in objective and subjective types.

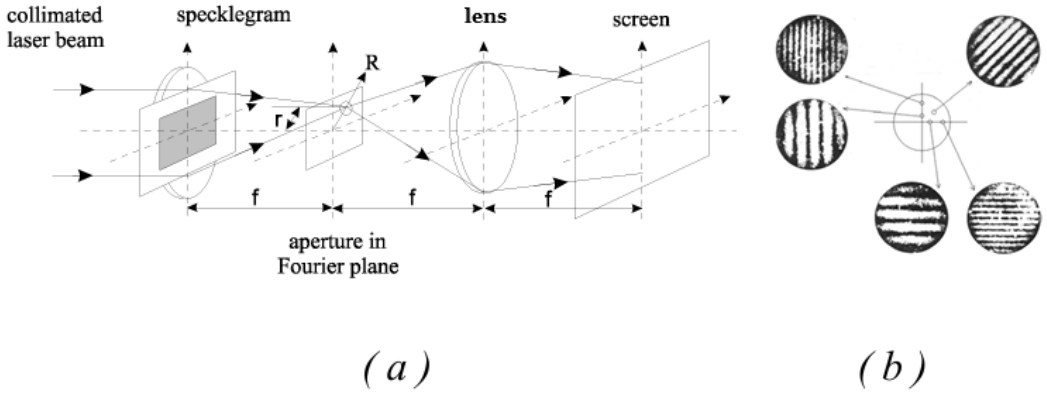

Figure 2.3: (a) Common arrangement of full-field Fourier filtering for obtaining the speckle pattern in diffraction-based techniques. (b) Fringes that are mainly observed in coherently superposed speckle fields (Interferometric methods with superposition of usually two speckle fields). [Reproduced from [8]]

Among the factors of speckle used as metrics, speckle decorrelation is shown to be linked to the precision of the optical measurement systems, both in diffraction based and imaging-based configurations. These correlation properties provide data about the phase stability of the scattered field, influencing measurement accuracy. In particular, tracking image correlation in space and time provide a way to perform interferometric measurements in disturbed environments. Analysis of the correlation properties in diffraction-based setups were the foundational principle of the earliest metrology techniques, marking the beginning of speckle-based optical diagnostics.

Speckle metrology can provide both point-by-point and whole-field data, with each approach offering advantages, depending on the application. Due to the advancements in computers and 2D optical sensors, both methods have been

significantly improved. However, pointwise algorithms are especially benefited from increased image processing capabilities, leading to faster and more precise measurements. They rely on acquisition of a temporal sequence of correlated speckle images, generating activity data as a 2D spatial contour map that represents a given statistical parameter. The most prominent pointwise algorithms are the intensity-based methods, where each map entry is constructed from a time sequence of intensity values recorded at the same pixel in the acquired speckle images. This type of image processing is extensively applied in speckle contrast analysis for measuring fluid flow and microscopic interferometry for evaluating surface roughness. Whole-field methods, on the other hand, provide spatially resolved information over an entire field of view, allowing for full-field displacement, deformation, and vibration analysis. These methods are implemented with different optical and computational techniques to process speckle patterns. The main example of optical filtering approach is an aperture filter being placed at the Fourier plane of the imaging lens. Other whole-field techniques rely on phase analysis and image tracking algorithms to extract displacement and strain information, like Electronic Speckle Pattern Interferometry (ESPI) and Digital Image Correlation (DIC). Whole-field approaches are useful in industrial inspection, biomedical imaging, and structural health monitoring, aiming at capturing global deformation patterns.

As previously described, speckle metrology utilize phase variations, speckle displacement, intensity variations or interference effects. Modern speckle metrology techniques are categorized into two major classes interferometric and statistical. Interferometric methods rely on the superposition of usually two speckle fields, where their relative phase differences are used to extract information about the physical parameter we are measuring (displacement, strain, vibration). These are diffraction-based methods that typically involve the interference of a speckle field with a reference beam (as in ESPI and DSPI) or with a spatially shifted copy of itself (as in Shearography). While most interferometry methods in use today, are based on coherently superposed speckle fields where phase relationships are maintained, non-coherent methods like speckle photography were developed and used in the past. Coherent speckle field superposition result in the formation of fringe patterns that are used in the calculations of the physical changes in the sample. Such techniques are highly sensitive, able to detect sub-wavelength deformations, and are widely used in non-destructive testing, material evaluation, and structural monitoring. Statistical techniques, on the other hand, do not depend on interference or phase analysis but rather use the temporal and spatial fluctuations of speckle intensity to extract information. These methods that are generally imaging based, quantify changes on the sample based on statistical metrics such as contrast, variance, or decorrelation rate. A prominent example is laser Speckle Contrast Imaging (LSCI), which is this thesis technique of interest, as well as laser Doppler Imaging and Diffusing Wave Spectroscopy. These approaches are favored in cases where simplicity, high-speed acquisition, and non-contact analysis are prioritized, even if they offer less spatial resolution than interferometric systems.

In the bigger picture, laser speckle metrology is a full field, non-contact technique and offers a variety of measurement use cases such as deformation, displacement, object shape, surface roughness, vibration, and dynamic events. It is highly effective on any rough surface with a sensitivity equivalent to the wavelength of the laser source, which makes it a powerful and precise tool. What further emphasizes its versatility is the wide variety of techniques it includes from phase-sensitive interferometric methods to

statistical, intensity-based approaches. This diversity allows speckle metrology to fulfil the needs of industrial applications for reliable measurement on different fields. These advantages have been amplified with the increasing processing power of latest computers, faster frame grabbers and sophisticated image processing software more practical and accessible than ever before.

2.3 3D object mapping

Laser speckle metrology has been proven an effective tool for 3D spatial measurements and structural analysis due to its ability to extract complex geometric and shape-related data in industrial contexts. This is especially true when conventional techniques are inefficient in cases that require independence from the object's distance, and the ability to measure depth even in narrow or deep structures. Phase sensitive techniques are the most prominent in this use case. As demonstrated by Sjödahl et al. [9],dual-wavelength interferometry and speckle deflectometry were shown to reconstruct shape with high precision, under dynamic or disturbed environments. A thesis by Wei An. [8] developed a modified variant (LiF) of electronic speckle pattern interferometry (ESPI) especially for 3D mapping of small parts. Depth slices were acquired by translating the sample stepwise and assembling speckle interferograms into a full 3D profile of the object surface. While this approach showed the potential of speckle metrology in 3D object visualization, it required several interferograms to acquire a single model of the sample, making it cost and time effective, impractical for industrial use. However, since 2002 that this method was developed, speckle 3D imaging techniques have evolved significantly, with some modern systems achieving real-time 3D modeling using just a single frame.

A notable example is the work by Wang et al. [10] that combined speckle projection profilometry (SPP) with a deep stereo matching network (DCSM) trained on both real and synthetic data from a Blender-based simulation. This implementation addresses the challenge of extracting accurate results from a single speckle frame, a constraint that limited the capabilities of previous approaches in dynamic 3D imaging. Their system achieved a 0.5-pixel disparity error rate, significantly lower compared to traditional and other deep learning-based implementations and showed strong generalization across varied geometries, including faces and industrial components. Similarly, Li et al. [11] presented a single frame 3D modeling method using a different approach. They proposed the projection of complex pattern, combining a speckle with a fringe pattern into a single image and the application of a Fourier-based phase retrieval method to reconstruct depth. Most importantly, their system operated at a frame rate equal to the camera's frame rate with high resolution results, making it well-suited for the most demanding real time applications.

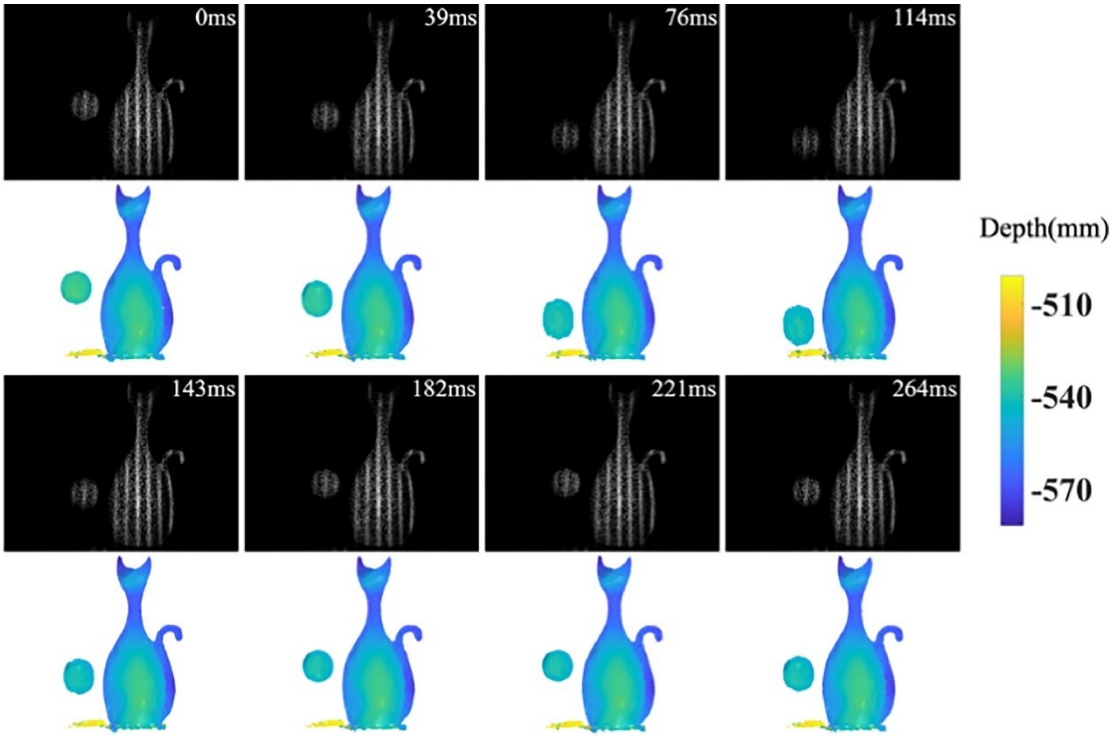

Figure 2.4: The reconstructed result of a ping pong ball's free fall and rebound next to a cat figure by Li et al. [Reproduced from [11]]

These recent developments with single-shot, high-speed, 3D reconstruction systems demonstrate the power of speckle metrology on this field. Speckle based metrology not only enhances traditional 3D modeling applications such as inspection and quality control but also paves the way for real-time process monitoring in modern manufacturing. Applications like laser cutting and welding rely on in situ monitoring that speckle metrology techniques could offer excellently.

2.4 Transient Process Monitoring

Laser speckle metrology has shown promising results in monitoring microscopic surface activity. Speckle techniques have been found useful in various scenarios related to different industries. A notable example of a use case that can be directly applied in industrial manufacturing is found in the thesis of Wei An. [8] In a targeted application they used LiF ESPI to evaluate solder joint deformation, a crucial quality parameter in electronics manufacturing. As the study explains capturing deformation patterns under thermal cycling or mechanical stress, can provide early insight into joint fatigue and reliability.

As a result, speckle metrology use, has been extended from general surface activity monitoring to a specialized transient process evaluation that will be thoroughly described as it is clearly intended for industrial use. In this context, statistical point-wise algorithms are more useful as they offer non-destructive and real time results and are capable of assessing local variations on different regions of a surface.

2.4.1 Paint and Coating drying

One popular industrial application is the evaluation of drying dynamics in coating and paint, where observing speckle fluctuations over time reveal information about the surface's state.

One of the earliest studies by Romero et. al [12] investigated this relationship between dynamic speckle and surface's state and applied it to assess paint drying. In a later study, Federico et al. [13] employed a statistical speckle metrology method and validated paint drying experiments with their dynamic speckle simulation model to demonstrate that the decorrelation of speckle patterns could reliably reflect the evolution of the drying process. Stoykova et al. [14] developed a statistical algorithm that mapped the speckle patterns into binary patterns and evaluated activity with a polar correlation function that resulted in much faster computation than conventional speckle approaches. They used their method to evaluate the drying of paint on a metal object with alternating height regions, acquiring reliable results indicating the varying activity across the object as intended. A recent notable advanced study that quantitatively applies speckle metrology in paint drying was conducted by Semerdzhiev et al. [15]. Through the application of laser Speckle Imaging in opaque coatings, the researchers identified the drying stages, and distinguished the open time which is the period that the coating remained workable, by setting contrast-based thresholds. Importantly, their results were validated with traditional techniques. The study's importance comes from the introduction of scaling relations to predict open time based on physical drying parameters and the achievement of capturing late formation phenomena such as polymer particle deformation and coalescence. Their approach confirmed that speckle metrology offers a quantitative real-time method, perfectly capable of industrial establishment in quality control of paint and coating processes.

2.4.2 Corrosion propagation

Corrosion, the gradual degradation of metals, is another transient process that laser speckle metrology has been widely applied. This phenomenon that arises from environmental interactions with the materials can be proven difficult to detect, especially in its early stages, using conventional techniques. A sensitive non-invasive monitoring method is crucial to prevent significant economic losses, as corrosion damage has a great economic relevance to the majority of manufactured products and engineering structures.

Since 1999, quantitative speckle metrology approaches have been developed. Fricke-Begemann et al. [16] used a speckle decorrelation technique on samples undergoing corrosion. They demonstrated that microstructural surface changes over time could be quantitatively linked to speckle decorrelation, providing a remote and non-contact method to monitor surface degradation even in early stages of the phenomenon. As they emphasized, this application is of major importance as typical corrosion depths are ~0.1mm, while speckle metrology is capable of studying effects on the nanometer scale. These results are supported by subsequent studies, such as Andres et al. [17]

that have applied Digital Speckle Photography (DSP), capturing speckle images before and after the onset of corrosion. In a recent study, Pedram et al. [18] artificially induced corrosion on a carbon steel sample to monitor its development in different stages. They demonstrated the application of a statistical speckle analysis technique to evaluate the pitting corrosion in metals. By applying constant voltage to a stainless-steel sample, to induce the corrosion, they observed that pitting growth rate progressively decreased over time, highlighting the method's sensitivity to the kinetics of corrosion propagation.

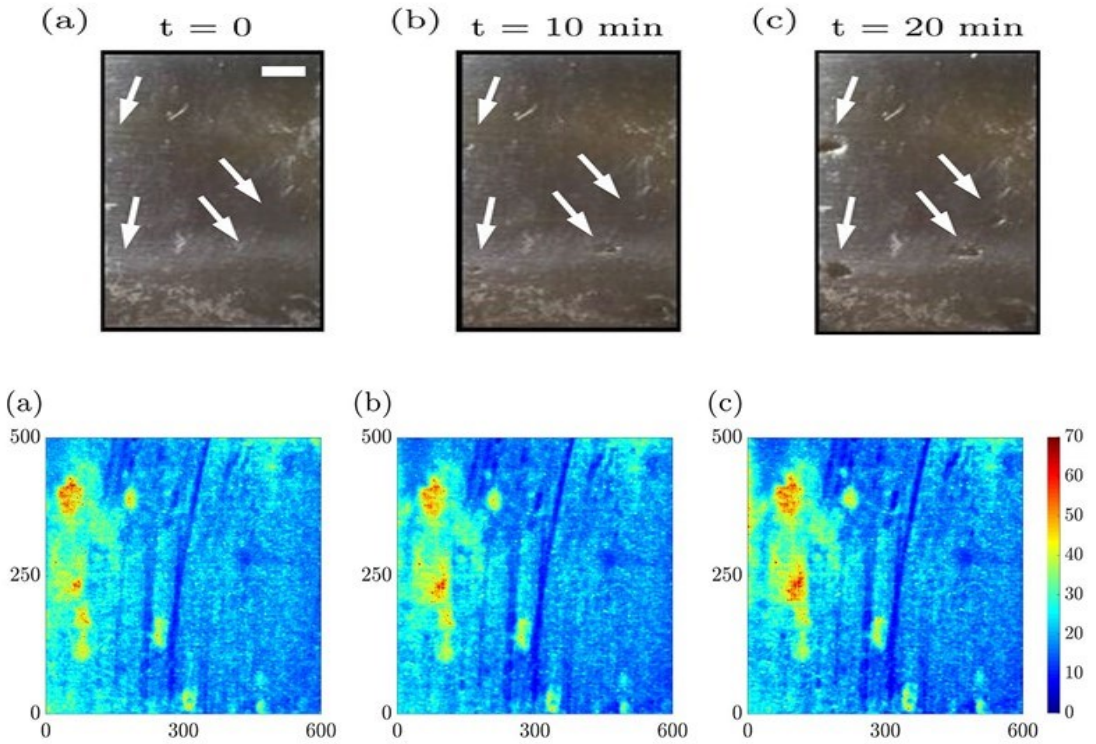

Figure 2.5: Results by Pedram et al. obtained by the motion history image (MHI) on a collection of images of a sample every ten minutes after the experiment starts in different corrosion stages. Two intermediate pits are imaged on the surface.
[Reproduced from [18], under Open Access]

These examples of corrosion monitoring demonstrate speckle metrology's compatibility with such application. The ability to quantitatively asses material degradation with a cost-effective tool is essential, considering the extend of corrosion's impact in industrial components. This is exactly what speckle metrology techniques have to offer with additional advantages such as early detection that conventional methods can fail to provide and non-contact real time monitoring.

2.4.3 Mechanical Fatigue

Beyond corrosion, mechanical fatigue is a transient process that has been extensively researched under the application of speckle metrology techniques. Fatigue is a progressive form of surface degradation that occurs in metals subjected to cyclic loading, very common condition in industrial components. Repetitive stress causes

microstructural changes, slip band formation and eventually cracks in the material. Because these changes are subtle and evolve temporally, they are difficult to detect using conventional methods.

Dai et al. [19] conducted one of the earliest researches on the way speckle patterns are influenced by mechanical fatigue. They captured and compared speckle patterns on the same material (aluminum alloy 6061-T6) in different stages of fatigue progression. They observed that even in early stages of the phenomenon, slip bands form on the material that lead to subtle but detectable changes in speckle appearance. Since there were strong indications that speckle metrology can provide significant data for the progression of mechanical fatigue, it became a popular field of research. Recently, Farahani et al. [20] were able to evaluate corrosion quantitatively, monitoring strain field development using ESPI. In this study, measurable displacement and strain variations were captured in different stages of fatigue's progression. The results offered early insight on the phenomenon before cracks were apparent on the samples. Another notable study by Kopec et al. [21] compared ESPI with Digital Image Correlation (DIC) in P91 steel samples under identical fatigue conditions. DIC was found to be more capable of identifying potential failure zones in the earliest stages of the phenomenon, thanks to its full-field strain tracking. ESPI on the other hand was able to provide complementary strain distribution data, supporting deeper quantitative analysis of the progression of fatigue. These examples show speckle metrology's true potential for in-situ fatigue monitoring in industrial application. The technique allows early detection of failure in critical components such as pressure vessels, turbine blades, and welded joints. The sensitivity of these approaches makes them a strong candidate for structural health monitoring.

These studies show the ability of laser speckle metrology to detect surface activity during transient processes, highlighting the effectiveness of speckle metrology beyond shape or displacement measurement. In most industrial contexts, metals are a primary concern, especially in fields like aerospace, automotive, construction, and energy where above studies are extremely relevant. These approaches are valuable for quality control in industrial painting and surface treatment processes, and can ensure early detection of defects or non-uniformities without interfering with the product.

2.5 Mechanical and Contact deformation

Another field that speckle metrology has been advancing is contact pressure assessing. Since surface deformations are known to alter speckle patterns, contact deformations have been investigated with speckle metrology since the early years of speckle-based methods. An early study by Osistev et al. [22] offered quantitative results using correlation-based speckle photography, revealing its true potential on this domain. The researchers measured the irreversible changes caused by the pressure of a flat slab on a steel cylinder, showing their interest industrial application. Their method involved capturing speckle patterns before and after the contact and they linked the fringes that developed, to the plastic deformation in the contact area. They developed a relationship between fringe contrast change and the degree of plastic strain and provided numerical values for contact pressures in kilonewtons.

Building upon the groundwork of early studies, pressure measuring has evolved significantly, leading from the development of ready to use speckle-based sensing tools, to multimodal soft surface sensors. Pei et al. [23] into 2022 presented ForceSight, a non-contact, real time force sensing tool utilizing laser speckle imaging (LSI). Surface deformations caused by applied forces are analyzed by speckle patterns in a precise manner. It's designed to accurately estimate force magnitude, quantitatively, not just detect the presence of force. The system considers practicality of use, requiring only a laser and a camera, with its software utilizing machine vision techniques. Its potential spans from industrial automation to human-computer interaction applications.

Another sophisticated study has combined optical scattering phenomena with machine learning to develop a high-resolution multimodal sensing tool. Shimadera et al. [24] developed a flexible soft material, with an embedded camera and a laser directed on the material, that is able to detect contact force, location and temperature through speckle analysis. Their vision was to deliver a solution without the traditional arrays of electrical sensors to acquire sophisticated measurements. The patterns are decoded using deep learning that enabled real time simultaneous sensing with high spatial resolution. This method offers the capability to recognize object shaped that touch the surface, responding to environmental changes. This ground-breaking achievement paves the way for applications in wearable electronics, robotics or even prosthetics, involving several industrial fields.

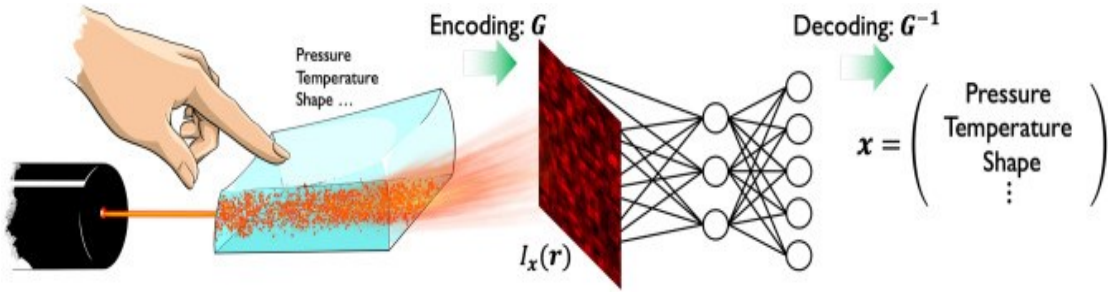

Figure 2.6: Conceptual schematic of the proposed multimodal soft sensing approach by Shimadera et al. [Reproduced from [24], under Open Access]

These developments demonstrate the link of this technique with contact pressure monitoring in the industry. From foundational photographic methods to complex real-time systems that involve cutting edge technology, the evolution of speckle-based approaches has clearly established their value. As industries increasingly seek precise, flexible, and non-invasive solutions for monitoring mechanical interaction, speckle-based systems have all the requirements to prevail.

2.6 Biological Specimens Monitoring

Biospeckle is a term that has been established to describe speckle patterns produced by coherent light interacting with biological specimens. These patterns carry information about internal activity as cellular motion, metabolic processes, structural changes and have been exploited in agri-food, bioproduction, pharmaceutical and other bio-industrial fields. This section explores key examples of applications to biological specimens, emphasizing the versatility of speckle analysis methods, especially statistical.

In 1985 oulamara et al. [25] conducted a pioneering research, the first published study of laser speckle metrology applied on botanical samples that laid the groundwork for modern biospeckle techniques and even LSCI. The connection with LSCI is apparent due to their method being a statistical approach, analyzing intensity fluctuations of speckle patterns pixel by pixel and relating intensity autocorrelation function to biological activity. They interpreted the decorrelation of speckle pattern as a result of internal activity in fruits and seaweed, specifically the slow movement (sometimes cyclical) of the chloroplasts and amyloplasts. Furthermore, their method was semi-quantitative as they generated intensity correlation curves and extracted decorrelation time that was compared across samples. This study led to a number of studies focused on the industrial exploitation of speckle metrology.

Several studies have applied statistical speckle metrology to evaluate the quality and condition of fruits and vegetables. In particular, Xu et al. [26], Pajuelo et al. [27], and Rabelo et al. [28] used speckle activity analysis to assess pre and post-harvest condition, bruising, and physiological changes. These studies used statistical methods such as autocorrelation, cumulants, and temporal descriptors to extract indicators of biological activity. Their results showed that biospeckle imaging can monitor fruit quality and usefulness in agro-industrial contexts. A particularly targeted study by Zdunek et al. [29] investigated the effect of temperature on apple biospeckle activity, aiming to evaluate the internal quality changes during storage. Comparing three different statistical approaches they concluded to the most robust indicator of biospeckle activity with high sensitivity in detecting freshness loss. This enhances the applicability of speckle metrology in food quality monitoring and storage optimization in the agri-food industry.

Laser speckle metrology has also been explored for monitoring biological growth processes. Romero et al. [30] aimed to assist in microalgae large-scale cultivation which is critical in several industries like pharmaceutical, cosmetic, biofuels and others. This study demonstrated that the growth of the microorganisms can be detected using statistical analysis of speckle patterns produced by the samples. Their use of Time History of the Speckle Pattern (THSP) and autocorrelation-based cumulants, a statistical approach showed high correlation with the standard technique, optical density (OD) measurements, which is a common method for estimating the concentration of cells in microbiology. By measuring speckle activity directly from the culture containers without extracting samples, their approach promises real-time, in situ monitoring of algal biomass in lab-scale photobioreactors. This opens new perspectives for applying speckle metrology in bioproduction process control and optimization across several industrial domains.

Chapter 3

Biomedical Applications of speckle metrology

The numerous advantages of speckle analysis, which have shown such relevance in the industry, suggest strong potential in the biomedical field as well. Non-contact, real-time monitoring techniques are valued both in research and clinical diagnostics, which justifies the research of speckle metrology into multiple processes that involve structural, mechanical or cellular changes. Unlike traditional biomedical imaging techniques that require contrast agents, substances introduced into the body, speckle-based methods simply rely on optical properties. Both interferometric and statistical approaches have been applied in the biomedical field, with the latter prevailing as they are simpler and faster, compatible with real time imaging. Furthermore, the nanometer scale sensitivity to motion is another benefit of speckle metrology that makes it ideal in blood perfusion measuring, our application of interest. As this will be our main subject of analysis in the specific part, this section of biomedical applications will focus on other applications that exploit the sensitivity of speckle patterns. In fact, speckle analysis has a broad biomedical potential, this section aims to review.

At this section of our thesis, the review by Heeman et al. [31] has been a great guide with a collection of important studies, specifically on the clinical applications of laser speckle contrast imaging (LSCI), an imaging based statistical approach, which is the technique of interest in this thesis.

3.1 Microorganism and Cellular Growth Monitoring

Recent advancements have expanded the utility of laser speckle imaging. Techniques initially developed for industrial monitoring have shown potential in the biomedical field. Such example is the tracking of microbial growth that was previously described in the context of its industrial use. The methodology used for microalgae activity measuring, is essentially applicable to biomedical applications too, creating a bridge between the industrial and clinical applications of speckle metrology. A lot of studies have applied statistical speckle analysis to investigate microorganism growth and cellular behavior. By measuring the fluctuations of speckle patterns over time, these techniques can assess biological function, being effective in microbiological diagnostics, clinical research, and biomedical experimental studies.

Two of the earliest studies by Pomarico et al. [32] and Murialdo et al. [33] are fundamental for speckle metrology's later progress in microbial growth and biological activity. Pomarico et al. used speckle interferometry to assess the motility of nematode parasites after their exposure to different anthelmintic drugs. They were able to extract activity curves from their speckle analysis that showed different pharmacodynamic profiles, with Levamisole being the most effective drug. This is an indication that the method may be able to provide quantitative results. Similarly, the study by Murialdo et al. highlighted biospeckle sensitivity to the metabolic activity of microorganisms in

different growth conditions. Building upon this ground work, recent studies have evolved significantly. In a notable study from Balmages et al. [34], a laser speckle imaging system enhanced with sub-pixel correlation analysis was developed. Their technique was not only able to detect the expansion of the colony of interest but also visualized activity “rings” within the colonies, demonstrating that growth is driven by peripheral cells. This finding was supported by flatbed scanner images and was further verified by theoretical models. A related study, leaded by the same researchers [35] employed neural networks in order to automate the classification of bacterial colonies as growing or non-growing. They used the same sub-pixel correlation approach with their previous study in combination with a statistical speckle technique that were both fed into the multilayer perceptron (MLP) neural network. This approach showed strong potential for assessing the physiological state of bacteria, including the impact of antimicrobial agents, with capabilities for real-time microbiological diagnostics.

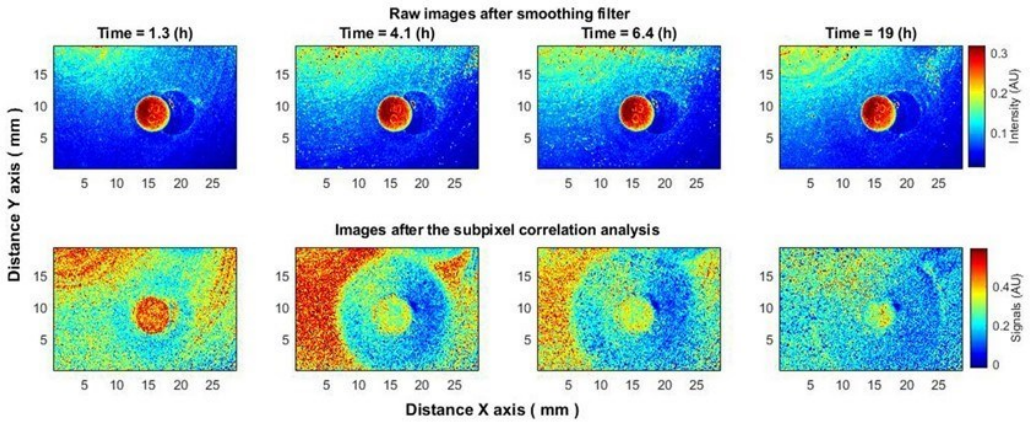

Figure 3.1: An experiment conducted by Balmages et al. where the antibiotic disk was placed on the surface with bacteria already growing. The bottom raw shows the results of their sub-pixel correlation technique. [Reproduced from [34], under Open Access]

As a conclusion from the studies reviewed, the relevance of speckle-based imaging in the microorganism growth is increasing. The introduction of modern methods like neural networks increases the effectiveness of speckle analysis, while the classic advantages of label-free and real-time processing further support its potential. Those features collectively pave the way for these techniques to be established in the biomedical field. Speckle metrology is proving itself as a powerful diagnostic tool for microbiology pharmacology and clinical diagnostics.

3.2 Drug Testing and Pharmacodynamics

Following the success of speckle metrology in microorganism growth monitoring, it is natural to proceed with this section on their use in evaluating pharmacological agents. As a matter of fact, some studies of the previous section tested the effect of drugs in microorganism populations. Both clinical and experimental environments benefit in

understanding how drugs influence biological systems. For this reason, the advantages speckle metrology could offer in such field is worth noting.

A distinctive study was published by Silvennoinen et al. [36] in the early 2000s that further researched the potential of statistical speckle metrology. They employed (THSP) and Inertia Moment (IM) analysis to monitor the local deformation on the surface of pharmaceutical tablets. Their goal was to track the elastic relaxation of tablets, the time-dependent compression before they resolve. This is essential in quality control of medicine and can help optimize tablet formulations, consistency and quality. After confirming that indeed mechanical relaxation can be tracked with their method, they analyzed different types of tablets. Each tablet's analysis resulted in a distinct speckle activity profile, proving the effectiveness of speckle techniques. Their findings are supported by Pomarico et al. [32] whose study were reviewed in the previous section. They computed different pharmacodynamic profiles in several anthelmintic drugs. Another study that has already been included by Balmages et al. [35] evaluated the use of antibiotic effect on bacteria with their neural network enhanced speckle-based system. More recently, a study came to address a drug administration issue, revealing how different infusion routes of substances influence their effects. In essence, Postnov et al. [37] applied laser speckle flowmetry to monitor blood perfusion in rat kidneys, as it is affected under the influence of drug infusion. Their analysis showed that angiotensin II after infused created localized oscillatory patterns in blood flow due to uneven vascular delivery, something that could not be detected by traditional methods. The contribution of this study is that it was able to confirm the capability of speckle metrology to reveal dynamic heterogeneities of drug effects within organs.

These studies together demonstrate the effectiveness of speckle techniques in drug monitoring and their practical advantages. They offered valuable data, both by observing microbial responses to prescriptions and by tracking changes in tissue under medication. Together, these use cases show the potential of speckle metrology to establish a strong presence in pharmacodynamics research, clinical diagnostics.

3.3 Tissue viability and damage evaluation

Beyond microorganism growth and pharmacodynamics, let us now dive into human related biomedical studies. Ever since its early years, laser speckle metrology is known to be effective in monitoring microscopic surface activity. Apparently, damaged or non-viable tissue effect speckle patterns in a distinguishable way and provide significant diagnostic information. Combined with the simplicity of the required set ups, any related application is constantly under the scope of researchers. "Tissue viability and damage evolution" is a wider spectrum of applications that covers different health-related conditions. In this context, statistical algorithms prevail in the moment and have major advantages that have already been discussed in previous sections.

3.3.1 Burn depth - assessment

Accurate assessment of burn depth is important for selecting the appropriate treatment strategies and achieving the best healing outcomes. The clinical field needs cost-effective techniques, accessible in any healthcare setting, non-invasive and able to provide rapid results that can be applied to patients experiencing pain. Optical methods have been explored for decades in this context, making burn evaluation one of the most clinically investigated use of speckle metrology, as well. Laser Doppler Imaging and LSCI are the most common approaches, with LSCI being the recent focus of research due to its simplicity and convenience in use. They are both optical techniques involving similar configurations with a laser source and a CCD camera and both involve statistical signal analysis. However, LDI is not technically a speckle-based method as it relies on Doppler frequency shift detection. Nevertheless, it is still included in the following clinical comparisons due to its similarity with LSCI in methodology and application.

As Pape et al. [38] point out only about 70% of burns are correctly assessed and treated by the medical professionals, and burn depth is also critical for their treatment. This study was likely the earliest study to demonstrate the value of LDI in burn depth assessment, outperforming traditional visional inspection in intermediate-depth or second-degree burns. Since this study took place in 2001, research mainly focused on LDI technique. Stewart et al. [39] conducted a comparison among LDI and LSCI in burn scar perfusion and found LSCI to be a favorable alternative because of its ease of use and faster acquisition times. Crouzet et al. [40] further confirmed the relevance of LSCI in wound assessment in a preclinical mouse model. They demonstrated that the technique was capable of distinguishing superficial and deep-partial thickness burns. Building on this, Lindahl et al. [41] applied LSCI to pediatric scald injuries and showed that early perfusion measurements correlated with wound healing outcomes at 14 days after the injury. This study's contribution was significant as they confirmed that early wound outcome prediction is possible using laser speckle imaging, inspiring more research on the application. A later study on this direction by Mirdell et al. [42], further validated LSCI accuracy in pediatric scald wounds, providing greater clinical robustness. They confirmed the ability to predict healing outcomes and surgical needs in this clinical study, reporting that a perfusion measurement no more than 24 hours after the burn could exclude the need for surgery with high negative predictive value (NPV). The most recent study revisited the comparison between LSCI and LDI across different healing categories. The clinical evaluation by Zheng et al. [43] of 50 burn wounds in patients of different ages and burn etiologies, achieved high accuracy in healing time predictions. Their results showed a high sensitivity of 71% and specificity of 95% in identifying wounds that healed in a total of 14 days and similarly strong performance for those requiring more than 21 days versus more delayed healing occurrences. The method found LSCI to be more practical in clinical settings, with shorter imaging time and increased comfort in patients, especially children.

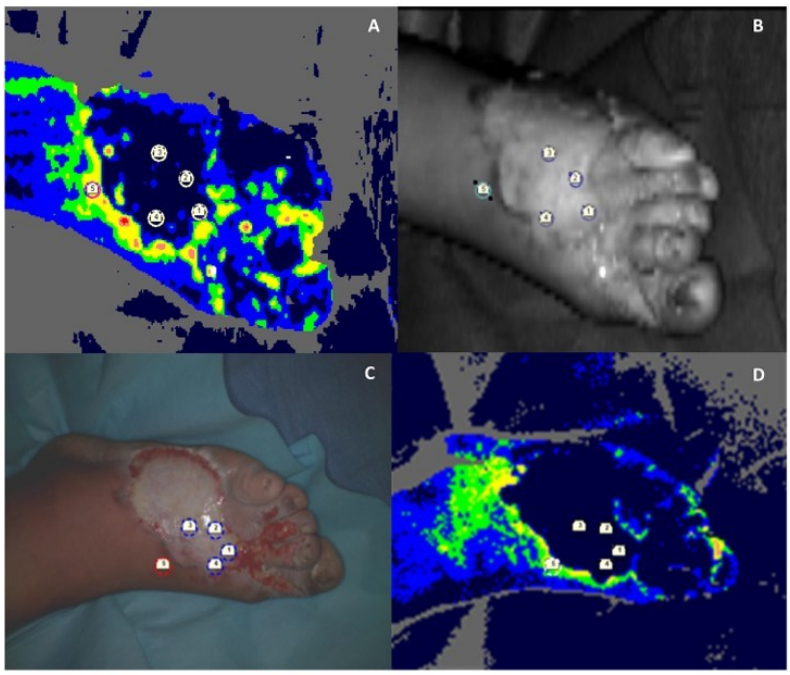

Figure 3.2: Results of selected ROI in a burn wound by Zheng et al. comparing LDI with LSCI. A. LDI flux image; B. LDI video image; C. LSCI video image; D. LSCI flux image. [Reproduced from [43]]

Wound assessment is a clinical biomedical application that speckle metrology has been adopted in the last two decades. Not only LDI is currently a standard technique established in the field, but LSCI has become an alternative method with more advantages and a great potential to take the lead in the following years. The contributions of the reviewed studies show that LSCI has clinical value in improving burn assessment accuracy and patient outcomes, especially in challenging partial-thickness cases. This growing trend of speckle metrology technique is no surprise as its non-invasive, fast and accessible nature is really suitable for the demands of wound assessment.

3.3.2 Ulcer evaluation

Ulcers are localized injuries, open sores that occur on the skin or the soft tissue inside the body such as in the mouth or stomach. They can result from prolonged pressure or other conditions like diabetes and vascular insufficiency. Pressure injuries and ulcers monitoring is another application that falls under the broader category of tissue viability and damage evaluation. These are high impact clinical scenarios, similar to burns, where speckle metrology can provide critical diagnostics. This is no surprise, as ulcers are essentially another type of wounds, sharing some of the same principles in diagnosis and treatment.

Speckle metrology has been applied to various types of ulcers, including diabetic foot venous and digital ulcers showing promising results. Specifically, LSCI has taken a leading role in this field, showing similar potential to that seen in burn wound assessment. Ruaro et al. [44] in a clinical study, evaluated digital ulcers caused by the systematic sclerosis, before and after their treatment. They report significant perfusion

increases in the ulcer region in combination with reductions in ulcer size and pain score, confirming the clinical utility of LSCI. Van Vuuren et al. [45] on the other hand, demonstrated that LSCI could excel in assessing ulcers caused by Venous disease. This important methodological study described that predictions of venous ulcer healing outcomes are possible based on perfusion patterns, especially at the wound edges. They analyzed 25 venous ulcers and used a two-week follow-up to distinguish between healing and non-healing ulcers. They provided metrics that show a sensitivity of 92.3% and specificity of 66.7% in predicting wound healing. This confirmed the prognostic value of LSCI in clinical ulcer management and supports its treatment planning. In diabetic foot ulcers, Mennes et al. [46] reported similarly promising results, with LSCI distinguishing between different ischemia severities. Their work validated the reproducibility and efficiency of speckle imaging. This study suggested that speckle analysis could be a valuable complement to current diagnostic tools. In a follow up study, though, Mennes et al [47] succeeded further advancements. They introduced a semi-automatic method, critical for clinical applicability of LSCI in diabetic foot ulcers. While manual operation of a ROI analysis would need 15 minutes, preventing the technique from being clinically adopted. Their system would need approximately 90 seconds to operate, while maintaining excellent agreement with manual assessment. The method was tested on 66 LSCI recordings from 33 patients, including different perfusion tests (baseline, PORH, and Buerger's). It was proved consistent in tracking microcirculation around ulcers, their edges and surrounding tissue. This notable study sets a foundation for faster and more objective wound analysis.

There is an apparent growing significance of speckle metrology in ulcer evaluation, with LSCI proving to be a reliable technique. Laser metrology have shown clinical potential across different ulcer types, from assessing perfusion in digital ulcers caused by systemic conditions, to predicting healing in venous ulcers and diabetic foot cases. The ability to provide label-free, real-time imaging, lately combined with semi-automatic analysis is promising for wound monitoring and decision making in the clinical field. Still, more development and validation will be essential for broader adoption of the techniques.

3.3.3 Wound healing

The same advantages that brought speckle techniques to such relevance in burn depth and ulcer assessment apply naturally to broader wound healing applications. While burns and ulcers are two well-studied specific cases, speckle metrology shows growing potential in being used in the broader category of wound healing. This is no surprise, as many of the principles remain the same and nearly all types of wounds benefit from early prognosis and monitoring. A recent example is the work by Hsieh et al. [48] who proposed a speckle-based system enhanced with automatic region of interest selection and tracking during wound monitoring. Their study addresses an apparent limitation of LSCI in clinical practice, the stability requirement of the technique. The difficulty of keeping the target region stable when imaging patients is the main drawback of speckle metrology limiting its use in all kind of applications. They developed a system with object tracking algorithms to correct ROI positioning, resulting in high agreement with manual tracking methods (ICC = 0.798–0.917 for acute wounds). The technique was reliable across both acute and chronic wound types with

high potential to improve accuracy, reduce workload. The study's direction signifies the value of speckle metrology extended beyond specific wound types.

This transition to general wound healing monitoring extends beyond thermal injuries and ulcers evaluation with especially LSCI being investigated for a wide range of wound types, including chronic ulcers, surgical sites, and traumatic injuries. The core benefit remains the detection of perfusion-related changes that are indicative of healing progress. Studies like that of Hsieh et al. reflect a shift toward clinical integration, where automated tracking and objective metrics are used to support speckle metrology's role in the biomedical field.

3.4 Functional Tissue Imaging

Moving forward to the last section of the biomedical applications, we introduce a broader category that includes different dynamic tissue and physiological factors. This functional tissue imaging section is necessary to cover all the diverse ways which speckle metrology can be applied in the biomedical field, beyond structural damage or pathology. It is widely known that speckle techniques are highly sensitive to motion down to nanometer scale, ideal for capturing any small-scale deformations and subtle biological activity. In the following section, we include some notable studies, harnessing these capabilities of speckle metrology.

3.4.1 Cilia motility monitoring

A representative application is the imaging of cilia motility. Cilia are the tiny, hair like structures that can be found on the surface of epithelia cells, particularly in the respiratory track which are the aim of a unique study se review. Assessing cilia's function is important in the diagnosis of airway diseases as they are vital for the clearance of mucus. Long et al. [49] developed a light-sheet laser speckle imaging technique to achieve monitoring such extraordinary tissue. In their setup, a laser beam is shaped into a thin sheet and projected onto the sample at a shallow angle. The resulting scattered light is recorded as a speckle pattern by a high-speed camera placed orthogonally to the illumination plane. Their system was used for characterizing cilia beating patterns in human nasal epithelial tissue. They achieved to estimate ciliary beat frequency and subtle features of the beating wave front. In addition, they showcased that asymmetries between power and recovery strokes can be detected as well as directionality changes across the beating cycle. This was an extraordinary study offering valuable results with a high potential to be clinically adopted following further research.

3.4.2 Cell motility and protein dynamics

Another clinical field where speckle metrology can be applied to is cell motility. Speckle-based tracking has been researched in cell motility since early on, with a study

arising in 1998 combining dynamic speckle analysis with fluorescence microscopy. In this pioneering work, Waterman-Storer et al. [50] introduced Fluorescent Speckle Microscopy (FSM), a technique where small quantities of fluorescently labeled proteins are introduced in the cytoskeleton, resulting in a “speckled” appearance. The speckle pattern which results from the random distribution of labeled proteins, can be tracked over time, enabling the visualization of the internal motion of key structural components in living cells, such as actin filaments and microtubules. This technique revealed important features of how cells move and divide, into microtubule flux, mitotic spindle movement, and retrograde actin flow in migrating cells. Since the inception of this technique, several researchers have studied its applicability on the subject.

Dormann and Weijer [51], for example, explored the potential of FSM in live-cell imaging. They highlighted FSM as a valuable method for tracking cytoskeletal activity during cell movement, confirming the technique’s value in visualizing filament dynamics. Notably, they placed FSM alongside other powerful approaches such as TIRF and FRAP for analyzing molecular movement in migrating cells.

Through this ongoing research, FSM has been further developed with a recent study delivering important advancements. Yamashiro et al. [52] developed Single-Molecule Speckle (SiMS) Microscopy an extension to FSM method. This approach is capable of tracking the behavior of individual protein molecules, like actin, within live cells, offering a more detailed look at internal cell dynamics. The study provided critical insight into how cells reorganize their internal structure during movement and suggested they may follow different mechanisms than what was previously assumed. In addition to their medical contribution, they later developed an electroporation-based version (eSiMS), with an improved spatial and temporal resolution, allowing nanometer-scale displacement analysis with very low localization error equal to ~ 8 -8.5 nm at 100 ms exposure time. This creates the potential for more applications in actin dynamics and drug response studies. Furthermore, their improved method does not require genetically tagged protein, instead it uses electroporation to introduce chemically labeled actin into the cells further improving its accessibility and reproducibility.

In conclusion, the use of speckle metrology combined with fluorescence imaging became a powerful tool for studying cell motility. It has evolved to advanced single-molecule tracking techniques tracking individual protein molecules in live cells with a nanometer precision and without requiring extensive genetic manipulation or complex optics. This method has progressed to the point of revealing particular cell mechanism, that have not been observed before [52]. This positions it as a practical and high-resolution tool for studying cytoskeletal dynamics in real-time, with high potential to take a lead on the field of cell and protein dynamics monitoring, as well as other biomedical regions like drug response monitoring.

Chapter 4

The importance of measuring blood perfusion

Blood perfusion, the central focus of this thesis, is a fundamental physiological process that accounts for the function of every organ in the body. It is strongly linked with tissue oxygenation, which is necessary for sustaining life itself. For this reason, blood perfusion importance is obvious and its dysfunction is associated with several health issues. Among them tissue hypoxia, energy depletion, and eventually cellular damage are severe complications that underscore the significance of its monitoring in clinical environments. It is worth noting, that blood perfusion measurement is indeed a common application of laser speckle metrology, as non-invasive optical imaging is highly beneficial in medical diagnostics.

4.1 Definition and Biological role of blood perfusion

Blood perfusion refers to the passage of blood through the vascular network of biological tissue. It is typically measured in milliliters per minute per gram of tissue (ml/min/g) which provides a quantitative index of vascular supply. Perfusion is a vital physiological process that supports cellular metabolism, tissue viability and overall homeostasis across all organ systems. This function is made possible as blood flows through the body ensuring the continuous delivery of oxygen, nutrients, hormones, cells, platelets and other elements essential for tissue function. At the same time, it takes care of the metabolic waste products removal from the body. Blood flow itself is maintained by the cardiovascular system, which consists of the heart, blood vessels and two main circulatory loops: pulmonary and systemic circulation. The pulmonary circulation oxygenates the blood in the lungs and systematic circulation delivers the oxygenated blood to the rest of the body. The heart pumps blood to the organs through different types of vessels that each serve a unique purpose.

A central function of perfusion is to maintain sufficient tissue oxygenation, which is essential for cellular energy production. This article by K. Powers and A. Dhamoon [53] analyzes the process of oxygenation in depth. According to them, oxygenation is the process by which oxygen is absorbed from the lungs into the bloodstream and transported, bound to hemoglobin, through the circulatory system. However, the delivery of oxygen requires sufficient perfusion. Even a fully oxygenated blood supply may fail to meet local tissue demands if perfusion’s function is disrupted. Systemically, perfusion determines how much oxygen finally reaches the tissues. This part takes place in capillary vessels which enable nutrient and gas exchange. It is established that even with good lung function and high arterial oxygen content, regional hypoxia can happen as a result of insufficient tissue perfusion, especially in metabolically active or peripheral tissues. This shows the importance of assessing local perfusion when investigating oxygenation related health issues.

Even more importantly perfusion enables the transport of various essential substances beyond oxygen, through the capillary network. Among these, it is responsible for glucose, and growth factors exchange. Oxygenation in combination with the latter substances is essential for wound healing and tissue regeneration. Without proper vascular supply, wounds may heal more slowly or become infected. This is particularly relevant in chronic wounds, such as diabetic ulcers, where microvascular dysfunction impairs the healing process.

Perfusion is also critical in endocrine signaling and immune function. Blood is the main carrier of hormones which enable communication between different organs. In a similar way, immune cells rely on the vascular system to reach infected or injured regions. Inflammatory mediators, antibodies, and cytokines are all distributed through the bloodstream, and impaired perfusion can compromise both immune responsiveness and healing capacity.

Furthermore, perfusion's role extends to another physiological process critical for body function, thermoregulation. Thermoregulation is extensively covered in the review of Charkoudian Nisha [54]. As they note, microvascular adaptations that result in necessary alterations of blood perfusion come to help the body's function under heat stress or cold environments. During heat stress, blood vessels near the surface of the skin dilate to promote heat dissipation, while in cold environments they constrict to preserve core temperature. These two mechanisms that are familiar to most people, and easily observed in our bodies are called vasodilation and vasoconstriction. They are vascular adjustments, regulated by the autonomic nervous system and vital for thermal homeostasis under changing environmental conditions.

Similar phenomena take place during physical exercise. Blood perfusion has the additional role of adapting to muscle's metabolic demands. Autonomic receptors control blood flow to the muscles. At rest blood flow is at normal levels that during exercise raise, after the vasodilation caused by local metabolites like lactate and potassium. The higher blood perfusion is capable of providing oxygen and nutrients to the working muscles as well as removing metabolic waste and heat.

Lastly, blood flow can be regulated according to the local activity of specific organs to ensure their proper function. Metabolically demanding organs such as the brain, heart and kidneys rely on autoregulatory mechanisms, or local control of blood flow, that affect perfusion. For instance, in the brain, neural activity triggers local vasodilation or vasoconstriction (widening or narrowing of blood vessels), in a process known as neurovascular coupling. This function ensures that appropriate blood perfusion is received in active regions, to meet their transient energy needs. Disruptions in neurovascular coupling have been linked to cognitive and neurodegenerative disorders. Similarly, disruptions in autoregulation of other organs have been linked to different pathologies and will be further analyzed in the next subsection as they highlight the clinical importance of blood perfusion.

For the definition and biological role of blood perfusion, the article by D. Matienzo and B. Bordoni [55] was a major influence, containing fundamental phenomena of the cardiovascular system.

4.2 Clinical relevance of blood perfusion

From the previous part on the biological role of blood perfusion, it is clear how perfusion reflects tissue viability and regeneration potential, metabolic demands and supports hemodynamic regulation of the body for proper organ and muscle. The clinical relevance of blood perfusion is strongly implied by its biological role. The following subsection intends to explore the clinical applications and further support the significance of blood perfusion measurements.

As previously demonstrated, blood perfusion is tightly linked with tissue oxygenation which is critical for normal functioning of the body. It is known since the early 20th century that increased blood flow doesn't necessarily mean better oxygen delivery to tissues, as this function depends on capillary geometry and transit time. As Østergaard [56] highlights, oxygen transport is influenced not only by the overall blood flow but also by the uniformity of capillary transit times (CTH). Faster blood flow could actually reduce oxygen exchange if CTH is high. This makes it clear that global blood flow is not a sufficient index of tissue viability, as regional tissue hypoxia can still occur. The paper also notes the correlation of health conditions like Alzheimer's and stroke with capillary dysfunction and suggest that CTH monitoring serve as a biomarker for microvascular health. In conclusion, traditional indicators of blood flow may not reflect the true oxygenation status of tissue, emphasizing the need for regional blood perfusion measuring for early diagnosis, prognosis and treatment assessment in different conditions.

Building on this Den Uil et al. [57] support the significance of microcirculatory blood perfusion in sustaining oxygen exchange and tissue function. Importantly, their review reveals that microcirculatory dysfunction in conditions like sepsis, hypovolemic shock, and cardiogenic shock can occur independently of global hemodynamic indicators, such as blood pressure or cardiac output. They further analyze, that capillary blood flow may not always be a reliable indicator of tissue oxygenation due to spatial and temporal heterogeneity. They conclude that functional capillary density (FCD), the number of perfused capillaries per area, correlates better with tissue viability. This emphasizes the need for blood perfusion imaging techniques rather than basic measurement methods.

Monitoring perfusion is essential for the prognosis and treatment of numerous diseases. Observing the changes of microvascular networks can work as a factor of disease progression and provide significant information for different health conditions. In the section of biomedical applications of speckle metrology, some cases related to perfusion have already been reviewed. Speckle metrology has the capability to track motion and deformation. In the case of wound assessment, for example, measurements highlight the differences of the affected tissue compared to healthy samples. Essentially, these differences correspond to vascular damage -among other physiological changes- that are captured as motion in living tissue. From this perspective, tissue viability and damage evaluation, is a group of applications that blood perfusion monitoring has been proven valuable for prognosis and evaluation of treatment effectiveness.

Perfusion's biological role extends from systemic to organ-specific as well. One such example is cardiology, where its clinical relevance is particularly critical.

Measurements of myocardial blood flow are effective for evaluating coronary artery disease, myocardial ischemia and tissue viability. Importantly, as Camici and Rimoldi [58] demonstrate, abnormalities in myocardial perfusion can appear even before observable stenosis. Their study shows that PET-based perfusion imaging can detect early coronary microvascular dysfunction, a condition associated with risk factors like diabetes, hypertension, and hypercholesterolemia. Beyond its value in prognosis, they also find perfusion measurements effective for treatment selection and evaluation, as well.

Furthermore, perfusion measurement finds clinical application in cerebral conditions. According to Demeestere et al. [59] perfusion MRI and CT are routinely used to assist the treatment of ischemic stroke. Through perfusion imaging doctors can track the ischemic core and surrounding penumbra and decide on reperfusion therapies which is especially important when the exact onset time of stroke is unknown. Therefore, real-time monitoring guides personalized treatment and improves the patient outcome.

A similarly important relationship between perfusion and organ function is apparent in the lungs, where oxygenation depends on the behavior between airflow and perfusion. As Powers and Dhamoon [53] explain, the ventilation/perfusion ratio must be optimal for effective gas exchange while clinical imbalances are known to effect blood oxygenation despite normal respiratory function. Some of those conditions include pulmonary embolism and chronic obstructive pulmonary disease.

Finally, the two clinical settings where perfusion monitoring is most essential are critical care and surgery. In such settings, perfusion monitoring ensures optimal clinical outcomes while assessing hemodynamic stability. Specifically, an early indicator of circulatory status is peripheral perfusion, which is linked with oxygen delivery and shock progression but is rather more sensitive than systematic perfusion measurements. Falotico et al. [60] demonstrates how peripheral perfusion is often the first region that hypoperfusion can be noticed during circulatory failure and the last to recover during resuscitation. They also explain that even though clinical assessments like capillary refill time (CRT) and skin temperature gradients, has been considered subjective, they are being reinforced by optical technologies to provide real-time, non-invasive evaluation. Such technologies are reflected and transmitted light sensors as well as near-infrared spectroscopy that have advanced peripheral perfusion measurement. These methods offer shock severity evaluation, can monitor fluid resuscitation and aid in personalized treatment as well as reduce mortality in septic patients compared to lactate-guided strategies.

Perioperative perfusion, on the other hand is equally important, especially in surgeries where uninterrupted blood supply is required for tissue viability or when occlusion is necessary. For example, oculoplastic reconstructive surgeries require perfusion to be maintained in flaps and grafts (tissue transplants) to prevent ischemia and ensure healing. Berggren et al. [61] reviewed several modern imaging techniques that are increasingly employed to evaluate tissue viability during oculoplastic procedures. Another example is cardiac surgeries. Li et al. [62] used ICG angiography to assess graft perfusion during coronary artery bypass procedure which offered real-time surgical decision-making.

In conclusion, blood perfusion is a central physiological parameter that reflects tissue health and systemic function. Its measurements track transitions from normal, healthy

states to pathological conditions such as ischemia, improper healing and systemic shock. It serves as indicator of underlying problems in several contexts including wound healing, cardiac and respiratory evaluation, stroke assessment and critical care. In addition, the transition from empirical perfusion assessment to image-guided, quantitative techniques has further improve its usefulness in modern medicine.

Chapter 5

Non-speckle methods for measuring blood perfusion

Given the effective role of blood perfusion as an indicator of numerous health issues and the clinical importance that was highlighted in the previous section, there has been a growing demand for reliable, non-invasive method to measure it. The reverse is also true; research on the various measuring techniques of blood flow has emphasized the clinical need and contributed on our improved understanding of human physiology too, especially throughout the early development. From the start of 19th century, there was major effort for the establishment of novel concepts in this field as well as the advancement of existing methods a while later. Today, an ideal perfusion imaging technique should be fast, label-free, sensitive to microvascular changes, and applicable in both research and clinical settings. Blood perfusion techniques are based on different principles, each with their own advantages. This section is divided in subsections according to the operating principle of each method and aims to review the most advanced and popular techniques that define the state of the art in this field.

5.1 Ultrasound-Based Techniques

5.1.1 Doppler Ultrasound

One of the most established non-invasive techniques for measuring blood perfusion is Doppler Ultrasound. It utilizes high-frequency acoustic waves whose frequency is captured after interacting with the sample. The principle behind its operation is that frequency shifts occur when sound is reflected from a moving source. The resulting shift not only provides information about the velocity but also about the direction of blood flow. The Doppler shift is related to blood flow velocity according to the following relationship:

$$V_{\mathrm{D}} = \frac{\mathrm{c} f_{\mathrm{D}}}{2 f_0 \cos\theta}$$

Where V_{D} is blood flow velocity, c is the velocity of sound, f_0 is the irradiated ultrasound frequency, f_{D} is the Doppler shift frequency of the received sound signal and θ is the angle of placement of the transducer with respect to the blood vessel.

There are several different types of Doppler ultrasound flowmeters, including continuous wave (CW), pulsed wave (PW) and color Doppler imaging. CW is best suited for high-velocity flow and while commonly used to detect severe arterial stenosis, it doesn't support depth resolution. PW allows depth-specific flow measurement but it is limited by velocity aliasing, making it more suitable for medium-sized vessels. Color Doppler Imaging, on the other hand, overlays real-time velocity and directional values providing vascular maps that are especially useful in the detection of vascular abnormalities.

While Doppler Ultrasound remains widely used for vascular diagnostics, its limited spatial resolution and inability to image capillary-level perfusion reduce is suitability for microcirculation assessment.

5.1.2 Contrast-Enhanced Ultrasound (CEUS)

Contrast-enhanced ultrasound was developed to overcome the limitations of standard Doppler ultrasound in visualizing microvascular perfusion. It relies on the injection of microbubble agents that increase the intensity of Doppler signals for several minutes after their injection. The microbubbles have a diameter between 1 and 5 μm and are approximately 1000 times more reflective than body tissue while they traverse the microcirculation. The technique allows for dynamic perfusion assessment through time intensity curve analysis and the evaluation of parameters such as peak enhancement (PEAK) and time to peak (TTP) enable quantifiable measurements of perfusion. CEUS outperforms Doppler ultrasound and has proven effective in deeper tissue layers and identifying perfusion in cases like skeletal muscle and peripheral limbs where conventional ultrasound is ineffective. While CEUS offers a valuable non-invasive option, the need for intravenous contrast administration and careful timing make affects its accessibility compared to standard Doppler systems.

5.2 Optical Techniques

5.2.1 Near-Infrared Spectroscopy (NIRS)

Near-infrared spectroscopy (NIRS) quantifies how much light is absorbed by hemoglobin, an oxygen-carrying protein present in red blood cells. The method relies on near-infrared light (700–900 nm) since it can penetrate deeply enough (several millimeters) to reach blood vessels and interact with both oxygenated and deoxygenated hemoglobin. The technique requires multiple wavelength illumination because the two forms of hemoglobin absorb light differently across the light spectrum. By analyzing their differential absorption, the method can determine the relative concentrations of hemoglobin forms and enables the calculation of regional oxygen saturation (StO_2) and total hemoglobin concentration in the measured volume.

Even though NIRS is widely used to monitor perfusion-related trends in both clinical environments and research, and is especially common in cerebral and muscle tissue application, it does not directly measure blood perfusion. Unlike any other technique reviewed, NIRS cannot calculate blood velocity or motion. However, an indirect evaluation of blood perfusion is possible through monitoring the delivery and use of oxygen by tissue. It is proven an effective tool for identifying ischemic risk or evaluating medical interventions, but is limited by shallow penetration depth, low spatial resolution and inability to provide absolute perfusion measurements.

5.2.2 Indocyanine Green Fluorescence Imaging (ICG)

Indocyanine Green (ICG) fluorescence imaging is an optical technique that takes its name from the dye that its operation principle is based. The ICG dye is a water-soluble, near-infrared fluorophore that gets injected into the bloodstream and binds to plasma proteins. The imaging method requires a light source near 800nm that excites the particles of the dye to emit fluorescence that can be detected by near-infrared cameras.

The technique is extremely helpful for evaluating superficial blood flow and is well-established in applications like surgery, burn depth assessment, gastrointestinal anastomosis integrity, and flap viability evaluation. It is particularly useful in aiding intraoperative decisions because of its ability to deliver fast, high-contrast visual feedback. Even though it is adopted in medical diagnostics and provides high spatial resolution with clear perfusion mapping, the technique faces a number of drawbacks. Some of the most restricting being the need for intravenous dye injection, the low temporal resolution, and the limitation on repeated use because of the pharmacokinetics of the dye. Nevertheless, ICG fluorescence imaging is still a strong and useful technique for assessing tissue perfusion in different medical scenarios.

5.2.3 Laser Doppler Imaging (LDI)

Laser Doppler Imaging is a technique that was already included in parts of the thesis due to its common comparison and similarity with LSCI in blood perfusion applications. It is an optical technique that uses coherent laser light but does not involve speckle-based computations. Instead, it shares its operational principle with Doppler ultrasound but utilizes light instead of sound waves. LDI is a development of the earlier Laser Doppler Flowmetry which was limited to single-point measurements. LDI builds upon LDF by scanning a ROI and using pointwise calculations to create a two-dimensional map of tissue perfusion.

LDI is another well established-method in several applications including burn depth evaluation, skin perfusion monitoring, and vascular research and is particularly useful for assessing superficial blood flow. The technique is non-invasive and does not involve any contrast chemicals offering the benefit of application on damaged or sensitive tissue. On the other hand, the comparatively long acquisition time of the scanning process is a disadvantage that makes it less suitable for imaging of moving tissue or abrupt physiological changes. Even so, LDI is still a popular and trustworthy method for determining superficial perfusion in both experimental and clinical contexts.

5.2.4 Hyperspectral Imaging (HSI)

Hyperspectral imaging is an optical technique that determines spectroscopy values of hemoglobin. The system uses a spectrometer to capture often hundreds of narrow spectral bands of visible light that are reflected from the tissue. Data from the collected light is then processed to assess tissue characteristics and stored in three-dimensional

structures known as hypercubes that contain two spatial and one spectral dimension. This results to a full reflectance spectrum for each pixel in the image.

This method is a conceptual successor of NIRS that extends its principle of wavelength-dependent absorption analysis from pointwise measurements to full-field analysis using a broad spectrum of light. Similar to NIRS, hemoglobin is the primary chromophore of interest, and the analysis is based upon the way the two forms (oxy or deoxyhemoglobin) absorb light depending on the wavelength. The method estimates hemoglobin distribution, tissue oxygenation, and other perfusion-related parameters by examining each pixel's spectral signature.

HSI is limited by light’s penetration depth which approximately reaches 1 to 2mm into the tissue. With that said, it is a powerful tool for assessing perfusion and vitality of superficial tissue due to its non-contact and label-free nature. It has been applied in surgical guidance, tumor margin assessment, flap monitoring, and wound evaluation. On the down side, HSI systems are complex and require the collection and processing of large amounts of data that makes it slow and computationally expensive. Nevertheless, HSI is a developing and promising method for wide-field, non-invasive perfusion monitoring in both clinical and research contexts.

5.3 Magnetic Resonance-Based Techniques

5.3.1 Perfusion MRI

Perfusion MRI is a collection of methods that use magnetic fields and radiofrequency pulses to analyze the movement of water molecules or contrast chemicals in order to determine blood flow. This method exploits the nuclear magnetic resonance principle according to which hydrogen nuclei are aligned by a strong magnetic field. Short radiofrequency pulses are emitted by the system that disturb hydrogens alignment. Protons experience phase shifts that depend on how far they have traveled from the application point of the RF pulses. Faster flowing protons will undergo greater phase shifts and hence a measure of the phase shift gives information about the blood flow velocity.

There are two primary categories of perfusion MRI, contrast based and non-contrast methods. Contrast based methods require the injection of a contrast agent in the bloodstream. The most popular is Dynamic Susceptibility Contrast MRI (DSC-MRI) is and uses a gadolinium-based contrast agent to monitor the changes in signal that take place as the agent moves through the microvasculature. The non-contrast techniques include Intravoxel Incoherent Motion (IVIM), which uses diffusion-weighted imaging to analyze microvascular flow; Arterial Spin Labeling (ASL), which uses magnetic labeling of arterial blood water as an endogenous tracer; and Blood Oxygen Level Dependent (BOLD) imaging, which tracks changes in oxygenation and can indirectly reflect perfusion, especially in the brain.

Perfusion MRI is capable of absolute quantitative measurements, usually expressed in milliliters per 100 grams of tissue per minute. This makes it very useful for tumor characterization, stroke imaging, and assessing the effectiveness of treatment. The

primary drawbacks are the intricacy, lengthy acquisition periods, and restricted availability in contrast to portable optical methods. For non-invasive perfusion imaging, MRI is still one of the most accurate and instructive techniques available.

5.4 Nuclear-Based Techniques

5.4.1 Positron Emission Tomography (PET)

Positron Emission Tomography is the most widely used nuclear based method which measures perfusion by detecting pairs of gamma rays released during the decay of a positron-emitting radiotracer. The most common tracers, radioactive substances, used for perfusion imaging is $H_2{}^{15}O$, ^{13}N-ammonia, and ^{18}F-flurpiridaz, which circulate in the bloodstream and allow the mapping of regional blood flow. The PET scanner detects the gamma rays and creates a three-dimensional image of the concentration of the tracer throughout the tissue. Absolute perfusion values can be computed using this data which are usually expressed in milliliters per minute per 100 grams of tissue.

PET is frequently used in heart, brain, and oncological imaging and is regarded as one of the most accurate methods for measuring perfusion. It enables functional imaging even in deep tissue and offers exceptional sensitivity. Despite its high cost, restricted availability, ionizing radiation exposure, and the need for on-site or adjacent radiopharmaceutical production, PET remains the gold standard for perfusion studies and clinical situations when accurate functional evaluation is essential.

As a conclusion, there is a wide variety of options in the field of blood perfusion measuring. The section emphasizes on the diversity of the approaches, each offering distinct advantages on clinical or research scenarios. There are options like PET and perfusion MRI which are the golden standard methods for quantitative imaging and some others like ICG fluorescence, NIRS and CEUS that provide real time measurements without complex set-ups. This range that spans from absolute measurement to real time applicability, further extends to methods like LDI and Hyperspectral Imaging that are entirely non-contact without the need for contrast agents. Despite their differences, all these methods have a place for specific clinical or research needs and reflect the increasing demand for reliable perfusion assessment.

This last section of the general part was guided by the review of Jayanthy a K and Sujatha Narayanan [63] on blood flow measuring techniques and the more recent and specific review of Kirsten F. Ma et al. [64] on tissue perfusion assessment of patients with peripheral arterial disease.

Specific Part

The general part of the thesis laid the theoretical and technological foundation for our topic of focus Laser Speckle Contrast Imaging (LSCI) applied to blood perfusion. On the previous section, the techniques that dominate the field of perfusion imaging were reviewed. PET, MRI, Doppler ultrasound are all widely used in clinical environments but their limitations in cost, speed or invasiveness reveal that there is always a need for simpler and more accessible approaches.

In this context LSCI stands out as a promising approach, being entirely non-contact, real time and label-free, which means that there is no need for external contrast agents injected in the blood stream. While the standard implementations provide relative perfusion measurements, more advanced versions such as multi exposure LSCI have been able to provide quantitative blood perfusion estimates. This is a significant achievement when combined with the method's cost effectiveness and ease of use, all essential requirements are met for LSCI to take a leading role in perfusion imaging.

The specific part of this thesis is built upon the experimental evaluation of LSCI which consists of 3 phases. In the first two, we use models to test the accuracy of the technique in controlled conditions, in order to later investigate its capabilities in blood perfusion monitoring. First, LSCI is used to monitor periodic motion and capture stationary oscillations, aiming to calibrate the configuration and evaluate speckle contrast in drum tests. Second, we examine the correlation between contrast and physical displacement and evaluate its performance with known frequency oscillations using a woofer speaker. Finally, we perform occlusion-reperfusion experiments to assess perfusion sensitivity in human skin tissue. This series of experiments was designed to validate the technique and assess its performance with different types of motion and vibration. While the ultimate goal is the use of LSCI in skin perfusion monitoring, the earlier phases were not chosen with a sole purpose of calibrating the equipment and validating the algorithms. We also explore a use case – surface vibrations and stationary oscillations – that aligns with the nature of the method and seems promising and generally unexplored in the existing literature.

LSCI is a method that falls under laser speckle metrology and therefore its motion measurements are based on the decorrelation of speckle. It is an imaging-based pointwise technique that utilizes statistical image manipulation to acquire motion estimates. It relies on a simple and cost-effective optical configuration that requires only a viewing system and a coherent beam. Sometimes optics like filters, polarizers and diffusers are also equipped before or after the sample for enhancing the image and suit the needs of specific applications. Since its development, it has been constantly improving, for the last three decades, in terms of algorithms and is benefited by the technological improvements in computational power and optics.

The operational principle of LSCI is the analysis of speckle contrast, a statistical index that reflects the intensity fluctuations of speckle patterns. Intensity fluctuations and contrast is known to be related with the movement of the sample. Before moving into the experimental arrangement and results, it is necessary to establish why and how speckle contrast can be used to reflect blood flow. For that reason, the next section presents a detailed statistical analysis of speckle behavior, laying out the theoretical

basis which justify the use of contrast as a perfusion indicator. This foundation will guide both the interpretation of our results and the design choices that follow.

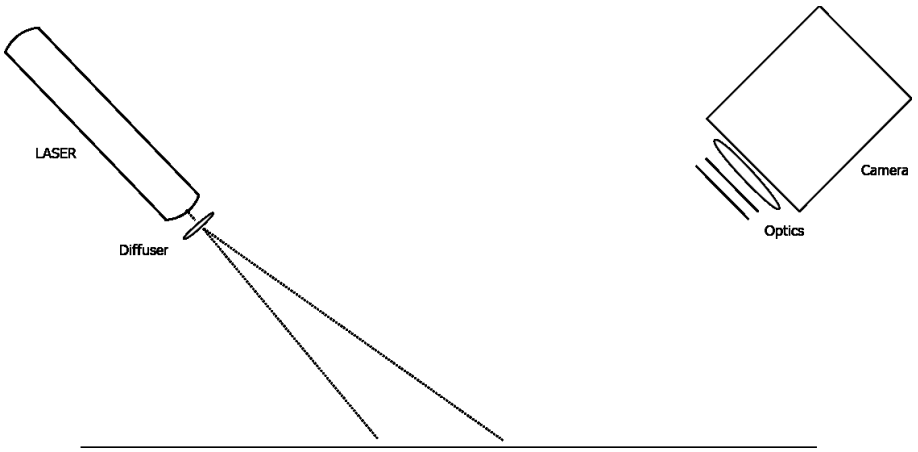

Figure 6.1: Optical configuration of Laser Speckle Contrast Imaging

Chapter 6

Statistical analysis

6.1 Foundational statistics

One defining characteristic of speckle is its randomness. Despite originating from deterministic physical processes, light waves interacting with surface features results in a chaotic distribution of intensity. This defining characteristic is presenting a challenge for precise analysis and interpretation. To address this challenge, statistical approaches have been developed. Goodman [65] first developed a detailed theory, introducing the speckle contrast K, one crucial parameter used in the statistical analysis of the phenomenon, which is an index commonly used to describe the degree of speckle's development.

Mathematically, contrast is defined as the normalized standard deviation of intensity fluctuations within a speckle pattern.

It is calculated as the ratio of the standard deviation σ devided by the mean intensity $\langle I \rangle$ of the speckle pattern: $K = \frac{\sigma}{\langle I \rangle}$

Fontelle [7] analyzed the statistics of speckle following Goodman's work providing some details on how contrast behaves on a static surface.

Assuming a perfectly diffusing surface with Gaussian distribution of surface height fluctuations, highly coherent, single-frequency laser light and linear polarization, it can be proven that speckle contrast is equal to 1 which is the maximum value that it can

obtain. This is proven by the relationship that can be acquired between the standard deviation and the mean intensity of the speckle.

It is true that the light field at any point $P(x, y, z)$ in the observation plane is equal with the sum of all the components N corresponding to the wavelets reaching the point from the various parts of the surface.

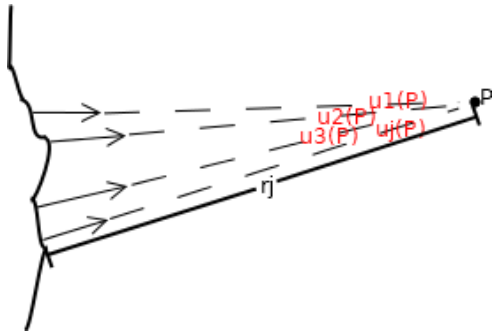

Figure 6.2: Wavelets being scattered from different parts of the surface, heading to point P

The contribution in the amplitude of the field at point P by any surface element, j, is:

$$U_j(P) = |u_j|e^{i\varphi_j} = |u_j|e^{ikr_j} \quad (1)$$

$k = \frac{2\pi}{\lambda}$ being the spatial frequency, r_j the random varying distance from the j-th scattering surface element to the point P as shown in Figure 2. $|u_j|e^{i\varphi_j}$ is the complex amplitude with $\varphi_j = kr_j$ representing the phase change as the wavelet propagates in the j-th path from the surface to the point P. Using Euler's formula $|u_j|e^{i\varphi_j}$ can be written also as $|u_j|\left(\cos(\varphi_j) + jsin(\varphi_j)\right)$.

The complex amplitude of the scattered field is given by:

$$U(P) = \frac{1}{\sqrt{N}}\sum_{j=1}^{N} U_j(P) = \frac{1}{\sqrt{N}}\sum_{j=1}^{N}|u_j|e^{ikr_j} \quad (2)$$

The above equation is considered a random walk in the complex plane because of the random phases φ_j.

Under the following assumptions:

- amplitude u_j and phase φ_j of $U_j(P)$ in each field component is statistically independent of each other and also independent of all other field components
- phases φ_j follow a uniform distribution on the interval $(-\pi, \pi)$, meaning that the surface is rough in comparison with the wavelenth
- the number of the scattering points N is very large (which is a condition for the central limit theorem to be true)

Goodman [65] was able to prove mathematically, according to the central limit theorem, that the real and imaginary parts of the resultant field are asymptotically Gaussian. The joint probability density function (PDF) for two Gaussian random variables is given by the formula:

$$P(x,y) = \frac{1}{2\pi\sigma_1\sigma_2\sqrt{1-\rho^2}}\exp\left(-\frac{1}{2(1-\rho^2)}\left[\frac{(x-\mu_1)^2}{{\sigma_1}^2}+\frac{(x-\mu_2)^2}{{\sigma_2}^2}+\frac{2\rho(x-\mu_1)(x-\mu_2)}{\sigma_1\sigma_2}\right]\right)$$

For the real and the imaginary part of the field though it is true that $\rho = 0$ because they are statistically independent and $\mu = 0$ as the Gaussian distributions have a zero mean. Moreover, both parts share the same standard deviation $\sigma = \sigma_r = \sigma_i$, so the joint PDF for them is given by:

$$P_{(r,i)}(U^{(r)}, U^{(i)}) = \frac{1}{2\pi\sigma^2} exp\left[-\frac{1}{2}\frac{\left(U^{(r)}\right)^2+\left(U^{(i)}\right)^2}{\sigma^2}\right] \quad (3)$$

Where

$$\sigma^2 = \lim_{N\to\infty}\sum_{j=1}^{N}\frac{\langle|u_j|\rangle^2}{2} \quad (4) \qquad \text{and} \qquad U^{(r)} = \sqrt{I}\cos\varphi\,,\ U^{(i)} = \sqrt{I}\sin\varphi \quad (5)$$

Another implication of the central limit theorem, is that the intensity distribution follows a negative exponential law, while the phase a uniform distribution in $[-\pi, \pi]$. Their PDFs are:

$$P(I) = \frac{1}{\langle I\rangle} e^{-\frac{I}{\langle I\rangle}}\ for\ I \geq 0 \quad (6)$$

$$P(\varphi) = \frac{1}{2\pi}\ \ for -\pi \leq \varphi \leq \pi \quad (7)$$

Where $\langle I\rangle$ in (6) stands for the mean intensity of speckles.

As for the moments of intensity, they can be derived by:

$$\langle I^n\rangle = \int_0^\infty I^n P(I)\,dI = \int_0^\infty I^n \frac{1}{\langle I\rangle} e^{-\frac{I}{\langle I\rangle}}\,dI$$

Let $x = \frac{\langle I\rangle}{I} \Rightarrow I = x\langle I\rangle,\ \ dI = \langle I\rangle dx$

$$\langle I^n\rangle = \langle I\rangle^n \int_0^\infty x^n e^{-x}\,dx = \langle I\rangle^n n!$$

$$\langle I^n\rangle = n!\,\langle I\rangle^n = n!\,(2\sigma^2)^n$$

If we use the formula for $n = 2$, we get the second order moment:

$$\langle I^2\rangle = 2!\,(2\sigma^2)^2 = 2!\,\langle I\rangle^2$$

$$\langle I^2\rangle = 2\langle I\rangle^2$$

Replacing this equation in the formula of variance we end up with:

$$\sigma^2 = \langle I^2\rangle - \langle I\rangle^2 = \langle I\rangle^2$$

Thus, taking into consideration the named assumptions, under ideal conditions, the standard deviation of the intensity variations in the speckle patters is equal to the mean

intensity. From definition of speckle contrast $K = \frac{\sigma}{\langle I \rangle}$, the resulting contrast is equal to unity, which is its maximum value and corresponds to static speckle.

Speckle contrast quantifies the level of blurring. A speckle pattern with the maximum value equal to 1 is known as fully developed and is observed without blurring. In reality, contrast tend to be less than one because the standard deviation of the intensity variations in the speckle patterns is less than the mean intensity. Low contrast values correspond to speckle patterns with relatively uniform, smooth intensity distributions, whereas high contrast values come from speckle patterns with vivid, apparent fluctuations in intensity across the surface. Therefore, it is obvious that contrast serves as a valuable metric for the evaluation of a speckle patterns and it is the foundation for various technologies including LSCI.

6.2 Characteristics of Speckle

After the analysis of speckle statistics and the establishment of contrast's relationship with blood velocity, it is essential to study the physical characteristics of speckle patterns that influence contrast. Understanding their impact is essential when designing a speckle-based imaging system and the experimental configuration, particularly in biomedical applications, like our own, where accuracy and repeatability are critical.

As described earlier speckle patters are subjective and are influenced by several factors, while objective speckles are considered only those that are captured without optics. A speckle pattern is highly sensitive to the configuration of the imaging system. Its properties, especially grain size and intensity fluctuations, are significantly influenced based on factors such as the sensor type (CCD, CMOS, etc.), the optical resolution, and especially the lens aperture. Likewise, the distance between the object and the detector, and the relative angle of observation, affect how speckle appears on the sensor. All these parameters contribute to the observed speckle contrast and must be carefully considered in any speckle-based measurement system.

Speckle is also dependable on the coherence of the light source. The coherence length of the light source determines the extent to which interference effects persist. Light sources with shorter coherence lengths lead to more random and rapidly changing speckle patterns, while longer coherence lengths produce more stable and coherent patterns. Generally, speckle contrast is inversely proportional to the coherence length.

Another factor influencing speckles is the wavelength of the light source which affects speckle size. Shorter wavelengths tend to produce smaller speckle grains that exhibit more rapid intensity fluctuations, resulting in higher contrast values. In comparison, longer wavelengths result in larger speckles with smoother patterns and lower contrast. On top of that, light's wavelength influences its scattering behavior as well as the way it finally interacts with optics. Because of that it is certainly an important factor that requires attention in imaging system design like LSCI.

Last but not least, movements play a critical role in laser speckle phenomena, particularly for applications like ours. When the surface being illuminated undergoes motion or vibrations, the resulting speckle patterns become blurred, leading to a

decrease in the standard deviation of intensity fluctuations while the mean intensity remains unchanged. The same is true for motion or vibration on the laser source itself. Minor movements of the illuminated objects cause the speckles to move along with them, maintaining correlation. However, larger motions result in a completely different formation of the speckle patterns, leading to decorrelation. Similarly, if individual scatterers within a stationary object are in motion, decorrelation occurs. A notable example is the movement of particles in a fluid and is the principle under blood perfusion measuring is possible using LSCI. This time-varying behavior was initially recognized by Stern [66] particularly in the context of blood flow analysis.

6.3 Analysis of time-varying speckle

In order to extract information about the motion of the scatterers, a relationship between their movement and the alterations that happen to speckle patterns must be established. It is expected that such a relationship exists between movement and contrast because standard deviation changes with motion. Therefore, deriving a formula linking the temporal statistics of speckle fluctuations to scatterer velocity is needed.

This article [66] by (among others) Briers which is also the author of the original 1981 paper on single-exposure speckle photography explains that the starting point was the formula by Goodman [67] in 1965:

$$\sigma^2{}_s(T) = \frac{1}{T}\int_0^T C_t{}^{(2)}(\tau)\, d\tau$$

This relationship connects the variance of a time-averaged speckle pattern and the temporal statistics of the fluctuations. This is the most commonly used equation, in LSCI methods, at least until 2008 and is a simplified version. Then, it was shown to affect the soundness of the results by Donald D. Duncan* and Sean J. Kirkpatrick [68]. In fact, this formula would be sufficient only for large exposure times as they pointed out.

The full formula which was on the original work of Goodman [69] published in 1985, is the starting point in this mathematical analysis:

$$\sigma^2{}_s(T) = \frac{2}{T}\int_0^T \left(1-\frac{\tau}{T}\right) C_t{}^{(2)}(\tau)\, d\tau \quad (1)$$

It is a function of the exposure time of the camera, T, the autocovariance of the intensity fluctuations in a single speckle, $C_t{}^{(2)}(\tau)$ (second order autocovariance). Let us also mention that the first time being used for LSCI was by Cheng and Duong [70] in 2007.

The variance $\sigma^2{}_s(T)$ measures the average of the squared deviations of the intensity fluctuations from their mean over the time exposure T. By integrating the autocovariance function $C_t{}^{(2)}(\tau)$ over the time interval from 0 to T, we are effectively summing up the covariances between intensity fluctuations at different time lags within that interval. Dividing by T normalizes the integral by the duration of the exposure, providing an average measure of the intensity fluctuations over that time period. So,

the formula essentially says that the variance of the intensity fluctuations observed by the camera during a time exposure T can be obtained by averaging the autocovariance of the intensity fluctuations over that time interval. Assuming that the random phenomenon follows a stationary process and has a Gaussian probability density function (PDF), it's possible to establish this relationship. In such cases, the autocovariance function ${C_t}^{(2)}(\tau)$ fully characterizes the temporal dependence structure of the random phenomenon.

${C_t}^{(2)}(\tau)$ is defined as follows:

$$ {C_t}^{(2)}(\tau) \stackrel{\text{def}}{=} \langle (I(t) - \langle I \rangle_t)(I(t+\tau) - \langle I \rangle_t) \rangle_t $$

Where $I(t)$ is the intensity at time t, τ is the time lag, $\langle\ \rangle_t$ is the time-average.

While from the definition of Standard deviation squared (which is equal to the variance) ${\sigma^2}_s(t)$ we get the following relation:

$$ {\sigma^2}_s(t) \stackrel{\text{def}}{=} \langle (I(t) - \langle I \rangle_t)^2 \rangle_t $$
$$ = \langle \left(I^2(t) - 2I(t)\langle I \rangle_t + {\langle I \rangle_t}^2 \right) \rangle_t = \langle I^2(t)\ \rangle_t - 2\langle I \rangle_t \langle I \rangle_t + {\langle I \rangle_t}^2 = $$
$$ \langle I^2(t)\ \rangle_t - {\langle I \rangle_t}^2 \quad (2) $$

Another definition needed is the normalized autocorrelation function of a field ${g_t}^{(1)}(\tau)$:

$$ {g_t}^{(1)}(\tau) \stackrel{\text{def}}{=} \frac{\langle E^+(t)E^-(t+\tau) \rangle_t}{\langle I \rangle_t} $$

Where $E(t)$ is the Field at time t, and $E(t) = E^+(t) + E^-(t)$. Intensity $I(t) = E^+(t)E^-(t)$ meaning that is equal with $|E(t)|^2$.
The above relationships reveal that $E^+(t)$ and $E^-(t)$ are Hermitian conjugates between them and synthesize the field. Their adaptation in the theory, indicate that the field can be divided to complex parts that are also convenient for the computations.

The normalized autocorrelation function ${g_t}^{(1)}(\tau)$ depends on the velocity distribution of the scattering particles and the proportion of photons that are Doppler-shifted. Hence, to estimate the average velocity from a single-exposure image, the fraction of Doppler shifted photons as well as the velocity distribution must be either known or assumed.

At this point, we will proceed to make the analysis specific to blood perfusion and include a specific model for the motion of scatterers in blood flow. The following statistical analysis assumes an autocorrelation function of the electric field that corresponds to the moving particles in human tissue.

We assume all photons are being Doppler-shifted and a Lorentzian velocity distribution. Assuming that, the normalized autocorrelation function of the field, ${g_t}^{(1)}(\tau)$ is exactly negative exponential:

$$ {g_t}^{(1)}(\tau) = e^{-\frac{|\tau|}{\tau_c}} \quad (3) $$

Here, τ_c represents the characteristic correlation time associated with the Lorentzian velocity distribution. This correlation time is related to the width of the Lorentzian distribution and provides a measure of how quickly the autocorrelation function decays

with increasing time delay τ. In this occasion, the exponential decay reflects the decay of correlation between intensity fluctuations of the speckle pattern over time, which is driven by the velocity distribution of the scattering particles and the proportion of Doppler-shifted photons. It will be demonstrated that this decay rate and the correlation time τ_c is linked with the velocity of the scattering particles and provides a calculation for the average velocity from a single-exposure image.

In this analysis, the Siegert relationship is assumed to hold, which is valid under the assumption of Gaussian statistics. The Siegert relationship states:

$$g_t{}^{(2)}(\tau) = 1 + \left|g_t{}^{(1)}(\tau)\right|^2 \quad (4)$$

Where $g_t{}^{(2)}(\tau)$ is the normalized autocorrelation function of the intensity:

$$g_t{}^{(2)}(\tau) \stackrel{\text{def}}{=} \frac{\langle I(t)I(t+\tau)\rangle_t}{\langle I\rangle_t{}^2}$$

From the above definition, using the equations (1), (2) ,(3) and (4) we can extract the following equation assuming stationarity. Stationarity ensures that the statistical properties of the random process, such as the autocorrelation function, do not vary with time. Stationarity simplifies the analysis by allowing us to treat the process as being time-invariant, meaning $I(t) = I(t+\tau)$:

$$C_t{}^{(2)}(\tau) = \langle (I(t) - \langle I\rangle_t)(I(t+\tau) - \langle I\rangle_t)\rangle_t = \langle (I(t) - \langle I\rangle_t)(I(t) - \langle I\rangle_t)\rangle_t$$
$$= \langle (I(t) - \langle I\rangle_t)^2\rangle_t$$
$$utilizing\ (2), \qquad C_t{}^{(2)}(\tau) = \sigma^2{}_s(t) = \langle I^2(t)\,\rangle_t - \langle I\rangle_t{}^2 \quad (5)$$

$$utilizing\ (5), \qquad g_t{}^{(2)}(\tau) = \frac{\langle I(t)I(t+\tau)\rangle_t}{\langle I\rangle_t{}^2} = \frac{\langle I^2(t)\rangle_t}{\langle I\rangle_t{}^2} = \frac{C_t{}^{(2)}(\tau) + \langle I\rangle_t{}^2}{\langle I\rangle_t{}^2}$$
$$g_t{}^{(2)}(\tau) = \frac{C_t{}^{(2)}(\tau)}{\langle I\rangle_t{}^2} + 1 = c_t{}^{(2)}(\tau) + 1 \quad (6)$$

Where $c_t{}^{(2)}(\tau)$ is the normalized autocovariance.

By combining equations (4) and (6):

$$c_t{}^{(2)}(\tau) = \left|g_t{}^{(1)}(\tau)\right|^2$$
$$\frac{C_t{}^{(2)}(\tau)}{\langle I\rangle_t{}^2} = \left|g_t{}^{(1)}(\tau)\right|^2$$
$$C_t{}^{(2)}(\tau) = \left|g_t{}^{(1)}(\tau)\right|^2 \langle I\rangle_t{}^2 = \left|e^{-\frac{\tau}{\tau_c}}\right|^2 \langle I\rangle_t{}^2$$
$$C_t{}^{(2)}(\tau) = e^{-\frac{2\tau}{\tau_c}} \langle I\rangle_t{}^2 \quad (7)$$

$$utilizing\ (1), (7), \qquad \sigma^2{}_s(T) = \frac{2}{T}\int_0^T \left(1 - \frac{\tau}{T}\right) e^{-\frac{2\tau}{\tau_c}} \langle I\rangle_t{}^2\, d\tau =$$
$$= \frac{2}{T}\langle I\rangle_t{}^2 \left(\int_0^T e^{-\frac{2\tau}{\tau_c}}\, d\tau - \frac{1}{T}\int_0^T \tau e^{-\frac{2\tau}{\tau_c}}\, d\tau\ \right) =$$

$$= \frac{2}{T}\langle I\rangle_t{}^2 \left(-\frac{\tau_c}{2}\left[e^{-\frac{2\tau}{\tau_c}}\right]_0^T - \frac{1}{T}\left(-\frac{\tau_c}{2}\left[\tau e^{-\frac{2\tau}{\tau_c}}\right]_0^T - \frac{\tau_c{}^2}{4}\left[e^{-\frac{2\tau}{\tau_c}}\right]_0^T \right) \right) =$$

$$= \frac{2}{T}\langle I\rangle_t{}^2 \left(-\frac{\tau_c}{2}e^{-\frac{2T}{\tau_c}} + \frac{\tau_c}{2} - \frac{1}{T}\left(-\frac{\tau_c}{2}Te^{-\frac{2T}{\tau_c}} - \frac{\tau_c{}^2}{4}e^{-\frac{2T}{\tau_c}} + \frac{\tau_c{}^2}{4} \right) \right) =$$

$$= \frac{2}{T}\langle I\rangle_t{}^2 \left(-\frac{\tau_c}{2}e^{-\frac{2T}{\tau_c}} + \frac{\tau_c}{2} + \frac{\tau_c}{2}e^{-\frac{2T}{\tau_c}} + \frac{\tau_c{}^2}{4T}e^{-\frac{2T}{\tau_c}} - \frac{\tau_c{}^2}{4T} \right) =$$

$$= \frac{2}{T}\langle I\rangle_t{}^2 \left(\frac{\tau_c}{2} + \frac{\tau_c{}^2}{4T}e^{-\frac{2T}{\tau_c}} - \frac{\tau_c{}^2}{4T} \right)$$

$$\sigma^2{}_s(T) = \langle I\rangle_t{}^2 \left(\frac{\tau_c}{T} + \frac{\tau_c{}^2}{2T^2}\left(e^{-\frac{2T}{\tau_c}} - 1 \right) \right) \quad (8)$$

Finally utilizing the above relation, we can calculate the contrast:

$$K = \frac{\sigma}{\langle I\rangle} = \left(\frac{\tau_c}{T} + \frac{\tau_c{}^2}{2T^2}\left(e^{-\frac{2T}{\tau_c}} - 1 \right) \right)^{\frac{1}{2}}$$

This analysis was following the assumptions and computations of A. Fercher and J. Briers on the original technique of speckle contrast imaging SESP in 1981 [71]. With the improved eq. (1) by Goodman the relation of contrast with the velocity of scatterers is an accurate approach as proved by Donald D. Duncan* and Sean J. Kirkpatrick. [68]

In the original LSCI method, LASCA, a Lorentzian distribution was assumed, and this is followed above. However, this assumption is accurate for Brownian types of motion (unordered flow) and in our application this is the case for capillary flow. If the application is focusing on displaying large vessels, then this is a case of an ordered flow and is best described by a Gaussian distribution. Following the same analysis, assuming gaussian distribution, the resulting autocovariance is:

$$C_t{}^{(2)}(\tau) = e^{-2\left(\frac{\tau}{\tau_c}\right)^2} \langle I\rangle_t{}^2$$

Thus, the contrast is given by:

$$K = \frac{\sigma}{\langle I\rangle} = \left(\frac{\tau_c}{2T}\left(\sqrt{2\pi}\, erf\left(\frac{\sqrt{2}T}{\tau_c}\right) - \frac{\tau_c}{T}\left(1 - e^{-2\left(\frac{\tau}{\tau_c}\right)^2} \right) \right) \right)^{\frac{1}{2}}$$

According to the same paper of Duncan and Kirkpatrick [68] the results of both the Gaussian and Lorentzian estimations have limiting behaviors. They have observed that the actual correlation behavior is some mixture of the two statistically independent processes and they suggested a model given by a convolution of the Gaussian and Lorentzian line shapes, a Voigt profile.

Finally, there is another thing to clarify. Having linked contrast, exposure time and correlation time is not enough for a blood perfusion measurement. Scatterer's velocity V is assumed to be inversely proportional to correlation time τ_c. The relationship between correlation time and blood velocity broadly used is the one from the original paper of LASCA [72]:

$$\tau_c = \frac{\lambda}{2\pi V}$$

However, this is a speculative relationship introduced by the authors.

Duncan and Kirkpatrick [68] proposed using a better and physically realistic relationship from Goodman's work:

$$\frac{{C_t}^{(2)}(\tau)}{{\langle I \rangle_t}^2} = \left(\frac{2J_1\left(\frac{\pi D V_\tau}{\lambda z}\right)}{\left(\frac{\pi D V_\tau}{\lambda z}\right)} \right)^2$$

Where D is the pupil diameter and z the distance from the sample to the aperture or lens.

Contrast resulting by this relationship has a behavior that is intermediate between the Gaussian and Lorentzian solutions. Specifically, this form closely resembles the Lorentzian results for long time exposures and the Gaussian for the short time exposures. This confirms their assumption for the distribution function to have a Voigt profile. Following this approach, from the last formula the relationship between the decorrelation time and the velocity is:

$$V = \frac{\lambda z}{D \tau_c}$$

This expression is derived using airy disc analysis and is closely related to the velocity approximation by Yordanov et al. [73] that is used in the implementation of LSCI used in our experiments:

$$V = 0.41 \frac{\lambda}{NA \tau_c}$$

Where NA is the numerical aperture of the imaging system.

Chapter 7

Development & Evolution of LSCI

7.1 Introduction on LSCI

Now that the statistical theory supporting LSCI is described and the relationship between contrast and velocity of scatterers has been established, let us proceed on the way this relationship is practically applied in the software. These algorithms calculate localized contrast in neighborhoods of the raw speckle frames being captured. Therefore, clarification is needed on whether the contrast-velocity relationships remain valid when computed over spatial, temporal or spatiotemporal neighborhoods of the image. For this to hold, it is assumed that the speckle pattern is ergodic and locally stationary, in order that statistical parameters like mean intensity and standard deviation can be estimated from these small sample regions. Duncan and Kirkpatrick [68] demonstrated that under appropriate conditions, spatial or temporal analysis in windows provide reliable estimates and supported mathematically the validity of the assumptions.

Having clarified this, the next section presents the algorithms that make use of the relationships defined by the statistical theory. Since the establishment of the statistical theory, researchers tried to exploit the phenomenon in various applications. Single Exposure Speckle Photography (SESP) which was the analog precursor of LSCI was developed in 1981 and used film post-processing to compute contrast. LSCI is a digital technique that utilizes contrast and its been widely adopted in blood perfusion measuring, starting from its first implementation in the 90's that was used to measure human skin perfusion.

The goal of the following section is to explain the essence of the image processing in LSCI and review its algorithmic evolution towards the current state of the art. This is essential for our choice of implementation in the experimental part of this thesis.

Laser Speckle Imaging Techniques developed for blood flow imaging

Technique	Initialism	Year	Domain	Description
Laser Speckle Contrast Analysis	*LASCA*	1995	Spatial	Contrast is calculated in 1 frame over $n \times n$ pixel areas
Laser Speckle Imaging	*LSI*	2003	Temporal	Contrast is calculated in 1 pixel over m frames
Laser Speckle Flowgraphy	*LSFG*	2002	Spatial & Temporal	A technique with a modified definition of contrast using spatio-temporal neighborhoods

Spatial Laser Speckle Contrast Analysis	*sLASCA*	2007	Spatial & Temporal	Regular LASCA, temporally averaged
Temporal Laser Speckle Contrast Analysis	*tLASCA*	2007	Spatial & Temporal	Regular LSI, spatially averaged
Multi-Exposure speckle Imaging	*MESI*	2008	Spatial	Contrast is calculated in 1 frame over 7×7 pixels while using different exposure times T
Anisotropic Laser Speckle Imaging	*aLSCI*	2012	Spatial & Temporal	Contrast is calculated in m frames directionally over $n \times n$ pixels
Space-Directional Laser Speckle Imaging	*sdLSCI*	2018	Spatial & Temporal	Alteration of LSCI with different direction selection
Adaptive Window Laser Speckle Imaging	*awLSCI*	2021	Spatial & Temporal	Contrast is calculated in m frames directionally over windows with adaptive size
Adaptive Window Space Directional Laser Speckle Imaging	*awsdLSCI*	2023	Spatial & Temporal	Alteration of aLSCI with adaptive window size calculation

Table 1: Remarkable digital LSCI techniques

7.2 Spatial Contrast Algorithms

The first digital Laser Speckle Contrast Imaging technique LASCA, “was born” in 1995 by D. Briers and S. Webster [72]. They essentially implemented the digital version of an existing technique SESP, making it efficient and potentially capable of clinical use. It involved spatial domain analysis with the final map of velocity computed in means of local spatial contrast. This local contrast is determined within squares of size $n \times n$, in iterations traversing the entire array and computing σ as the standard deviation of the spatial intensity variations and $\langle I \rangle$ as the spatial average of the $n \times n$ area.

The algorithm which is also schematically explained in Figure 7. is computed by the following formula:

Using $K = \frac{\sigma}{\langle I \rangle} = \frac{\sqrt{\langle I^2 \rangle - \langle I \rangle^2}}{\langle I \rangle}$,

$$K_{i,j} = \frac{\sqrt{\langle {I_{i,j}}^2 \rangle - \langle I_{i,j} \rangle^2}}{\langle I_{i,j} \rangle}$$

$$K_{i,j} = \frac{\sqrt{\frac{1}{(n+1)^2}\sum_{x=i-\frac{n}{2}}^{i+\frac{n}{2}}\sum_{y=j-\frac{n}{2}}^{j+\frac{n}{2}} I^2{}_{x,y} - \left(\frac{1}{(n+1)^2}\sum_{x'=i-\frac{n}{2}}^{i+\frac{n}{2}}\sum_{y'=j-\frac{n}{2}}^{j+\frac{n}{2}} I^2{}_{x',y'}\right)^2}}{\frac{1}{(n+1)^2}\sum_{x=i-\frac{n}{2}}^{i+\frac{n}{2}}\sum_{y=j-\frac{n}{2}}^{j+\frac{n}{2}} I_{x,y}}$$

where $I_{i,j}$ the intensity of pixel i,j and $n+1$ the size of the square over which the contrast is calculated.

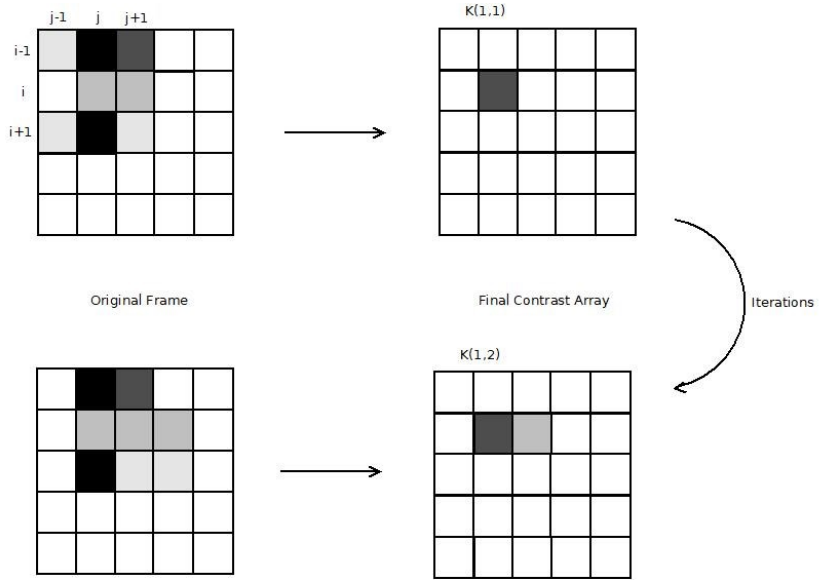

Figure 7.1: Graphical presentation of K computation in LASCA

After observing the presentation of the algorithm, it becomes obvious that the final image containing the information about contrast has way less effective spatial resolution. This is the main disadvantage of spatial domain analysis. The effective resolution will be averaged by the size of the n-sized windows and is equal to $\frac{l}{n} \times \frac{l}{n}$, considering the original frame was size l. Of course, temporal resolution with this kind of analysis will be the best possible, only determined by the hardware. The developers used 5×5 or 7×7 pixels for contrast computation which is still a popular choice, as lower values reduce the validity of the statistics, whereas larger numbers limit the spatial resolution of the technique.

7.3 Temporal Contrast Algorithms

The low spatial resolution of LASCA raised the interest of researchers to the development of other approaches, that do not involve spatial computations. LSI developed by Cheng et al. [74] is a technique using temporal domain analysis. In this context, σ is computed as the standard deviation of the temporal intensity variations

and $\langle I \rangle$ as the temporal average of m consecutive frames. LSI is the temporal equivalent of LASCA, considering that contrast is calculated in neighborhoods formed based on a pixel captured in a time sequence, instead of using multiple pixels in a single image. The algorithm computes contrast by the formula:

$$K_{i,j} = \frac{\sqrt{\langle {I_{i,j,t}}^2 \rangle_t - \langle I_{i,j,t} \rangle_t^2}}{\langle I_{i,j,t} \rangle_t}$$

$$K_{i,j} = \frac{\sqrt{\frac{1}{m+1}\sum_{l=t-\frac{m}{2}}^{t+\frac{m}{2}} {I^2}_{i,j,l} - \left(\frac{1}{m+1}\sum_{l'=t-\frac{m}{2}}^{t+\frac{m}{2}} I_{i,j,l'}\right)^2}}{\frac{1}{m+1}\sum_{l=t-\frac{m}{2}}^{t+\frac{m}{2}} I_{i,j,l}}$$

where $I_{i,j,t}$ the intensity of pixel i,j and $m+1$ the number of the frames from which contrast is calculated.

A direct observation from the formulas of LSI, is that spatial resolution of the resulted contrast map is exactly the same with the raw speckle image and depends only on the imaging system of the configuration. Temporal resolution, on the other hand, depends on the number of frames m, being used for the image processing. According to the researchers, in order to develop an algorithm with the same signal to noise ratio as the spatial algorithm, an m = 25 was needed. For this number of frames, they concluded that a linear relation between the inverse of contrast and the velocity of the scatterers was a good approximation ($U = \frac{1}{K}$), avoiding the use of complex statistical estimates.

Another direct result of the temporal computation, is that it fails to measure the contrast of stationary speckle patterns. The technique falsely computes a contrast equal to 0, when detecting no flow at all which is actually true only for really high velocities. Li et al. [75] used an alteration of LSI, known as Laser Speckle Temporal Contrast Analysis LSTCA, exploiting this property. They used, T = 5ms with an interval time of 25 ms that enabled blood perfusion imaging on an intact (and not thinned by any medical operation) rat skull. This achievement, was also performed real-time with a frame rate of 33 Hz. This study, also showed that the visualization of LSTCA offered better results on imaging the blood vessels, with respect to LASCA, because speckles on the detector consist of a stationary and a dynamic part. The stationary part is dependent only by the local properties of the skull which is temporally homogeneous. Such application is not possible by spatial algorithms which are influenced by the stationary part.

7.4 Spatio-Temporal Contrast Algorithms

sLASCA – tLASCA are two improvements of the regular LASCA and regular LSI, respectively, developed by Tan et al. [76]. Both techniques after calculating speckle contrast, involve some kind averaging of contrast to achieve better results.

sLASCA, is a spatially derived contrast method, using temporal frame averaging. Initially, contrast is calculated, as in standard LASCA, and then averaged in a number of frames that are predetermined. After the calculation of contrast $K_{i,j,n}$ using squares of pixels for the number of frames n needed for the averaging, the final contrast is calculated by the relation:

$$K_{sLASCA(i,j)} = \frac{\left(K_{i,j,1} + K_{i,j,2} + \cdots + K_{i,j,n}\right)}{n}$$

sLASCA provides a better viewing result because of the temporal averaging of the technique, maintaining partly the advantage of the temporal resolution and is more time-effective than temporal methods of contrast analysis.

tLASCA on the other side, is a temporally derived contrast method, that uses a spatial averaging in each frame. The technique uses regular LSI algorithm to extract the standard deviation and mean value for each pixel and calculate contrast temporally. After these computations, the spatial averaging takes place in each pixel, which is done using 3x3 pixel squares, in this implementation. The formula of the contrast is:

$$K_{tLASCA(i,j)} = \frac{1}{9} \sum_{r=i-1}^{i+1} \sum_{c=j-1}^{j+1} \frac{\sigma_{i,j,t}}{\langle I_{i,j,t} \rangle}$$

Due to the contrast computation by the LSI algorithm, tLASCA shares its major advantage. The contrast map created by the technique, has an effective spatial resolution with a small reduction comparing to the original, due to the window of averaging. Because spatial averaging is involved, a smaller number of frames is needed to achieve good results in the calculation of contrast.

tLASCA is found to achieve superior results comparing to sLASCA and of course regular LASCA, in objective and subjective quality, in processing time and in terms of error and statistical validity. It is shown, that the best viewing experience is produced by tLASCA for n = 10 and n = 16, followed by sLASCA for M = 3 with n = 4 and n = 10 for computations of large and small vessels, respectively. tLASCA has been proven to provide more consistent contrast value (after n = 10 or 16, ±8% error), and to provide better viewing experience. Regarding the processing time, tLASCA achieved the best results; for n = 16 it takes 5.3 s. to get the first statically stable contrast values for the first frame, and 0.3 s for subsequent frames. Once stability is achieved, tLASCA is 3.7 to 16.7 times faster than sLASCA.

There is another spatio-temporal method that initially was developed, using a modified definition of contrast. This refers to Laser Speckle Flowgraphy (LSFG) [77] which is not an LSCI technique with its strict definition, but it is included for its image processing algorithm that performs well and can be implemented to compute regular contrast. The method uses a spatio-temporal neighborhood consisting from a spatial window in a series of frames.

7.5 Multi Exposure Speckle Imaging

This technique is rather complicated, compared to others but is also a milestone for LSCI. MESI, or multi exposure speckle imaging is a technique developed by Parthasarathy et al. [78] They utilized the theoretical observation previously noted, by Cheng and Duong [70] and provided a theoretical model, attempting to eliminate the simplifications and neglects of LSCI theoretical models before them. Their work account for the presence of static scattered light that was previously neglected due to models relying of Siegert relationship which is applied on Gaussian statistics. In the presence of static scatterers, the fluctuations of the scattered field remain Gaussian but the intensity acquires an extra static contribution that was overlooked. They also provided a variable for the experimental noise and finally did not overlook nonergodic variance due to the ensemble averaging. The speckle pattern obtained from a completely static sample does not fluctuate. Hence the variance of the speckle signal over time is zero. However, the spatial (or ensemble) speckle contrast would be a nonzero constant due to spatial averaging of the random interference pattern produced. They also added this constant in their computations. Apart from their theoretical model, the multi exposure configuration of LSCI they developed, aims to compute the autocorrelation function, not to assume it. Multi-exposure imaging, utilizes multiple exposure times and experimentally calculates the contrast through the autocovariance function. This became possible because the distribution can be acquired when the decorrelation time τ_c is known. The estimation of τ_c is done experimentally by having it as a fitting parameter, since images are obtained at different time exposures. They optimized speckle imaging by all means previously noted. These improvements enabled quantitative measurements, providing real blood flow values rather than approximations or arbitrary units.

7.6 Anisotropic LSCI

All LSCI techniques developed until 2012 utilized isotropic algorithms for image processing. Meaning that, the method was applied uniformly regardless of the directional properties of speckle on the frame – all pixels were treated equally without considering the directional variations in the data. In blood perfusion imaging, raw laser speckle frames acquired, contain vessels in which blood moves towards a direction, thus the dynamic part of the image follows a path that can be detected. This was the idea behind anisotropic image processing aLSCI. Rege et. al [79] proposed aLSCI as a spatiotemporal method, that considers 4 different directions and computes contrast in a line neighborhood on the chosen angle. The four directions that get involved in the selection process are, $0°, 45°, 90°, 135°$ and are chose under the criterion of the least square error about the central pixel as the line segment rotates 180° around it. This is described by the following formula:

$$\arg[l_0] = argmin_{l\in 0°\to 180°}\left[\sum_{P\in l}\left(K_P - K_{P_0}\right)^2\right]$$

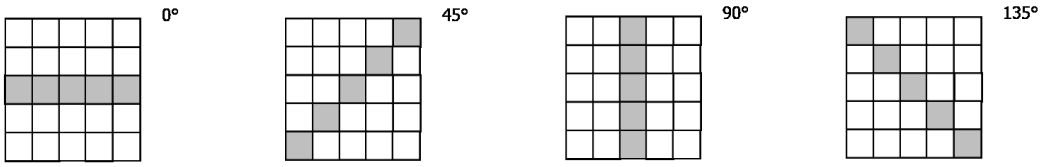

Figure 7.2: The considered directions in the image processing

After the selection of a direction line for each pixel, contrast is recalculated using the lines of pixels in a number of consecutive frames. The choice of a line in the direction of the flow was proven to make even the visualization of vessels with a diameter of one pixel possible.

A major improvement was done by Perez-corona et al. [80], with their alteration of the method called space directional LSCI. The authors suggested that the direction should be chosen in each specific raw speckle image before contrast is calculated, using the mean value of intensity in each neighborhood, rather than the central pixel's value, to avoid including noise in the computations. Most importantly, this new technique used another direction criterion. According to [81], the method was based on the observation that static parts of the raw speckle image consist of highly varying pixel intensities, while the dynamic parts, of highly similar intensities. Thus, choosing the direction with maximum variation for the calculation would result in static regions with increased contrast values, while dynamic parts would not be greatly affected by this, because of the similarity in intensities. The same four directions were considered using the maximum variance criterion.

The latest addition to anisotropic LSCI techniques was adaptive window space direction contrast method. In 2023 by Han et al. [82] developed a spatiotemporal method that uses an adaptive window for the spatial computation of contrast. The method involves the clustering of the image to groups of similar intensities that divide it to static and dynamic regions. Initially, the used an anisotropic diffusion filter, ADF, in the raw speckle frames that worked, eliminating noise without smoothing the edges of vessels. Furthermore, they proposed the use of 3 different criteria of direction selection corresponding to the static, dynamic and transition regions; maximum variance for the selection in static regions, median variance for transition regions and minimum variance for dynamic regions.

awsdLSCI was tested in a model experiment, and then an imaging of the distribution of rat cerebral blood flow CBF was performed. First of all, the authors concluded that using 3 consecutive frames was sufficient for the contrast computation, and there was no obvious difference between the results using 30 frames. Both in vivo and in vitro testing aim was to validate the method visualizing perfusion in different depths and used CNR to compare it with awLSCI, sdLSCI and LASCA. This new method achieved better spatial resolution, making imaging of small vessels possible, improved the contrast of dynamic, static, transition regions, and achieved greater noise attenuation. To quantify the results, it is worth mentioning that CNR values was increased as high as 163.80% and 239.29% comparing to sdLSCI and awLSCI respectively. These results were achieved in the maximum depth tested that was 500μm.

7.7 Further Development and Evolution

Briers et al. [83] noticed, related to performance of LSCI, that speckle size effects the results. Speckle size is found to be dependent on the laser wavelength λ, the f-number of the lens system $f_{\#}$ and the magnification M. The following equation relates the speckle size d with the latter three:

$$d = 2.44\lambda f_{\#} M$$

They observed that if the average speckle size is smaller than the aperture of the detector, there is speckle averaging, as more than one speckles are sampled in each pixel. As a result, the first-order statistics that the method is based, collapse, producing error in the computations. However, if the speckle size is much larger that aperture size, not enough speckles are sampled and therefore good statistics are not ensured too. They concluded that the error in contrast calculations is minimized when the speckle size is of the same order with pixel size. The most convenient way to control speckle size is the manipulation of the f-number of the lens. However, this leads to less amount of light reaching the camera which can be corrected by using neutral density filters.

Another important research from Yuan et al. [84] about the exposure time T of the camera took place. Apparently, the exposure time is linked with the noise induced in the measurements and the sensitivity of them. An increase of only 2ms in the exposure time can lead to an increased sensitivity of speckle changes. However, increasing T also results in more noise. They concluded that the optimal contrast to noise ratio was achieved with an exposure time of 5ms, using LASCA to measure perfusion in the brains of rodents.

Another optimization of the technique comes from Cheng and Duong [70] that were able to develop a time efficient computation, using an approximation of velocity. Instead of using the analytical contrast K relation they used the asymptotic approximation of $\frac{1}{K^2}$ that was shown to be linearly related to $\frac{T}{\tau_c}$, the blood flow index.

Finally, noise reduction is a subject that occupied several researchers, concerning LSCI. A study with notable results was conducted by Volker et al. [85] providing a way to decrease statistical noise in LSI. By utilizing a slowly rotating diffuser in the laser path, statistically independent speckle patterns develop on illumination surface. The principle is that while the diffuser rotates the temporal fluctuations will occur at time scale t0, choosing the exposure time to be much smaller than t0, speckle images will be statistically independent. In combination with normalizing the measurements using a number N of consecutive frames for contrast calculation they showed that the noise level was $\frac{1}{\sqrt{N}}$ %. Their results contained 4 times less noise, comparing to LASCA.

Chapter 8

Experimental Configuration

With the description and evolution of LSCI taken care of, we can now proceed to the main subject of the specific section, the experimental evaluation of the technique. This thesis investigates Laser Speckle Contrast Imaging as a technique for visualizing blood perfusion. We focused on implementing and validating the technique with well-structured experiments, but while designing the experimental procedures, the lack of access to animal models or clinical data, typical of integrated master's projects, lead us towards skin perfusion measuring. This application is non-invasive and ethically straightforward while offering significant clinical value. Some examples of its clinical importance have been reviewed on previous sections and include applications in wound healing, burn assessment and ulcer evaluation.

8.1 Experimental Scope and Rationale

Despite its clinical relevance, LSCI faces specific limitations when applied to skin perfusion, which in fact, are not encountered with other types of clinical applications, like retinal or intraoperative imaging. The creation of vascular maps on human skin is particularly challenging due to the multilayered complexity of vascular structures and the stationary nature of the skin surface. Actually, LSCI has been proven incapable of producing vascular maps without additional invasive procedures. Lately, optical clearing has been shown to assist LSCI's performance in skin perfusion and enable it to image microvascular structures. Some significant studies [86] [87] [88] [89] demonstrated significant advancements in visualizing cutaneous blood flow and vascular structures using this combination of optical clearing and LSCI. The researchers managed to reduce skin's scattering and increase imaging depth. Specifically, this was enabled by the application of OCAs such as PEG-400, glycerol and fructose.

The first of these studies, used skin models with varying concentrations of glycerol and intralipid (popular skin phantom), which resulted in better performance and opened the door for the upcoming studies on animals. Even though one study [87] addressed the safety issues and found no evidence of damage on the skin or internal organs after testing different substances, research in this area, is still in early stages. So far, all of research in optical clearing and LSCI, has been performed on animal subjects. In addition, medical precautions and oversight required for human trials are beyond the point of this thesis.

Given these limitations and ethical constraints and since, in our experimental work, non-invasiveness is an essential requirement, we decided to conduct occlusion-reperfusion experiments on human skin to assess LSCI's sensitivity in a skin-based application. This configuration might not provide vascular mapping but it is an established method for evaluating relative changes in blood flow and is well-suited to test the performance of speckle metrology techniques. Our objective was to provide a reliable implementation of LSCI and validate its performance under established

physiological settings, and gain a deeper understanding of the contrast–perfusion connection in a practical setting.

In this context, it worth noting that a quantitative analysis is not feasible. The measured contrast in skin is a result of multiply scattered light through dense capillary structures at varying depths. These conditions make it impossible to assign precise velocities to individual vessels or paths. For this reason, in our blood perfusion experiments, we adopted the asymptotic approximation of $V = \frac{1}{K^2}$, that was proposed by Cheng and Duong [70] and described on the previous section. It provides a consistent, monotonic relationship between velocity and speckle contrast, while providing relative comparisons through the experimental steps of each phase. In this work, using arbitrary units was both appropriate and following standard practice.

8.2 Overview of Experimental Phases

In order to validate the imaging system and the selected algorithms, we designed two phases of physical experiments, supporting our goal of applying LSCI in skin perfusion monitoring. In the first phase, we used LSCI to visualize stationary wave fields on the membrane of a drum. This not only served as a step of calibration but is also a novel application of the method. The ability to capture standing wave patterns using speckle contrast is largely unexplored in the literature and demonstrates the technique's sensitivity in a wide range of physical phenomena.

We extended this work in a second experimental phase aiming to quantify and further research controlled oscillatory systems. In the second phase, we investigated speaker membrane oscillations, aiming to link contrast values to known vibrational input. This enabled us to explore a quantitative scaling of the speckle response in relation to volume levels of the speaker, further validating our configuration and proving the reproducibility of the method.

Finally, in the third phase, we applied LSCI to biological tissue by conducting an occlusion–reperfusion test on the hand. This experiment served as the biological validation of our system, demonstrating its ability to detect useful changes in perfusion. Occlusion testing is a widely accepted protocol for assessing relative blood flow changes and is often used to evaluate the sensitivity of perfusion monitoring systems. In fact, occlusion experiments were a part of LASCA's, the initial LSCI method, laboratory testing. This final phase bridges the system's physical performance with its intended biomedical application and confirms its practical functionality under real-world conditions.

8.3 Initial Setup Challenges and Design Decisions

Although LSCI is known for its extremely simple setup, requiring only a laser source and a camera sensor, the process of calibrating the system was proven quite challenging. Let alone achieving reliable and high-quality results. Several practical limitations arose during the initial phases of the configuration testing. The most

immediate challenge was the method's extreme sensitivity to motion. LSCI could actually detect any movement on the sample's surface, due to its relation with the speckle pattern formation. While this makes the technique a really sensitive tool, it is a feature that can become a drawback, when attempting to isolate specific causes of movement which is essential in any imaging configuration. Contrast calculation was affected by any unintentional movement, even slight shifts in the setup or ambient vibrations and significantly impacted the results. This required the stabilization of every component in the optical path, including the camera, laser source, sample, and supporting structures.

Another challenge involved the laser illumination itself. Speckle quality and contrast were affected by glare and overexposure, especially on reflective surfaces like skin or synthetic membranes. These issues required adjustments to the laser source, figuring the appropriate power output needed, angle adjustments and the use of optics.

Different laser diodes were tested, including 5 mW, 50 mW, and 100 mW units at wavelengths of 633 nm and 635 nm. We needed sufficient illumination while also preventing pixel saturation from excessive laser power. Finally, the most powerful laser was selected in a combination with a cross-polarizer setup, which allowed precise control of the illumination and minimized glare. Combined with a diffuser, we succeeded uniform illumination that satisfied the system's requirements.

In our initial experiments, a significant challenge was encountered during the configuration of our drum setup that was caused by environmental light. We captured our first raw speckle frames using grayscale format (Mono8) that suited us well, in ways that will be further explained in the software section. In the initial contrast maps there were prominent noise artifacts and pronounce interference patterns that couldn't be explained, initially. These included visible outlines and surface characteristics of the membrane, such as discoloration, which were unrelated to actual motion or perfusion changes. Switching to Rgb24 format and an algorithm that isolated the red channel from the video, we discarded most light that does not come from the illumination source (635nm red Laser). This change resulted in contrast maps clear from those noise artifacts from which we concluded that the source of noise was ambient light in the lab that was especially disruptive in lower expose time values. Based on this observation, we continued the experiments in a completely dark environment, using the red channel of Rgb24 videos in order to ensure that most noise is eliminated from our results.

Let us note here that, Mono8 images were darker. Using only the red channel of the Rgb24 format was prone to glare causing error to our computation as pixels were saturated. To overcome this, we optimized our system with additional optics.

8.4 Drum Experiments

The phase of the drum tests was aiming at configuring basic aspects of LSCI, testing the proper functionality of the algorithms, as well as evaluating LSCI on monitoring stationary oscillations of the vibrating membrane.

Oscillations occurring on a circular membrane, like a drum's surface, are complex. The vibrations create dynamic waves and under these specific conditions-boundary effects of the membrane, evolve into stationary waves. When the drum is struck, waves created by the disturbance travel outward, reaching the edge of the membrane, where it reflects back towards the center. This interaction between the outgoing and incoming waves creates standing wave patterns. This patterns that are explained by wave interference, are composed by nodes, static areas of the membrane and anti-nodal areas that are dynamic. This is the reason behind our choice, of this use case for LSCI. The patterns are expected to appear as concentric rings and lines on the speckle maps with alternating velocities and static areas.

Stationary wave frequencies appearing on this physical phenomenon are really complex. The frequency of these oscillations depends on the physical properties of the drum. The simplest mode of vibration, the fundamental frequency, involves the entire membrane moving uniformly. However, higher-frequency harmonics can emerge, which are complicated patterns with additional nodal lines. During this phase, our primary goal was to evaluate whether our system, was sensitive enough to capture these oscillations, regarding frame rate. Drum vibrations involve a plethora of patterns and frequencies, making them difficult to predict in advance. Our expectation was that the system could detect some of these frequencies, potentially just the fundamental one, and visualize the stationary waves.

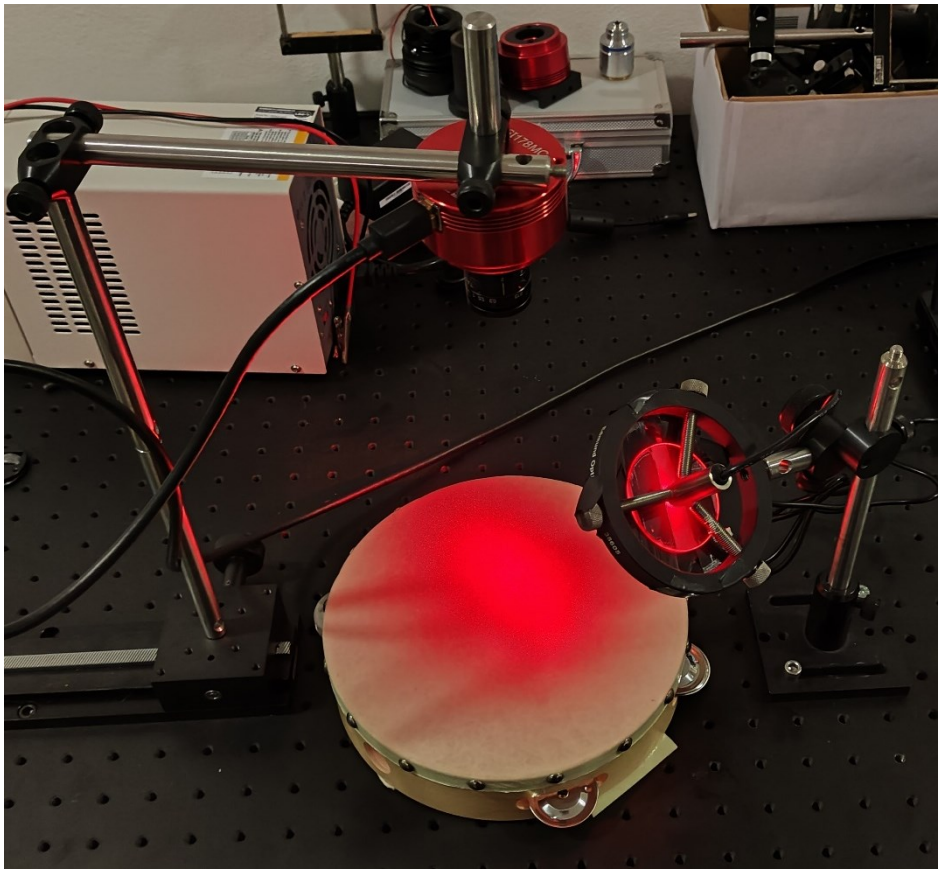

Figure 8.1: Drum LSCI setup. The images were captured by a CCD camera, illuminated by a powerful cross-polarized and diffused LASER.

8.4.1 Equipment

Figure 8.1 illustrates the experimental setup for our drum membrane tests. A drum with 20 cm diameter skin membrane is mounted to the workbench with double sided tape and used as our oscillator instrument.

A cross-polarized 100mW, 635nm diode LASER illuminated the upper part of the membrane. A diffuser was used to help distribute evenly the laser light across the surface, offering uniform illumination and reducing coherent noise in the speckle pattern. On top of it, a polarizer was placed to filter the light source and counter the glare, enhancing speckle contrast.

Our imaging setup consisted of 24-bit RGB CCD camera (ZWO ASI178MC, China) with a resolution of 3096 x 2080, using a manual iris lens (Tamron M112FM16, Japan). The imaging system was used with SharpCap 4.1 frame grabber that captures the videos of the drum. The algorithms ran on MATLAB 2024b on a Windows computer with 32 GB of RAM.

8.4.2 Imaging Procedure

During the drum experiments, videos of the relaxed membrane were captured to gain baseline contrast ranges. Afterwards, footage of a drum hit following a static state were captured as well as dynamic videos of the drum constantly being hit. Drum's stimulation was done with a drum stick, striking the lower middle part of the drum that is the reason behind capturing the oscillations in the upper part, in order to monitor the evolution of the disturbance. We started with powerful strokes and gradually reduced the power of the drum's hit, as well, to evaluate the sensitivity of LSCI.

During this phase, frames were captured in resolutions, from 1280x720 that succeeded a frame rate of 86 fps, to 1920x1080 with a stable frame rate almost equal to 60 fps. We experimented on the resolution to find out what could provide better insides on the oscillations and these two choices offered the best possible resolution to frame rate.

In addition, we tested exposure time values ranging from 1ms to 20ms, while anything higher was considered incapable to capture the drum's high frequencies.

8.4.3 Drum Setup Optimization

One critical parameter of LSCI is the camera's exposure time. This is an application depended parameter that requires optimization in order to capture intensity fluctuations on an appropriate pace and preserve statistical validity. While blood perfusion is an application well researched and the fitting exposure times are established, drum oscillations are widely unexplored with this technique and finding the right exposure time has a direct impact on the visibility of the stationary wave patterns. Through

comparative testing, we found that shorter exposure times, particularly around 1 ms, yielded the most distinct and reproducible contrast maps. These settings preserved the fine temporal fluctuations of the speckle pattern caused by the standing wave fields. In comparison, longer exposure times such as 5ms and above, resulted in averaging of the intensity fluctuations, blurring contrast maps and reducing the visibility of oscillations. This outcome differs from typical LSCI applications in blood perfusion, where higher exposure times are preferred and provide more accurate results. In the case of vibrational surface imaging lower exposure times were necessary to capture the rapid intensity fluctuations induced by membrane displacement.

Another important subject that was tested, is the approximation of velocity using contrast in arbitrary values. A popular conversion used in blood perfusion $\mathrm{V} = {}^{1}/_{K^2}$ was tested and produced very low intensities and was inappropriate for the application. The details of oscillations were imperceptible and final maps were dropped. Another conversion that was tested, is $\mathrm{V} = {}^{1}/_{K}$, but the results were still worse to interpret comparing to contrast maps. Because of that we proceeded by only computing contrast maps for our analysis.

In an attempt to test the wavelength dependence of LSCI outside its typical biomedical context, we experimented with a purple 405 nm laser, operating at a shorter wavelength than the standard red source (635 nm). The goal was to evaluate whether different wavelengths might offer any advantage in imaging surface oscillations and if this technique is wavelength dependent. The resulting maps did not offer any advantage and we observed that for imaging surface vibrations the laser wavelength appears to have little influence on contrast formation.

8.5 Speaker Experiments

Following the stationary wave validation on the drum membrane, a second phase of experiments was designed to investigate whether the implemented LSCI system could be used not only for qualitative imaging of surface oscillations but also for quantitative assessment of vibrational energy input. Most LSCI systems go through a modeling phase in which the contrast range is linked to the physical quantities being measured. This experimental phase was designed to study controlled oscillations, with known attributes such as their frequency and magnitude. In order to achieve this, we employed a woofer speaker as a sample surface and configured our system to measure its motion.

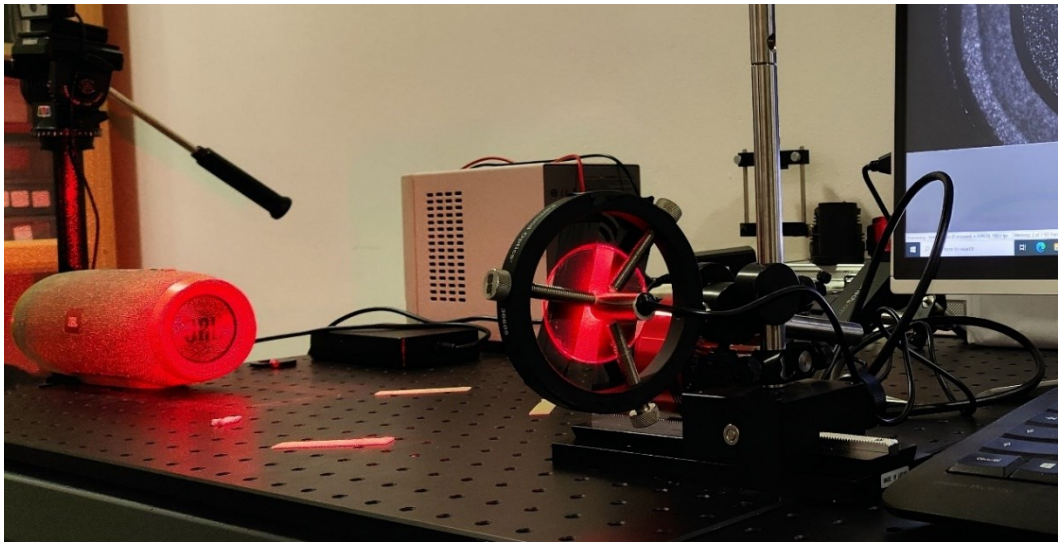

Figure 8.2: Woofer speaker LSCI setup. The images were captured by a CCD camera, illuminated by a powerful cross-polarized and diffused LASER.

8.5.1 Equipment

Figure 8.2 shows the experimental setup of the speaker tests. A cross-polarized 100mW, 635nm diode LASER illuminated the woofer's membrane. A diffuser was used to help distribute evenly the laser light across the surface, offering uniform illumination and reducing coherent noise in the speckle pattern. On top of it, a polarizer was placed to filter the light source and counter the glare, enhancing speckle contrast.

Our imaging setup consisted of the same 24-bit RGB CCD camera (ZWO ASI178MC, China) and lens (Tamron M112FM16, Japan), as well as frame grabber software (SharpCap 4.1) and computer (Windows, 32 GB of RAM).

8.5.2 Imaging Procedure

During this phase, frames were captured in a resolution equal to 1280 x 720 pixels that was sufficient to capture the entirety of the membrane in a stable frame rate of 100 fps. Additionally, we used an exposure time of 5ms. A frequency generator was used to drive the speaker with acoustic pulses at alternating frequencies to investigate the system's sensitivity to varying vibrational energy. This setup allowed precise control of the pulse frequency and amplitude, resulting in fully customized membrane oscillations for testing. The membrane was excited with square wave signals at 20 Hz and 40 Hz frequencies that are within the limits of the Nyquist sampling criterion, given the camera's frame rate. The resulting membrane motion was illuminated with the laser source, and speckle patterns were recorded using the configured camera settings for subsequent contrast analysis.

8.6 Finger Occlusion

This final phase of the experimental part had a main goal of optimizing our system for the biomedical application that is the focus of our thesis and validating LSCI on visualizing blood perfusion. The chosen occlusion – reperfusion evaluation works by applying a pressure band to a subject's finger to induce temporary occlusion, followed by its release to observe the reperfusion phase. This experiment allowed us to assess the system's sensitivity to physiological changes in blood perfusion, and to confirm its ability to capture relative variations in speckle contrast corresponding to reduced and restored flow.

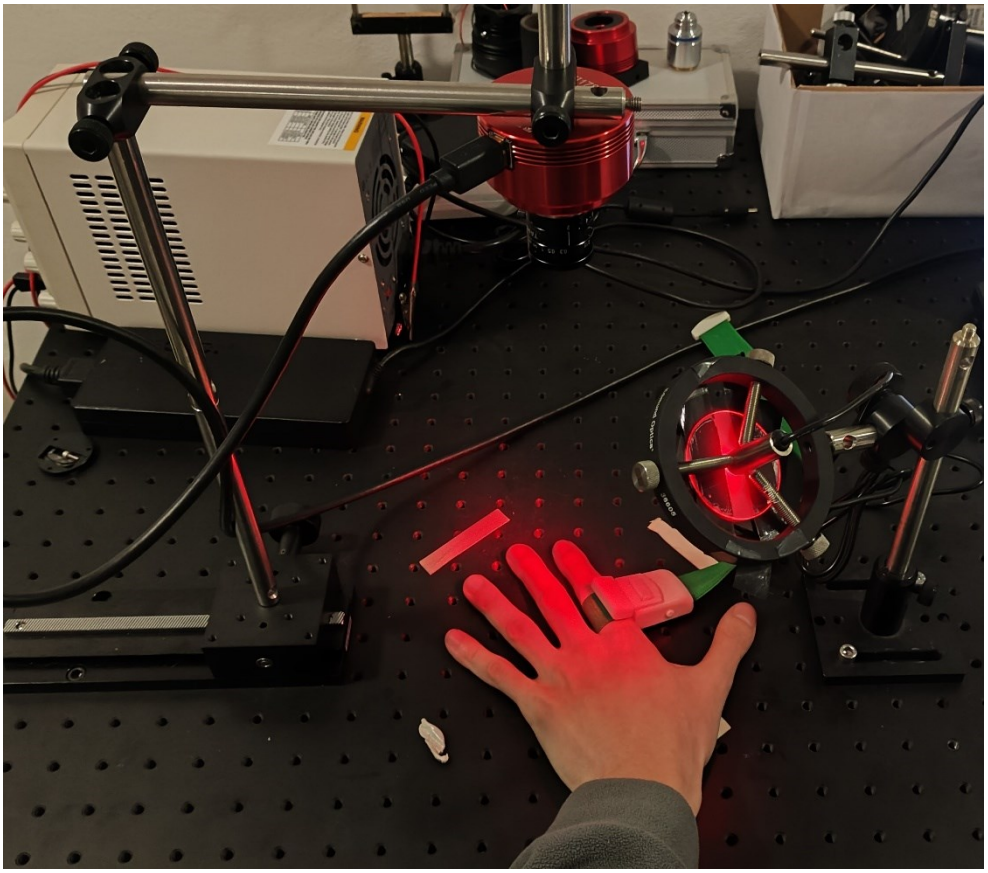

Figure 8.3: Finger Occlusion LSCI setup. The images were captured by a CCD camera, illuminated by a powerful cross-polarized and diffused LASER.

8.6.1 Equipment

Figure 8.3 shows the experimental setup of the occlusion – reperfusion tests on human hand. An occlusion tourniquet is placed on the index finger of the subject's hand.

The use of hand stabilization tools was not chosen, as it was our priority to check the operation of the method in real life scenarios, and validate the practical usability in clinical settings without the use of additional equipment.

A cross-polarized 100mW, 635nm diode LASER illuminated two of the fingers, one that undergoes occlusion and one that serves as a baseline control. A diffuser was used to help distribute evenly the laser light across the surface, offering uniform illumination and reducing coherent noise in the speckle pattern. On top of it, a polarizer was placed to filter the light source and counter the glare, enhancing speckle contrast.

Our imaging setup consisted of the same 24-bit RGB CCD camera (ZWO ASI178MC, China) and lens (Tamron M112FM16, Japan), as well as frame grabber software (SharpCap 4.1) and computer (Windows, 32 GB of RAM).

8.6.2 Imaging Procedure

During the skin perfusion experiments, videos of the index finger, undergoing occlusion were captured while the middle finger is also on the image plane in order to gain normal baseline perfusion contrast ranges. During the recording of our samples we remove the occlusion band to capture the reperfusion phase on the same video with the finger's location unchanged.

Frames were captured in a resolution equal to 1544 x 1040 pixels and a frame rate of 60 fps. In addition, we tested exposure times ranging from 5ms to 20ms, values that are widely used in the literature and are proven to provide optimal measurements.

8.6.3 Occlusion Setup Optimization

In this phase, we observed that LSCI maps can be misleading or difficult to interpret due to the way, the normalization is executed in the algorithms. In order to produce valuable results, we use global normalization which takes into account the velocity range from the whole stack of images to attribute the final intensity values. During the removal of the occlusion bands, the finger was moving unavoidably no matter the care of the band removal. The effect of this phenomenon was more than just inducing noise on these specific frames. Because of the normalization, extremely high velocities from this occasion, compressed the intensity range of perfusion velocity in the entire resulting stack of maps. The contrast values from the movement of the hand were magnitudes smaller than contrast from blood perfusion resulting in weak visual representation of the perfusion differences in occlusion – reperfusion.

A related problem, was the occlusion's band plastic mound that was highly reflective. This problem falls under the category of noise from glare that saturates the intensity pixels and results in extreme contrast values. Final maps produced contrast values exceeding those occurring from skin perfusion and produced error because of the normalization range.

To counter these phenomena, we cut out the frames of occlusion band removal as well as cropped the raw speckle images to eliminate optical noise. Another solution could be the modification of our algorithm to enforce threshold values and discharge values

well above the accepted range. Or we could modify the normalization process of the data saving routine to accommodate our needs.

In this phase of the experimental work, we also investigated the common analytical approximations for velocity existing in the literature, in comparison with the formula $V = \frac{1}{K^2}$ that we mainly used. Applying this approach, the mean velocity of a non-occluded finger ranged from .22 to 0.3 arbitrary units, using spatial contrast analysis. The same raw speckle video was processed to calculate velocity using the three most common theoretical models.

Using the classical formula widely used until 2008 and established by D. Briers and S. Webster in the development of LASCA [72] and assuming Lorentzian distribution our velocity maps produced a range of 100-200 μm/s of mean contrast in normal skin perfusion. These results are in agreement with values reported for LASCA experiments (100–250 μm/s) and, given that a spatial contrast method was also employed, they provide additional validation for our system. When we calculated velocity with $V = \frac{\lambda z}{D\tau_c}$ formula, mean velocity ranged from 2000 to 2500 μm/s which overestimates the physiological range and has a significant divergence from the previous two approaches. Similarly, the measured perfusion index, using the optical model $V = 0.41\frac{\lambda}{NA\tau_c}$ yielded mean values of 800-1200 μm/s, still above expected physiological capillary flow.

The divergence between these different estimates highlights that while theoretical models offer useful order-of-magnitude consistency results, the strong assumptions that they rely, make single-exposure LSCI non-quantitative, unless dedicated configuration is involved.

Nevertheless, it is worth mentioning, that $V = \frac{1}{K^2}$ produced visually nearly identical results with all other theoretical formulas. In some instances, frame-by-frame comparisons showed zero pixel-wise difference when subtracting the resulting maps, demonstrating that these different approximations can be all applied in qualitative imaging.

Chapter 9

Algorithmic Implementation

9.1 Implementation Strategy and Rationale

The choice of application is the key factor in deciding the algorithmic side of the system. When planning the implementation, we considered our specific needs, imaging oscillations, monitoring mechanical motion and measuring skin perfusion. As we explained earlier, LSCI is incapable of producing vascular maps for skin perfusion, regardless of the algorithm.

Most of the recent development in LSCI is focused on enhancing the visualization of vasculature, noise reduction, achieving better statistical reliability and finally producing clear vascular maps. In our case, these advanced methods aren't particularly useful. Advanced methods like anisotropic algorithms or multi-exposure imaging provide significant advantages in standard blood flow imaging, but for skin perfusion they don't make much sense because there's no clear vasculature to resolve in the first place.

Visualizing oscillations, which is our focus in the initial phases, is significantly determined by the limitations imposed by the frame rate of our system. Therefore, choosing an algorithm that provides the best temporal resolution was essential. Spatial contrast analysis is the most efficient in the temporal domain, with temporal resolution depending only on frame rate of the camera. This choice would also work well for our occlusion – reperfusion experiments that are not really affected by a reduced spatial resolution, given that our goal is to monitor velocity trends during the two phases of the experiment.

Choosing a spatial contrast, also known as LASCA (as originally named), makes the implementation rather simple and do not require complex designing features. We decided on using an open source implementation, while focusing on adapting it to our system and developing efficient post-processing algorithms, which will be described in this part of the thesis.

9.2 Open-Source Toolbox and Adaptation

To put this into practice, we based our implementation on an open-source LSCI script available on GitHub [90]. The repository by Stoyan Yordanov provides a complete framework on MATLAB for computing contrast maps using different approaches, including spatial analysis. We used this as a starting point and made several modifications to fit our system's configuration and handle the specific recording formats we employed.

This MATLAB project provides four different algorithms for contrast calculation, intending to optimize the processing time and computational demand. We used the

developer's recommended numerical method, convfilter, which is the most efficient in terms processing time. The provided `sLASCAConvFilter` function uses a sliding window over each frame to calculate the local mean and mean-square intensity, and then computes the standard deviation normalized by the mean, as the definition of contrast requires. This method is vectorized in the temporal dimension (`Z-stack`) while using the efficient MATLAB's `filter2` function for fast averaging. `filter2` function applies a convolution filter, in order to average pixel values over a sliding window.

Then, our system used a modified version of the function `lsci_sLASCA.m` that computed contrast from the stack of frames that we captured and then skipped the computation of the correlation time. Instead, we used the common approximation of velocity $V = \frac{1}{K^2}$ which relies directly only on the contrast maps. Our script `lsci_sLASCA_V_approximation` used the function `calcVelocityMap1` that is shown below and computed the velocity map as described.

```
function rtrnXYZLSPVelocity = calcVelocityMap1(LSPContrast)
% Calc 3D XYZ Velocity Map from Laser Speckle

fprintf('\nProgress Velocity (Calc): ');
startTime = tic;

% Calc velocity map from contrast map --> we approximate by:
rtrnXYZLSPVelocity = 1 ./ (LSPContrast .^2);

% Filter velocity with Inf and/or NaN values
rtrnXYZLSPVelocity(isnan(rtrnXYZLSPVelocity)) = 0;
rtrnXYZLSPVelocity(rtrnXYZLSPVelocity == Inf) = 0;

% Remove velocity outliers
% [lengthX, lengthY, lengthZ] = size(rtrnXYZLSPVelocity);
% for iZ = 1:lengthZ
%     subFrame = rtrnXYZLSPVelocity(:, :, iZ); % get current frame
%     vthreshold = 4*median(subFrame, 'all'); % calc oultlier's upper boundary using the median
%     subFrame(subFrame > vthreshold) = vthreshold;
%     rtrnXYZLSPVelocity(1:end, 1:end, iZ) = subFrame;
% end

% Show progress
elapsedTime = toc(startTime);
fprintf('100%% | %.3f [sec]\n', elapsedTime);
end
```

Figure 9.1: Modified velocity map computation

It is worth mentioning, that throughout the experimental analysis we also used the original script of this repository, as well as other modified versions of the above function to compute and compare different approaches of velocity calculation. This is described in detail (including the approximations we used) in the results of our skin perfusion experiments.

We chose .tiff files as our format of choice to save the computed maps. Our analysis required global normalization to produce maps, useful and reliable. We detected a bug in the standard normalization process that resulted in local normalization even when global normalization was selected. This was an error, occurring because of tiff lib from MATLAB. For this reason, we used another variant of the normalization process that is shown below.

```
%Variant 2 --> uses custom tiff lib
objFastTiffWiter = TiffWriterClass(fileNameAndPath, 37.8, 0); % object to tiff file
for iZ = 1:size(OutputXYZFrames, 3)

    frameLSP = OutputXYZFrames(:, :, iZ)./maxIt(iZ); % normalize to 1
    % cInt = 2^16 - 1;
    cInt = 255; % coefficient to convert to 8 or 16 bit integer
    frameLSP = uint8(cInt.*frameLSP); % convert to 8 or 16 bit depth

    objFastTiffWiter.WriteImage(frameLSP); % save Laser Speckle 3D stack
end
objFastTiffWiter.close; % close tiff file
```

Figure 9.2: Global normalization variant, used during our data processing.

In this variant, each local contrast map is normalized by a global maximum, that was previously calculated as `maxIt(1:end) = max(OutputXYZFrames(:));`

This keeps the dynamic range consistent frame-to-frame and avoids artificial brightness jumps caused by local maxima. Finally, the normalized maps are scaled to 8-bit integer format for proper storage.

A key software decision of our system, which created several challenges, needed to resolve during the experiments involved the camera output format and frame grabbing. While RGB acquisition provides more intensity information, it increases processing time and memory usage. On the other hand, grayscale acquisition is sufficient for contrast computation and yields better performance in real-time capture. After testing both options, we selected grayscale acquisition as the most efficient and reliable format for our setup for several reasons. First, the frame grabber performed better using the grayscale format, which uses a single channel instead of three, resulting in less data per frame, lower computational load, and higher frame rates. From a software perspective, grayscale was ideal because no further color conversion was required and the resulting arrays were ready for image processing and contrast calculation. In contrast, Rgb24 formats consist of three channels and are essentially 3 times larger in data size, while the color information itself is not useful, given that the system uses a monochromatic 635 nm red laser source. However, due to the noise induced from environmental light in our original sample videos, we finally decided to use Rgb24 format. During processing, the green and blue channels were dropped, keeping only the red channel to from the arrays for contrast computation. This was made to ensure that wavelengths unrelated to the illumination were removed from the images, effectively also removing unwanted noise from the processed speckle maps.

```
% Convert to matrix
switch(videoObj.VideoFormat)
    case {'RGB24', 'RGB24 Signed', 'RGB48', 'RGB48 Signed'} % three color channels video

        % Case of color video -->  XxYxChxZ, Ch = 3 - we reduce it to single channel video
        rtrnMatrix = permute(rtrnMatrix, [1, 2, 4, 3]); % we take only the third color channel as a gray scale value
        rtrnMatrix = rtrnMatrix(:, :, :, 1); % reduce dimensions to 3
```

Figure 9.3: RGB manipulation, discarding the green and blue channels.

9.3 Post-Processing

Additional post-processing routines were also developed to visualize contrast and velocity trends as well as calculate metrics to evaluate the performance of the system. All of these steps are described in detail in the following part of this section.

Several custom functions were implemented, all built on the same core principle, the use of Regions of Interest (ROIs). Defining ROIs was a fundamental part of every post-processing step, which ensured that contrast and velocity statistics were computed meaningfully for each experiment.

The most important function of the post-processing phase is computeMeanIntensityOfROI that calculates the mean intensity of a ROI in a specific frame of a .tiff file (format of contrast map). This function can calculate both mean contrast and mean velocity and became the backbone of our post-processing analysis.

```
function meanIntensity = computeMeanIntensityOfROI(videoFile, windowPosition, windowSize, frame)
% computeMeanIntensityOfROI
% Computes the mean intensity (contrast) of a rectangular ROI in a specific frame of a TIFF stack.
%
% Parameters:
%   videoFile       - Path to the multipage TIFF file containing contrast maps
%   windowPosition  - [x, y] coordinates of the top-left corner of the window
%   windowSize      - [width, height] of the window
%   frame           - Frame number of the stack (1-based index)
%
% Returns:
%   meanIntensity   - The mean contrast value within the specified ROI

    % Read the specified frame
    imageFrame = imread(videoFile, frame);

    % Define ROI bounds
    x = windowPosition(1);
    y = windowPosition(2);
    w = windowSize(1);
    h = windowSize(2);

    % Extract ROI
    roi = imageFrame(y : y + h - 1, x : x + w - 1);

    % Compute mean intensity
    meanIntensity = mean(roi(:));
end
```

Figure 9.4: `ComputeMeanIntensityOfRoi`

Computation of a ROI's mean intensity in a particular frame

Following the development of this function, it was used in the implementation of *`computeMeanIntensityOfRoi`* function that computed the mean intensity of a specific ROI across the frames of a whole stack. This feature was used in all parts of our experimental phase, with the exception of the stationary oscillation analysis.

```m
function meanOfMeans = computeMeanIntensityOfROIStack(videoFile, windowPosition, windowSize, startFrame, endFrame)
% computeMeanIntensityOfROIStack
% Computes the mean intensity for a given ROI across multiple frames in a TIFF stack.
%
% Parameters:
%   videoFile       - Path to the multipage TIFF file
%   windowPosition  - [x, y] top-left corner of the ROI
%   windowSize      - [width, height] of the ROI
%   startFrame      - First frame index (inclusive)
%   endFrame        - Last frame index (inclusive)
%
% Returns:
%   meanIntensities - Vector of mean intensity values for each frame

    numFrames = endFrame - startFrame + 1;
    meanIntensities = zeros(1, numFrames);

    for i = 1:numFrames
        frameIdx = startFrame + i - 1;
        meanIntensities(i) = computeMeanIntensityOfROI(videoFile, windowPosition, windowSize, frameIdx);
    end

    % Compute the mean of the means
    meanOfMeans = mean(meanIntensities);
end
```

Figure 9.5: `ComputeMeanIntensityOfRoiStack`

Computation of a ROI's mean intensity in the whole stack of frames

For monitoring stationary oscillations, we calculated the mean intensity of the selected ROIs in each frame individually using `computeMeanIntensityOfRoi`. This was necessary due to the nature of the phenomenon that we were monitoring. The values were then stored into a vector, in order for the trends of all the static and dynamic ROIs to be plotted together in a single graph. The physical principles underlying this analysis are described in detail later in the experimental section.

```m
function plotContrastROITrends(staticValues, dynamicValues)
% plotContrastROITrends
% Plots the average mean contrast values for static and dynamic ROIs across frames.
%
% Parameters:
%   staticValues  - Nx2 matrix where each row contains the two static ROI values for one frame
%   dynamicValues - Nx2 matrix where each row contains the two dynamic ROI values for one frame

    % Compute mean per frame
    staticMean = mean(staticValues, 2);
    dynamicMean = mean(dynamicValues, 2);

    % Number of frames
    numFrames = size(staticValues, 1);
    frames = 1:numFrames;

    % Plotting
    figure;
    plot(frames, staticMean, '-o', 'LineWidth', 1.5, 'DisplayName', 'Static ROIs');
    hold on;
    plot(frames, dynamicMean, '-o', 'LineWidth', 1.5, 'DisplayName', 'Dynamic ROIs');
    xlabel('Frame');
    ylabel('Mean Contrast');
    title('Contrast Trends of Static and Dynamic ROIs');
    legend('Location', 'best');
    grid on;
end
```

Figure 9.6: `plotContrastROITrends`

Plots contrast trends of static and dynamic sets of ROIs

For all other parts of our experiments, we computed the mean intensity of a consistent ROI across each frame of the stack. We developed the function

`plotMeanIntensityToFrame` to calculate and plot the mean intensity of the selected ROI in relation to the frame number.

```
function [figHandle, axHandle] = plotMeanIntensityToFrame(videoFile, windowPosition, windowSize, startFrame, endFrame)
    % Plots the mean intensity within a specified window across the frames of a TIFF file
    %
    %
    % Parameters:
    % videoFile - Path to the multipage TIFF file containing contrast maps
    % windowPosition - [x, y] coordinates of the top-left corner of the window
    % windowSize - [width, height] of the window
    % startFrame - Starting frame number (inclusive)
    % endFrame - Ending frame number (inclusive)

    % Parameters check
    if nargin < 5
        error('All parameters (videoFile, windowPosition, windowSize, startFrame, endFrame) must be provided.');
    end

    % Load TIFF information to get the number of frames
    info = imfinfo(videoFile);
    totalFrames = numel(info);

    % Ensure the start and end frames are within valid range
    if startFrame < 1 || endFrame > totalFrames || startFrame > endFrame
        error('Invalid frame range. Ensure 1 <= startFrame <= endFrame <= totalFrames.');
    end

    % Calculate the number of frames to process
    numFrames = endFrame - startFrame + 1;

    % Pre-allocate needed size array
    meanIntensities = zeros(1, numFrames);


    % Loop through the stack and use the mean of ROI function
    for i = 1:numFrames
        frameIdx = startFrame + i - 1;
        meanIntensities(i) = computeMeanIntensityOfROI(videoFile, windowPosition, windowSize, frameIdx);
    end

    % Create a new figure and plot
    figHandle = figure;
    axHandle = axes(figHandle);
    plot(axHandle, startFrame:endFrame, meanIntensities, '-o');
    xlabel(axHandle, 'Frame Number');
    ylabel(axHandle, 'Mean Intensity in Window');
    title(axHandle, 'Mean Intensity to Frame Number');
end
```

Figure 9.7: `plotMeanIntensityToFrame`

Plots the mean intensity of a ROI as a function of frames

We then implemented a function similar to `ComputeMeanIntensityOfRoiStack`, but to compute the standard deviation of the region instead. This was essential for our last part of post processing that is a common metric, known as CNR used to assess LSCI techniques.

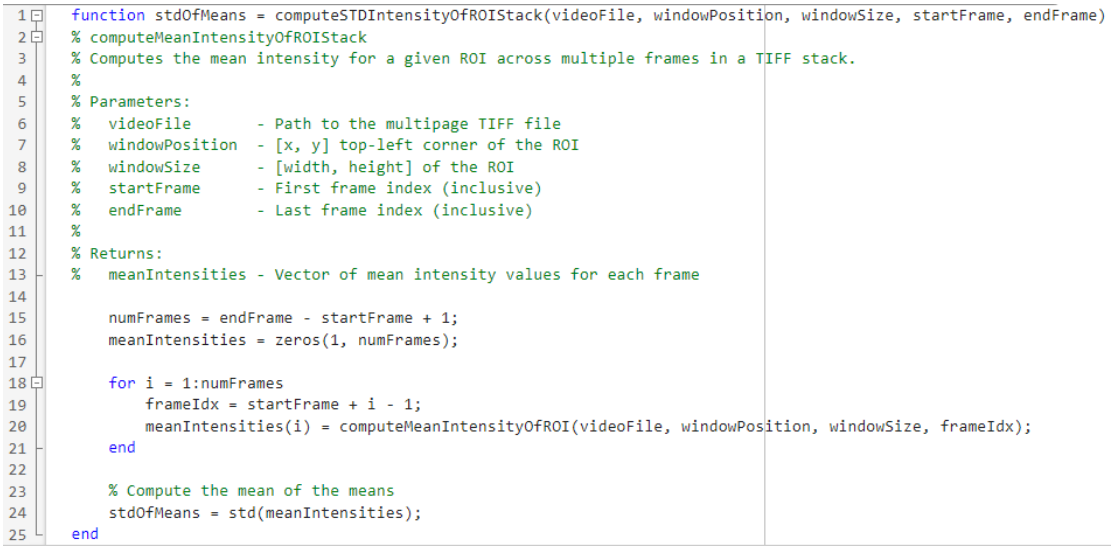

```
function stdOfMeans = computeSTDIntensityOfROIStack(videoFile, windowPosition, windowSize, startFrame, endFrame)
% computeMeanIntensityOfROIStack
% Computes the mean intensity for a given ROI across multiple frames in a TIFF stack.
%
% Parameters:
%   videoFile       - Path to the multipage TIFF file
%   windowPosition  - [x, y] top-left corner of the ROI
%   windowSize      - [width, height] of the ROI
%   startFrame      - First frame index (inclusive)
%   endFrame        - Last frame index (inclusive)
%
% Returns:
%   meanIntensities - Vector of mean intensity values for each frame

    numFrames = endFrame - startFrame + 1;
    meanIntensities = zeros(1, numFrames);

    for i = 1:numFrames
        frameIdx = startFrame + i - 1;
        meanIntensities(i) = computeMeanIntensityOfROI(videoFile, windowPosition, windowSize, frameIdx);
    end

    % Compute the mean of the means
    stdOfMeans = std(meanIntensities);
end
```

Figure 9.8: `ComputeMeanIntensityOfRoiStack`
Computation of a ROI's standard deviation in the whole stack of frames

The contrast-to-noise (CNR) ratio is defined as the absolute difference between the mean intensities of two ROIs divided by the standard deviation of the static region. The standard deviation of that region is related to noise (as explained in the following section).

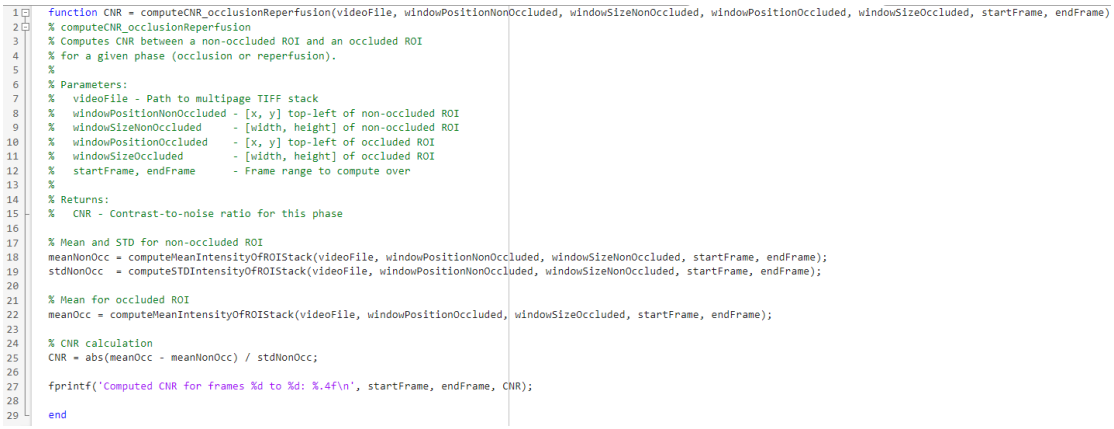

```
function CNR = computeCNR_occlusionReperfusion(videoFile, windowPositionNonOccluded, windowSizeNonOccluded, windowPositionOccluded, windowSizeOccluded, startFrame, endFrame)
% computeCNR_occlusionReperfusion
% Computes CNR between a non-occluded ROI and an occluded ROI
% for a given phase (occlusion or reperfusion).
%
% Parameters:
%   videoFile - Path to multipage TIFF stack
%   windowPositionNonOccluded - [x, y] top-left of non-occluded ROI
%   windowSizeNonOccluded     - [width, height] of non-occluded ROI
%   windowPositionOccluded    - [x, y] top-left of occluded ROI
%   windowSizeOccluded        - [width, height] of occluded ROI
%   startFrame, endFrame      - Frame range to compute over
%
% Returns:
%   CNR - Contrast-to-noise ratio for this phase

% Mean and STD for non-occluded ROI
meanNonOcc = computeMeanIntensityOfROIStack(videoFile, windowPositionNonOccluded, windowSizeNonOccluded, startFrame, endFrame);
stdNonOcc  = computeSTDIntensityOfROIStack(videoFile, windowPositionNonOccluded, windowSizeNonOccluded, startFrame, endFrame);

% Mean for occluded ROI
meanOcc = computeMeanIntensityOfROIStack(videoFile, windowPositionOccluded, windowSizeOccluded, startFrame, endFrame);

% CNR calculation
CNR = abs(meanOcc - meanNonOcc) / stdNonOcc;

fprintf('Computed CNR for frames %d to %d: %.4f\n', startFrame, endFrame, CNR);

end
```

Figure 9.9: `computeCNR_occlusionReperfusion`
computes CNR between to ROIs, as previously defined

Finally, we include an indicative script that enabled us to plot the results of `plotMeanIntensityToFrame` function in a single graph which was significant for the visual interpretation and presentation of our results.

```
>>
% === Compute mean intensity for each ROI ===
% Occluded ROI
[fig_dyn, ax_dyn] = plotMeanIntensityToFrame(
'...\600frames_5ms_finger_occlusion_60fps_cross_polar_diffus_mono8_sLSC-v.tif', [490,120], [950,320], 1, 132);

% Non-Occluded ROI
[fig_stat, ax_stat] = plotMeanIntensityToFrame(
'...\600frames_5ms_finger_occlusion_60fps_cross_polar_diffus_mono8_sLSC-v.tif', [330,620], [725,300], 1, 132);

% === Extract data from the plots ===
% Occluded
figure(fig_dyn);
ax_dyn = gca;
x_dyn = get(ax_dyn.Children, 'XData');
y_dyn = get(ax_dyn.Children, 'YData');

% Static
figure(fig_stat);
ax_stat = gca;
x_stat = get(ax_stat.Children, 'XData');
y_stat = get(ax_stat.Children, 'YData');

% === Combine and plot both ROIs together ===
figure;
plot(x_dyn, y_dyn, '-o', 'DisplayName', 'Occluded ROI');
hold on;
plot(x_stat, y_stat, '-x', 'DisplayName', 'Non-Occluded ROI');
xlabel('Frame Number');
ylabel('Mean Intensity');
title('Mean Intensity of Occluded and Non-Occluded ROIs');
legend('show');
grid on;
```

Figure 9.10: Plotting together mean velocities from ROIs in perfusion-reperfusion experiments.

Chapter 10

Results

10.1 Drum Experiments

The resulting maps with 1ms exposure time, achieved best visualizing patterns of variating velocities during oscillations. One particular recording was selected as the most representative and visually clear example of the resulting contrast maps, balancing detail and presentation convenience. The raw speckle video was captured in 1920 x 1080 pixels with a stable frame rate of 56fps. Although an alternative video with higher resolution produced equally satisfactory maps, its larger size was less practical for side-by-side visualization in small-size windows.

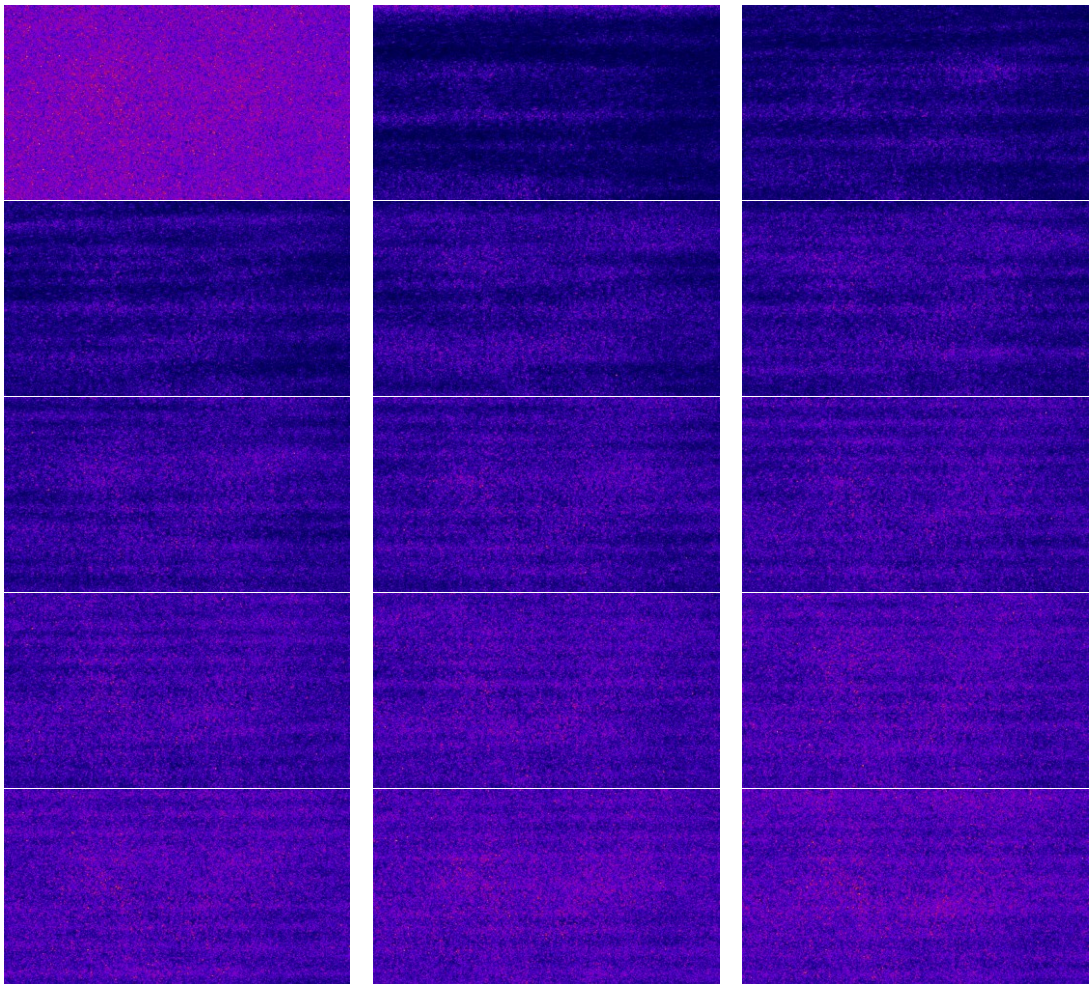

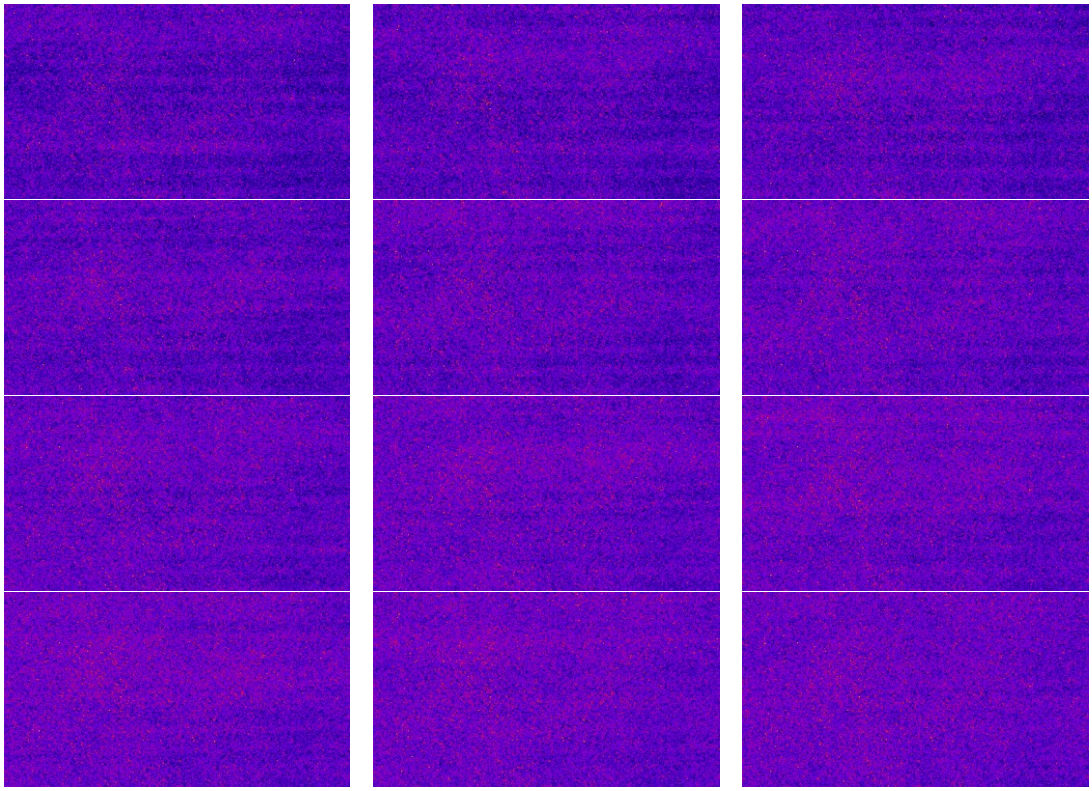

Figure 10.1: Frames-Contrast maps of oscillations

A sequence of 27 contrast maps was acquired to capture the full progression of the drum membrane oscillations, from the initial disturbance until the contrast values return to baseline, indicating full attenuation of motion. A look up table was applied in the contrast maps to enhance visualization and optical detection of patterns.

Nodal and anti-nodal regions are apparent from the first frame that oscillations have propagated to the whole drum's surface (1st row, 2nd column image in Figure 10.). As the oscillation evolves visible from approximately the seventh frame (3rd row, 1st column), stationary field patterns mostly consist of stationary and moving lines, which gradually fade as the phenomenon decays and the membrane returns to its static state. No fixed dynamic or static areas were observed across frames due to the nature of the standing wave pattern. These results highlight LSCI's sensitivity to motion-related contrast variation on a per-frame basis.

To further assess the local contrast behavior, quantitatively, we continue with a Region of interest (ROI) analysis in a selected sequence of contrast maps that capture the initial stages of the membrane's response after disturbance. In each frame, two static and two dynamic ROIs were manually selected in areas exhibiting higher contrast values (indicating minimal motion), and lower contrast (indicating surface displacement) respectively. These ROIs were selected independently for each frame, as was already indicated by previous results that the distribution of static and dynamic regions varies due to the wave-like propagation of motion across the membrane. The mean contrast values within the ROIs were computed to analyze the spatial variability in motion captured by LSCI.

The following contrast maps are a result of an RGB24 recording captured with our final experimental configuration. They visualize the membrane oscillations resulting from a

mild disturbance with the drumstick and shows the quick attenuation of the phenomena which makes it straightforward to interpret visually and analyze.

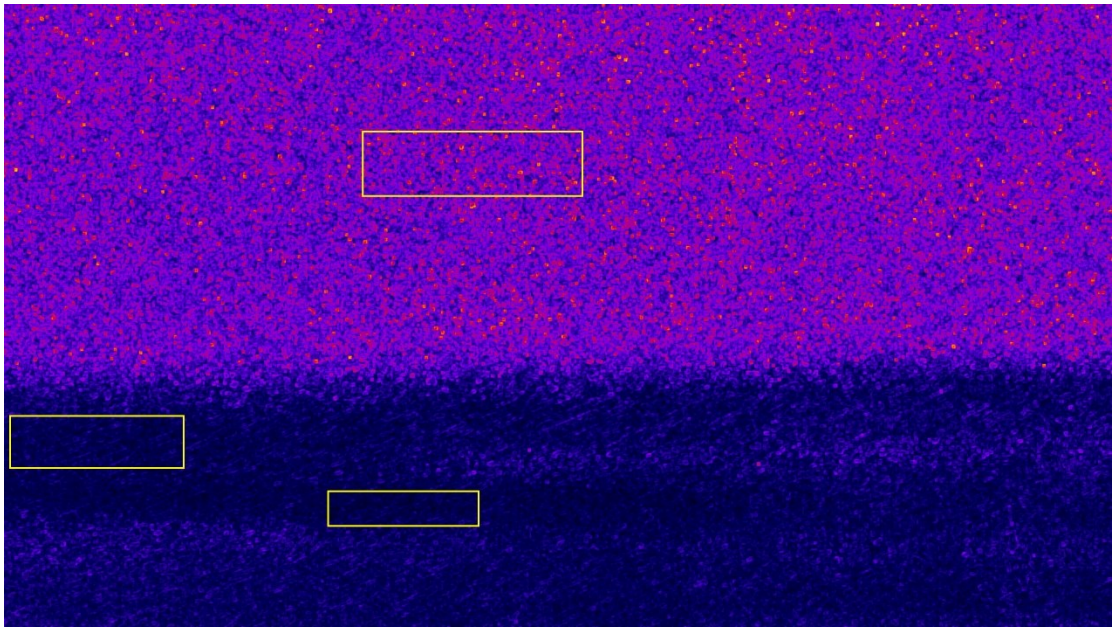

Figure 10.2: Initial Frame of the disturbance's propagation

An interesting achievement of this LSCI contrast map is capturing the transmission of the wave through the drum's surface. The contrast values on the top of the frame are similar with the previous frame that was completely static, while the lower part has low contrast values that visualize the moving membrane. The drum was hit under our field of view, so this LSCI image is effectively capturing the wave moving from the bottom to the top, proving that the frame rate is sufficient to visualize, at least, first order oscillations. On the other hand, the progression of the vibration caused by the stick is captured barely, in just one frame, signifying that the system would benefit from increased frame rate.

As representative dynamic regions we selected dynamic ROI 1, that extends from point [560,840] with an area equal to [260 x 60] (width x height) and has a mean contrast value equal to 11.9761, and dynamic ROI 2, which extends from point [10,710] with an area equal to [300 x 90] (width x height) and has a mean contrast value equal to 13.8610. For static regions, we selected static ROI 1, that extends from point [620,220] with an area equal to [380 x 110] (width x height) and has a mean contrast value equal to 57.4928.

In order to proceed in this analysis, we analyzed the sequence of static frames that were captured before the drum stroke that provide baseline contrast values without the presence of motion and are also indicative of the contrast distribution with no external stimulation. After observing the histogram of the sequence, we had a clear view of static contrast ranges that could further aid our analysis.

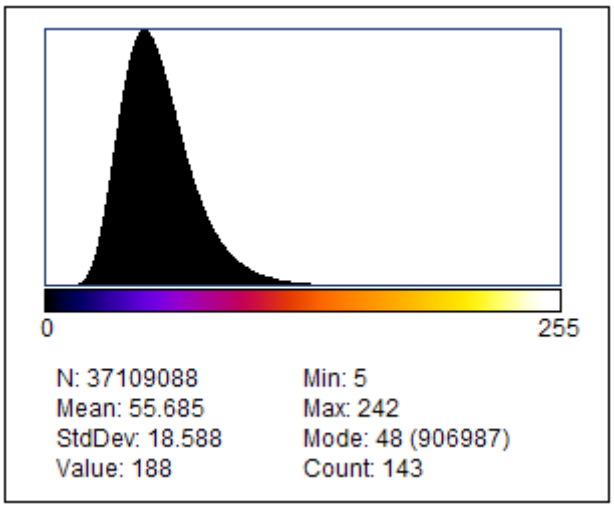

Figure 10.3: Histogram of the static sequence of contrast maps, bell-shaped, Gaussian-like.

Combined with the contrast maps and the selected ROIs, we also present a grayscale version of the image with a threshold to highlight the areas remaining static after the beginning of oscillations. To visualize areas with minimal motion, a global threshold T was empirically selected, according to the form of the curve that is bell-shaped with Gaussian-like distribution:

$$T = \mu - 0.5\sigma = 55.941 - 0.5 \times 18.663 \cong 47$$

where μ is the mean contrast and σ is the standard deviation of the pixel intensities.

This choice ensures that regions with contrast above the threshold correspond predominantly to static or less dynamic parts of the membrane.

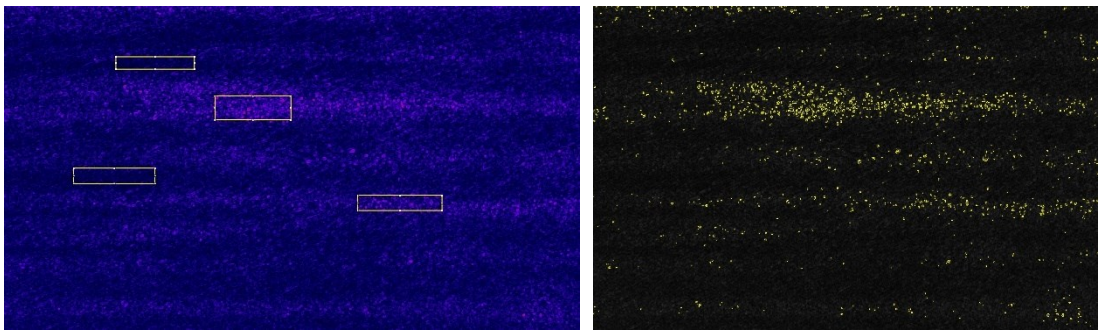

Figure 10.4: Dynamic ROI 1 extends from point [370,170] with dimensions [260 x 40] and has a mean contrast value of 13.9512, and dynamic ROI 2 that extends from point [230,540] with dimensions [270 x 50] and a mean contrast value equal to 14.2712.
Static ROI 1 starts from point [1174,630] with dimensions [280 x 50] and has a mean contrast value of 25.2227, and static ROI 2, that extends from point [700,300] with dimensions [250 x 80] and has a mean contrast value equal to 30.3365.

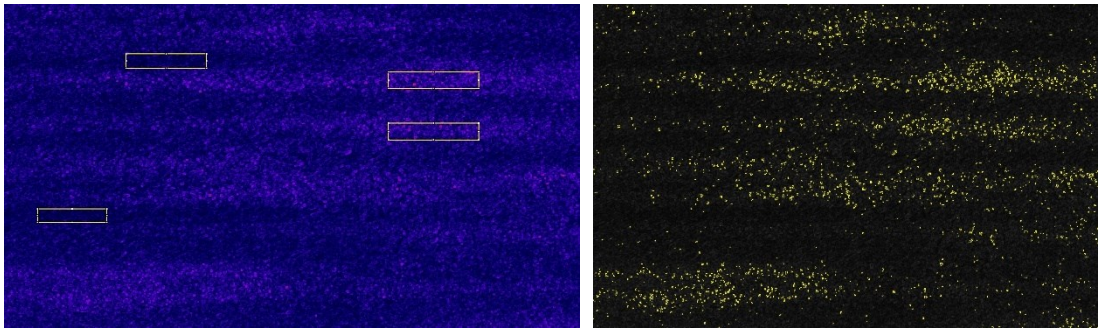

Figure 10.5: Dynamic ROI 1 extends from point [110,680] with dimensions [230 x 45] and has a mean contrast value of 14.3522, and dynamic ROI 2 that extends from point [405,165] with dimensions [200 x 45] and a mean contrast value equal to 15.3121.
Static ROI 1 starts from point [1270,225] with dimensions [300 x 55] and has a mean contrast value of 30.4596, and static ROI 2, that extends from point [1275,395] with dimensions [300 x 55] and has a mean contrast value equal to 27.2257.

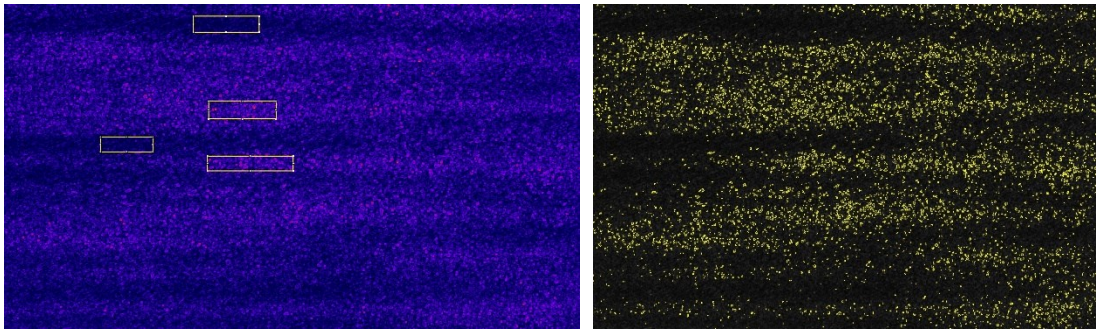

Figure 10.6: Dynamic ROI 1 extends from point [320,435] with dimensions [180 x 80] and has a mean contrast value of 18.4194, and dynamic ROI 2 that extends from point [630,40] with dimensions [220 x 55] and a mean contrast value equal to 16.6034.
Static ROI 1 starts from point [680,320] with dimensions [225 x 60] and has a mean contrast value of 33.6463, and static ROI 2, that extends from point [675,500] with dimensions [285 x 50] and has a mean contrast value equal to 32.4187.

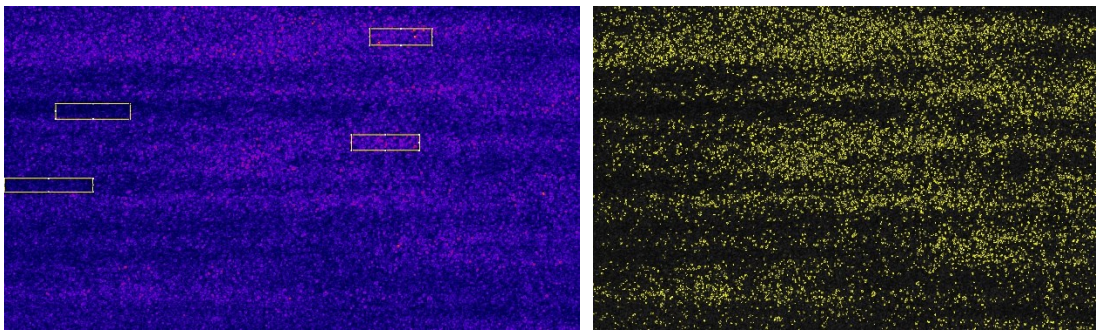

Figure 10.7: Dynamic ROI 1 extends from point [170,325] with dimensions [225 x 45] and has a mean contrast value of 17.7897, and dynamic ROI 2 that extends from point [1,570] with dimensions [295 x 45] and a mean contrast value equal to 19.5534.
Static ROI 1 starts from point [1215,75] with dimensions [205 x 55] and has a mean contrast

value of 39.0008, and static ROI 2, that extends from point [1150,425] with dimensions [225 x 50] and has a mean contrast value equal to 38.8083.

Oscillations continue with stationary wave patterns being apparent for at least another five more frames in this video. However, the series of the first five contrast maps we selected are sufficient to extract contrast trends in ROIs, representative of the static and dynamic regions and extract meaningful conclusions. Below we extract some graphs to help visualize the information of this ROI analysis.

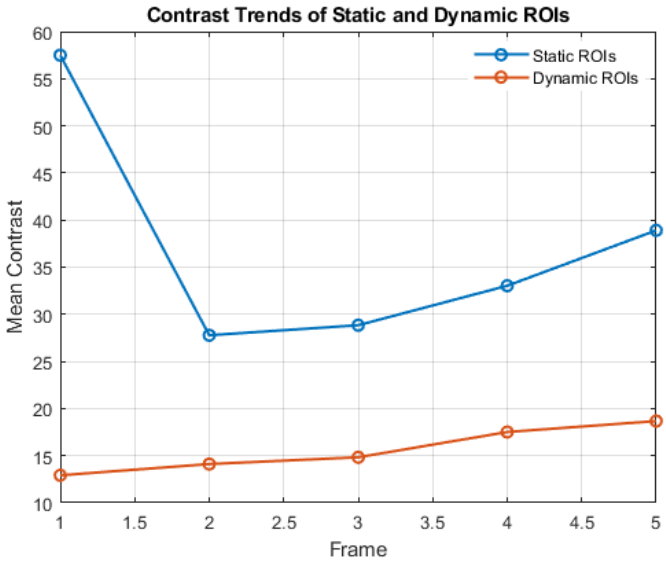

Figure 10.8: Average mean contrast to frame of the 4 selected ROIs during oscillations. Mean values were averaged to produce a single static and a single dynamic contrast value per frame.

The plot illustrates the contrast separation between static and dynamic regions at each stage of the oscillation, highlighting how dynamic regions progressively return to a static state as the phenomenon decays. Static regions consistently displayed higher contrast, while dynamic regions exhibited lower contrast in accordance with surface motion. Both static and dynamic regions display a trend of their mean contrast value increasing frame by frame, even with similar gradient.

The maximum intensity of these frames, that include pre and post oscillation values contain a maximum intensity equal to 57.4928 and a minimum equal to 12.9185. This gives an intensity range is spanning a distance of $57.4928 - 12.9185 = 44.5743$ intensity values.

This intensity span is used to calculate the normalized difference of the mean intensities in our regions of interest, nodal and anti-nodal. In each frame, we will analyze the maximum differences of intensity that appear in a comparison of dynamic and static ROIs.

The second frame (Figure 10.) displays the lowest intensity recorded in both dynamic and static regions. The two values have a difference of $\frac{27.7796-14.1112}{44.5743} = \frac{13.6684}{44.5743} = 30.66\%$ between them.

The third frame (Figure 10.) exhibits a difference of $\frac{28.8426-14.83}{44.5743} = \frac{14.0126}{44.5743} = 31.44\%$.

The fourth frame (Figure 10.) exhibits a difference of $\frac{33.0325-16.55}{44.5743} = \frac{16.4825}{44.5743} = 36.44\%$.

In the last frame (Figure 10.), the difference between average static dynamic ROIs is most apparent. The normalized difference of the mean intensity of those regions is $\frac{38.9046-18.6715}{47.0403} = \frac{20.2331}{47.0403} = 43.01\%$.

An important observation from the graph (Figure 10.) and the above analysis is that nodal areas do not assume the intensity values of post oscillation static frames. On frame 2, stationary patterns start to be observable, but static ROIs have approximately half the intensity of completely static frames, 27.7796. As the phenomenon proceeds though, contrast progressively increase. We observe that static nodal regions tend towards the contrast value of the completely static membrane faster than dynamic regions, resulting in more apparent nodal and anti-nodal regions as the phenomenon progresses.

One would assume, that nodal areas in a vibrating membrane should be completely static, but LSCI analysis shows that this is not the case. A potential explanation could be noise and frame rate lower than the necessary to fully visualize oscillations. We have indications that 56 fps are enough to capture first order oscillations on the drum, both from theory and in practice from capturing the wave's progression midway through the membrane. However, more complex vibration modes that produce higher-frequency stationary waves may exceed the system's Nyquist limit, leading to an under-resolved representation of motion and partial averaging of velocity patterns between frames. This could cause motion reduction, instead of stationarity. Moreover, higher harmonics could result in areas with low but not entirely zero motion. Real stationary waves on a drum may not form perfectly static nodes due to complex boundary conditions, membrane imperfections, or dampening effects.

The drum membrane experiment confirms the applicability of LSCI for visualizing stationary oscillations on an elastic surface under gentle to moderate excitation. The technique successfully distinguishes nodal and anti-nodal distributions in the contrast maps and tracks the progressive attenuation of surface motion, while no additional optical process is required. The clear separation between static and dynamic mean contrast values validates the system's sensitivity to subtle differences in local motion. At the same time, nodal regions depicted with motion, combined with the lack of higher-order oscillation modes underscore the limitations imposed by the frame rate of our camera.

Furthermore, comparison with related speckle metrology application, such as this article that uses speckle interferometry applied to cymbal membranes [91] indicates that higher-order modes with frequencies exceeding 2 kHz can be resolved when the system is designed to target specific resonant frequencies under controlled excitation. In that study, the cymbal was shown to oscillate with vibrational modes

exceeding 2,400 Hz. In comparison, using our configuration we could detect oscillation frequencies well below 50 Hz. While our LSCI configuration is well suited to visualize low-frequency oscillation in real time, capturing the full dynamics of the membrane's movement, comparable to those measured in the relative study we would significant increase in the camera's frame rate to satisfy the Nyquist criterion and to avoid motion averaging during exposure.

In summary, this experimental part demonstrates LSCI ability to visualize stationary field patterns in vibrating membranes. Our observations suggest that with high-speed cameras. operating at several thousand frames per second, LSCI could feasibly be extended to resolve complex, high-frequency stationary wave patterns. This suggests the system's potential for future work, expanding its use in non-contact vibration analysis.

10.1.1 Optimization Appendix

After presenting the final results on stationary wave fields, we include in this appendix a set of contrast maps derived during the optimization phase, as discussed in the previous sections.

To validate the optimizations on noise from environmental light, we present a series of consecutive frames that flickering effects are apparent, as horizontal lines with alternating height in each frame and their source is hypothetically from the main lights of the lab.

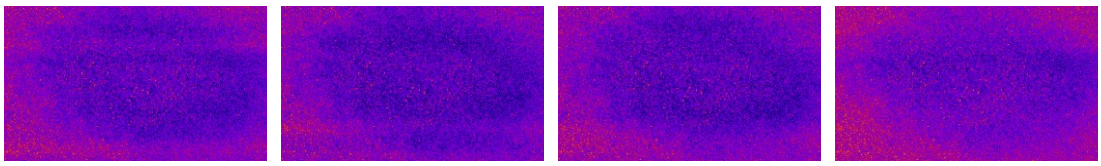

Figure 10.9: Contrast maps of four consecutive static frames captured at 1ms exposure time

We then present here, a comparison between contrast maps generated from Mono8 and RGB24 video formats, the first before eliminating ambient light and the latter afterwards. Contrast maps were acquired with a completely static membrane and external motion and vibrations absent. The results clearly highlight the presence of ambient light artifacts in the Mono8-derived maps, such as drum outlines and membrane features, which were eliminated by switching to RGB24 and isolating the red channel.

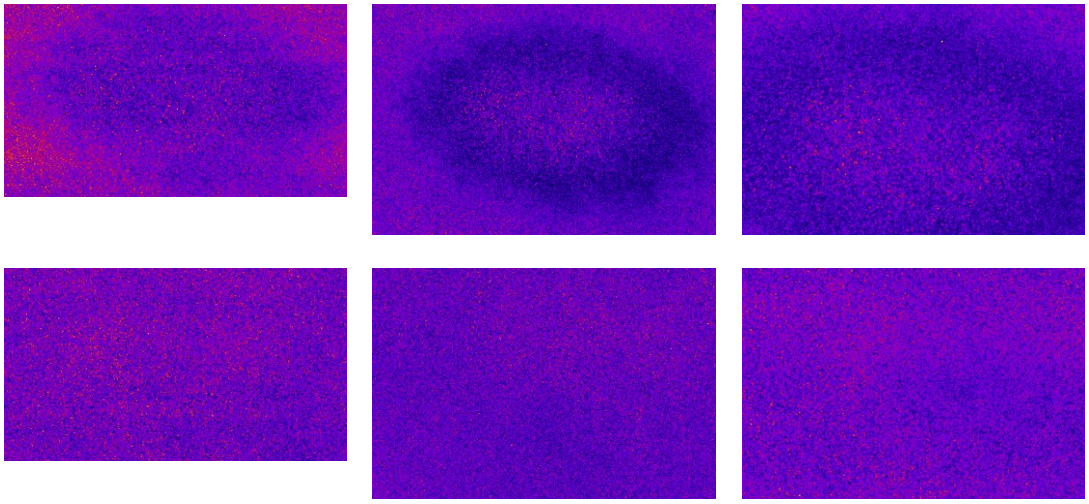

Figure 10.10: Three Mono8 contrast maps using 1ms, 5ms and 10ms exposure time respectively (First Raw). Three Rgb24 contrast maps using the same exposure times, having eliminated environmental light (Second raw).
Identical image plane of the drum setup and identical resolutions for each exposure time.

It is obvious that the second raw of results that were computed using the red channel of Rgb24 samples from the drum, having external light noise absent are uniform and no shapes or artifacts are apparent in the contrast maps.

At this point, it is meaningful to include the impact of exposure time on stationary field visualization using LSCI. The following contrast maps were computed from recordings acquired at 5 ms at the same frame rate, our system performed the best (56fps). These examples show that, using 5ms or longer exposure durations, temporal fluctuations are averaged out and the maps do not reveal any clear stationary wave patterns. Results from videos with longer exposure times are not included as they perform worse.

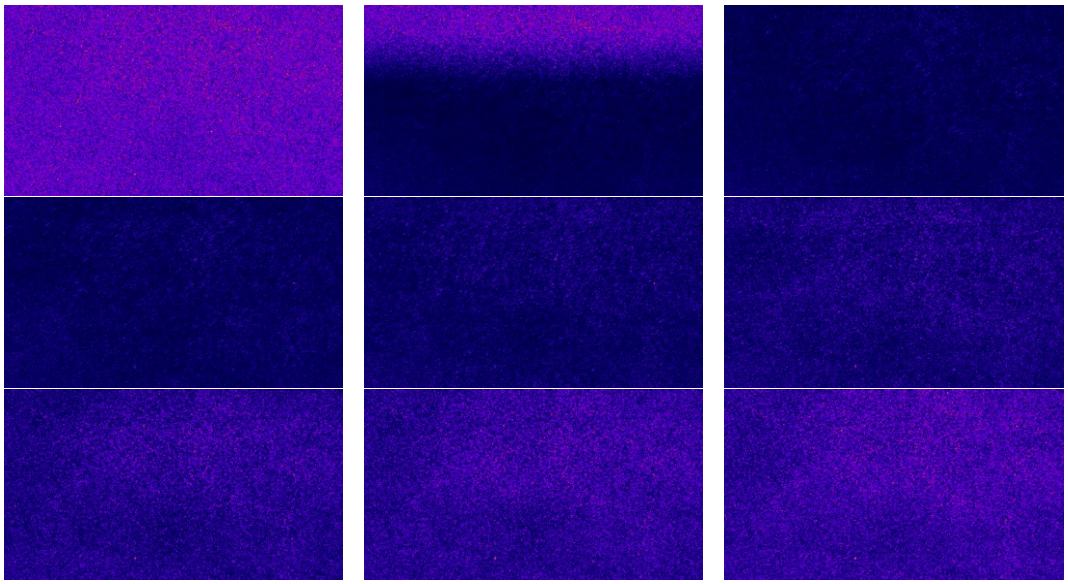

Figure 10.11: Contrast maps using 5ms exposure time

10.2 Speaker Experiments

The contrast maps using 20hz square waves resulted in clear visualization of different volume levels. We present 4 contrast maps of different amplitudes that correspond in 4 different input volume levels and are visually distinguishable by the naked eye.

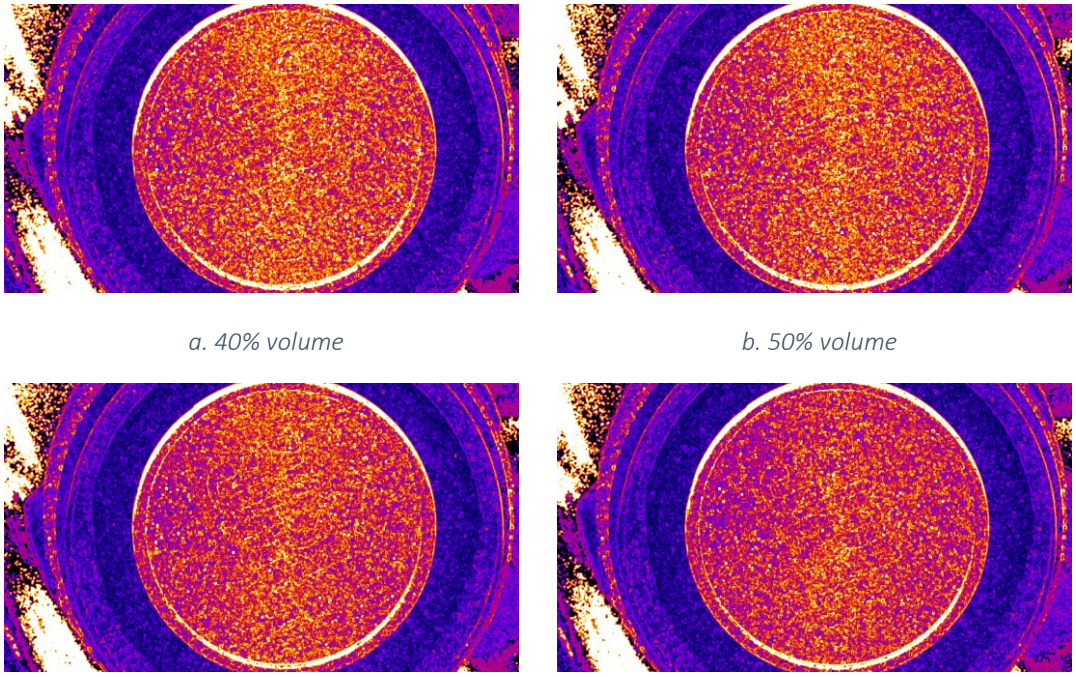

a. 40% volume

b. 50% volume

c. 60% volume

d. 70% volume

Figure 10.12: 4 Contrast maps corresponding to 4 different input volumes.

The 4 contrast maps illustrate a steady reduction of contrast as the volume increases. Considering the inverse relationship between speckle contrast and surface motion, this indicates exactly the expected behavior that greater membrane vibration is induced at higher input levels. This demonstrates that LSCI is sensitive enough to produce visually clear differences in subdivisions of volume.

In our research to link the speaker's magnitude with the contrast behavior, we continued with a ROI analysis to investigate their relationship.

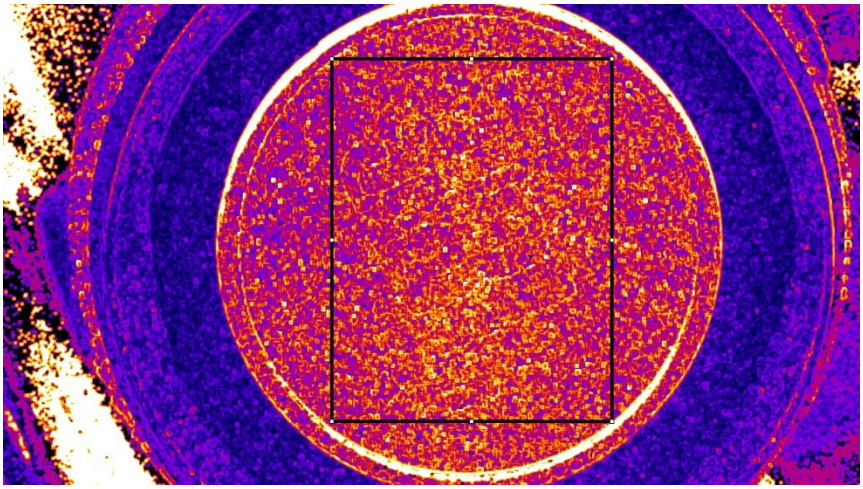

Figure 10.13: ROI selected on the membrane, that starts from point [490,80] with dimensions [420 x 540]

An identical ROI, shown in Figure and covering most of the membrane, was applied in all four contrast maps that are presented in Figure 10.. The stack of 100 contrast maps computed from the 40% input volume video yielded a mean contrast of 130.99 arbitrary units. The 50% input resulted in a mean contrast of 127.33, 60% resulted in 120.79 and the highest input volume 70% in 111.37 arbitrary units.

We observe that the reduction in mean contrast between the first two volume levels is relatively small, compared to the differences between higher input volumes. Specifically, there is a 2.7% decrease between 40% and 50% input, a 5.1% decrease between 50% and 60%, and a more pronounced 7.8% decrease between 60% and 70% input levels.

It clear that as the input volume increases, the mean speckle contrast decreases accordingly, as a result of the more intense vibrations of the membrane. These results confirm that the system can really detect and visualize relative changes in vibrational energy. Even more importantly, this modeling phase achieves the secondary objective set in the previous step, to establish a physical perspective on the contrast ranges that correspond to known oscillation magnitudes. By quantifying how contrast values vary with controlled input levels, this experiment provides a reference for interpreting the magnitude of surface oscillations, effectively bridging the qualitative speckle maps with a semi-quantitative understanding of the underlying physical motion.

10.3 Occlusion Experiments

The resulting maps from the videos captured with our cross-polarized system using an exposure time of 5ms, produced the best visualization of occlusion-reperfusion tests. These velocity maps were notably free of noise with the exception of subtle unintentional movement of the hand. One particular recording was selected as the most visually clear example of velocity maps. The raw speckle video was captured in 1544 x 1040 pixels with a stable frame rate of 60fps.

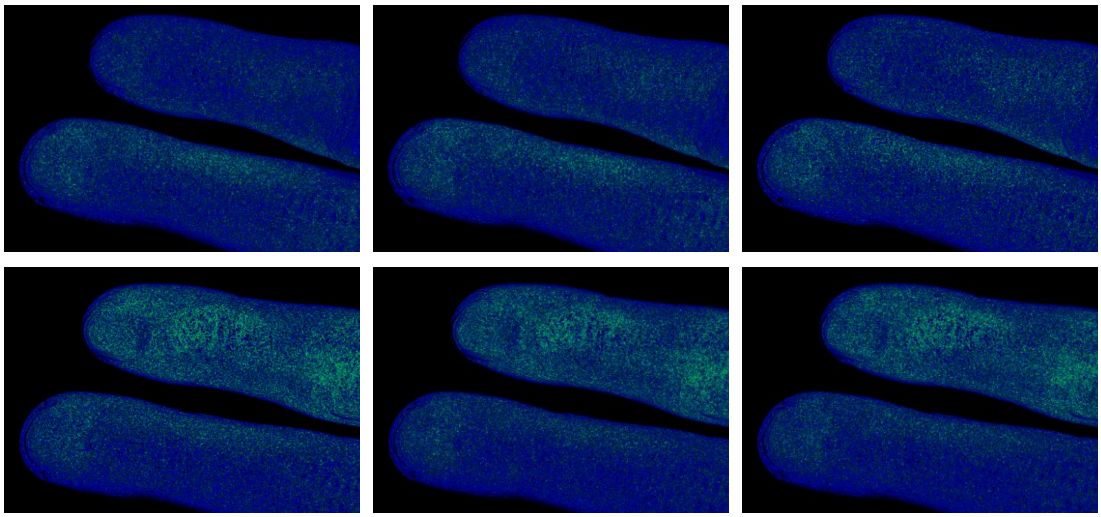

Figure 10.14: A series of four Velocity maps, three consecutive frames captured during occlusion on the upper finger and three during the reperfusion state. Bottom finger was used as baseline.

To illustrate the system's performance during this experimental phase, Figure presents a sequence of representative velocity maps, displayed using a look up table to enhance imaging. Three consecutive frames are included from the occlusion phase and three from the reperfusion. This sequence of frames demonstrates the clear visual difference in flow velocity between the two phases, even to the naked eye. During occlusion, velocity maps show effective flow restriction, while during reperfusion a strong velocity increase is visualized, with respect to the baseline finger. This visual presentation confirms a hyperemic response after the release of the tourniquet and highlights the power and sensitivity of LSCI technique in visualizing perfusion dynamics in skin tissue.

We continue with a presentation of two raw speckle images of the fingers alongside their corresponding velocity maps. This side-by-side presentation provides a clear visual reference, on the way raw speckle patterns translate into the computed velocity maps for each perfusion state, illustrating the system's pipeline, while also demonstrating the quality of the raw data that supports the contrast computation.

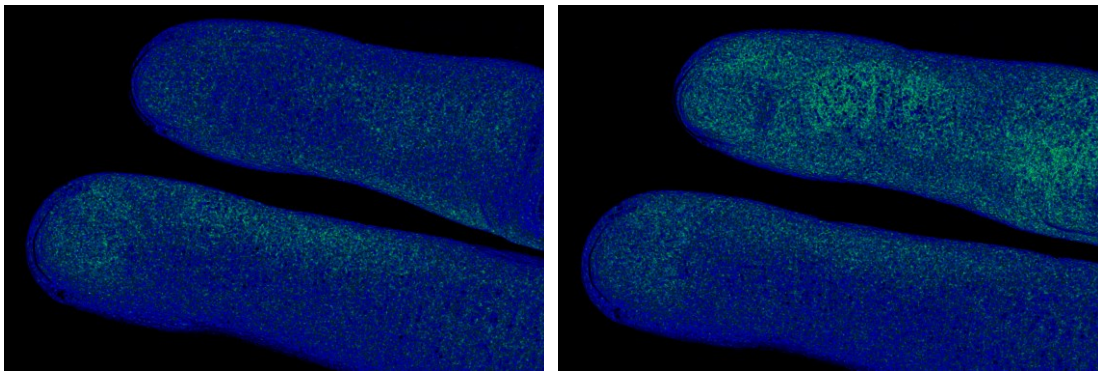

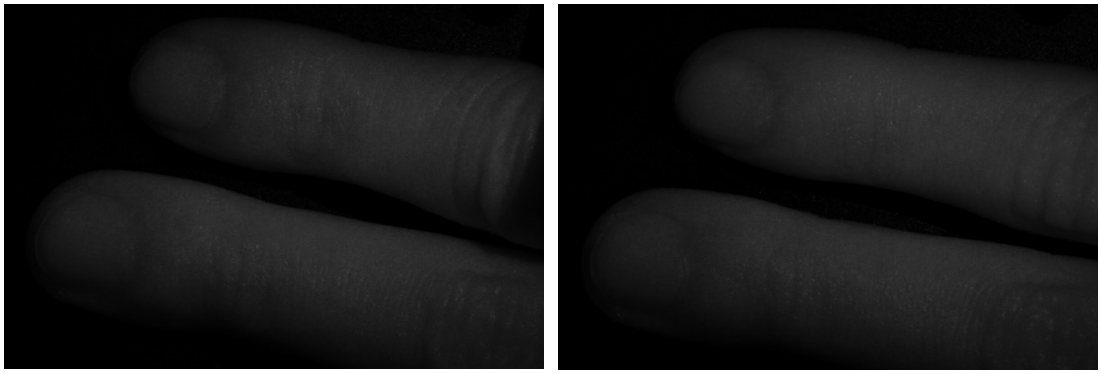

Figure 10.15: Comparison of the raw speckle frames with their corresponding velocity maps. During occlusion of the top finger (left) and Post-occlusion (right)

To further evaluate the LSCI's response to occlusion-reperfusion procedure in a quantitative manner, we continue with a ROI analysis, similar to that used in the drum phase. Mean velocity values were analyzed within a sequence of velocity maps covering both the occlusion phase and the progression of reperfusion after the tourniquet's release. Two ROIs were manually and applied consistently across the entire stack of velocity maps, each focusing on a specific area of the fingers in order to ensure the validity of measuring.

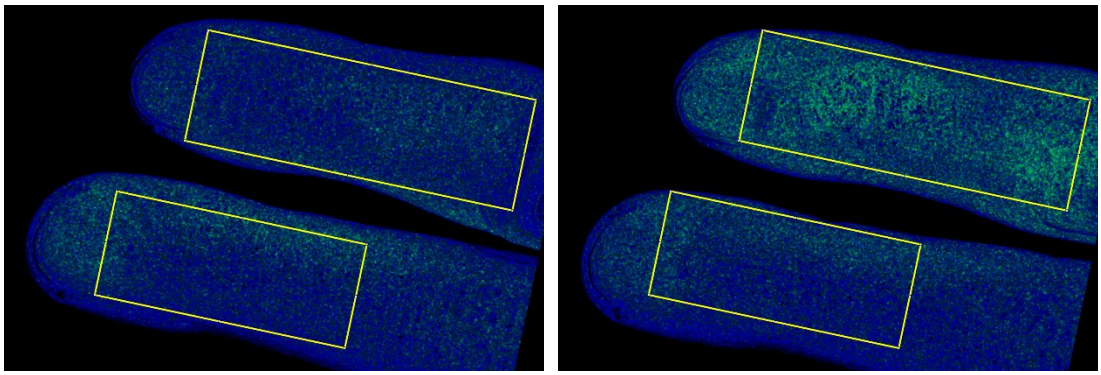

Figure 10.16: ROI of the occluded finger extends from point [490,100] with dimensions [825 x 325] while ROI of the un-occluded finger starts from point [330,620] with dimensions [725 x 300].

The illustrated ROIs were chosen to include the majority of each finger and capture overall velocity trends. In their selection in order to be universal among the two phases, we accounted for minor finger repositioning that occurred during the recording.

The mean contrast values within the ROIs were computed to analyze the temporal evolution of perfusion changes in the regions that are representative of the occluded and non-occluded fingers.

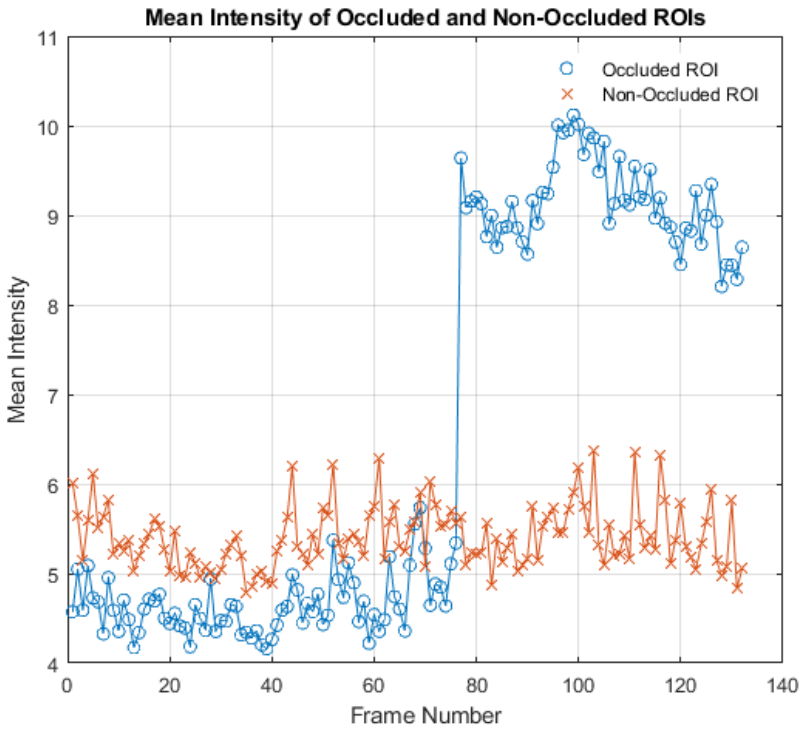

Figure 10.17: Average mean velocities to frame of the 2 selected ROIs during occlusion-reperfusion. Baseline mean velocity from the non-occluded finger is plotted along with the finger undergoing occlusion.

In the figure above, it is apparent that the evolution of reperfusion is not captured in its entirety. Due to practical hardware constraints, continuous recording of the complete reperfusion recovery was not feasible, as longer recordings would have required significantly larger file sizes and computational resources exceeding the RAM of our system. As a result, only the initial phase of the reperfusion process is presented, which is still sufficient to demonstrate the system's performance to physiological perfusion changes following occlusion release.

The non-occluded finger exhibits a consistent mean velocity trend throughout the test which is an initial indication of noise being absent and the system's stability. This ROI has a mean velocity of 5.4056 arbitrary units and a range of [4.7870, 6.3766]. During the occlusion phase, the occluded ROI shows a clear drop in mean velocity compared to baseline, confirming effective flow restriction. The mean velocity, during occlusion is 4.6520, spanning from 4.1593 to 5.7348. This corresponds to almost 14% reduced blood flow with respect to the baseline mean velocity of the non-occluded finger. After the release of the tourniquet, the mean velocity rises sharply, demonstrating a reperfusion response consistent with the expected hyperemia phenomenon. During the reperfusion phase, the finger exhibits a mean velocity ranging from 8.2044 to 10.1184, with a mean value equal to 9.0747 units. This corresponds to a peak to baseline ration of $\frac{10.1184}{5.4056} \cong 187.5\%$. The peak velocity value occurred at frame 99 and was followed by a clear progressive reduction toward the end of the stack. Specifically, from frame 99 to 132, the reperfusion phase shows a steady decline, with the final five frames exhibiting the lowest velocities within the entire reperfusion period, indicating a

return toward the baseline perfusion levels. The minimum velocity recorder was 8.2044 arbitrary units, corresponding to a reduction of 18.9%.

This peak magnitude is consistent with the values reported for healthy subjects in standard post-occlusive reactive hyperemia (PORH) tests, which typically range from 150-250% of baseline perfusion. Specifically, Lamprou et al. [92] reported $189.4 \pm 46.0\%$ peak magnitude while Humeau-Heurtier et al. [93] provided similar occlusion-reperfusion trends, in agreement with the trends of Figure 10.. It should be noted that PORH is a widely used vascular function assessment protocol, employing a calibrated occlusion cuff, and that specific methods and occlusion durations can vary between these studies. Additionally, our experimental procedure differs in several aspects, including the occlusion being performed on the finger, instead of the forearm. PORH, however, is still a relevant benchmark to validate our perfusion measuring system. Finally, the mean velocity drop, observed during the occlusion phase (~14%) aligns closely with the 16% reduction reported by Markwalder et al. [94] for mild forearm occlusion at 60 mmHg, confirming that the local finger band used in this study provides a comparable partial flow restriction. These related results provide a further validation, taken together, for our system's ability to detect physiologically meaningful perfusion changes.

As a final step, a contrast-to-noise (CNR) ratio was computed using the contrast maps, which is an additional, established metric to evaluate the LSCI system. Usually, CNR is defined as the difference between vascular and static tissue regions, normalized by the standard deviation of the static, serving as an objective measure of the visibility of the vasculature. In skin perfusion, vascular maps cannot be obtained, thus in this study we have developed an adaptation of the CNR, tailored for the occlusion-reperfusion application. The metric is computed as the absolute difference between the mean speckle contrast and the baseline contrast, normalized by the baseline standard deviation. This approach follows the same principle of quantifying signal detectability over noise but focuses on the physiological phases being measured rather than spatial vessel–tissue differences. The standard deviation of the baseline phase is related with noise as no physiological change is occurring and the variability comes from random speckle decorrelation and noise.

Two CRN values were computed, one for each phase, occlusion and reperfusion:

$$CNR_{occlusion} = \frac{|\mu_{occlusion} - \mu_{baseline}|}{\sigma_{baseline}} = 1.8749$$

$$CNR_{reperfusion} = \frac{|\mu_{reperfusion} - \mu_{baseline}|}{\sigma_{baseline}} = 7.6081$$

The resulting CNR values confirmed that the contrast variations induced by occlusion and reperfusion were well above the baseline noise level, which corresponds to the natural fluctuation (standard deviation) observed within the baseline contrast.

This final phase of experiments tested the developed LSCI system in the biomedical context. Using a clinical procedure that is established in microvascular activity

assessment, this stage confirmed the efficiency and practical performance of the LSCI system. Performing the occlusion-reperfusion experiment on human fingers we validated the effectiveness of the method on skin perfusion. We detected a relative perfusion reduction during occlusion in respect to the baseline range and a robust hyperemic peak upon reperfusion. The reproducibility of our measurements and their agreement with standard PORH benchmarks further validated the quality and reliability of the system in skin perfusion visualization, revealing a potential for future clinical or experimental work.

Bibliography

[1] H. Messaoudi, S. Eckert and F. Vollertsen, "Thermal Analysis of Laser Chemical Machining: Part I: Static Irradiation," *Materials Sciences and Applications,* vol. 8, no. 10, pp. 685-707, 2017.

[2] C.-Y. Liu, W. Chih-Chiang, T. Li-Chuan, W.-H. Chieng, E.-Y. Chang, C.-Y. Peng and H.-C. Kuo, "Design of High Peak Power Pulsed Laser Diode Driver," *Photonics,* vol. 9, no. 9, 2022.

[3] O. Svelto, Principles of Lasers, Milan, Italy: Springer, 2010.

[4] C. Balas, "3. Laser physics," in *Optoelectronics Course*, Chania, Greece, TUC.

[5] P. W. Milonni and J. H. Eberly, Laser Physics, New Jersey, US: Wiley, 2010.

[6] H. Weber, G. Herziger and R. Poprawe, "Subvolume A: Laser Fundamentals," in *Laser Physics and Applications*, New York, Springer, 2004.

[7] H. Fontelle, "Laser Speckle Imaging: Spatio-Temporal Image Enhancement," Patras, University of Patras, 2009, pp. 27-30.

[8] W. An, Industrial Applications of Speckle Techniques, Stockholm: Royal Institute of Technology , 2002.

[9] M. Sjödahl, "Practical limits and opportunities with speckle metrology," in *The European Physical Journal Conferences 266*, Porto, 2022.

[10] R. Wang, P. Zhou and J. Zhu, "Accurate 3D reconstruction of single-frame speckle-encoded textureless surfaces based on densely connected stereo matching network," *Optics Express,* vol. 31, no. 9, pp. 14048-14067, 2023.

[11] T. Li, Z. Guocheng, Z. Yiming, F. Lin, Z. Shaohui and H. Qun, "Single-shot absolute 3D measurement based on speckle-embedded fringe projection," *Optics and Lasers in Engineering,* vol. 172, 2024.

[12] G. Romero, E. E. Alanis and H. Rabal, "Statistics of the dynamic speckle produced by a rotating diffuser and its application to the assessment of paint drying," *Optical Engineering,* vol. 39, no. 6, pp. 1652-1658, 2000.

[13] A. Federico, G. H. Kaufmann, G. E. Galizzi, H. Rabal, M. Trivi and R. Arizaga, "Simulation of dynamic speckle sequences and its application to the analysis of transient processes," *Optics Communications,* p. 493–499, 2006.

[14] E. Stoykova, D. Nazarova, N. Berberova, A. Gotchev, B. Ivanov and G. Mateev, "Dynamic laser speckle metrology with binarization of speckle patterns," in *International Conference and School on Quantum Electronics "Laser Physics and Applications"*, Eilat, Israel, 2017.

[15] S. A. Semerdzhiev, H. M. van der Kooij, R. Fokkink, J. van der Gucht and J. Sprakel, "Quantifying the Open Time and Film Formation of Waterborne Coatings with Laser Speckle Imaging," *ACS Applied Optical Materials,* vol. 2, no. 5, 2024.

[16] T. F. Begemann, G. Gulker, K. D. Hinsch and K. Wolff, "Corrosion monitoring with speckle correlation," *Applied Optics,* vol. 38, no. 28, p. 5948, 1999.

[17] N. Andrés, S. Recuero, M. P. Arroyo, M. T. Bona, J. M. Andrés and L. A. Angurel, "Fast visualization of corrosion processes using digital speckle photography," *Corrosion Science,* vol. 50, pp. 2965-2971, 2008.

[18] O. Pedram, R. Jamali, V. Abbasian, V. F. Rad and A. Darafsheh, "Evaluation of pitting corrosion by dynamic speckle pattern analysis," *Scientific Reports,* vol. 13, no. 1, 2023.

[19] Y.Z. Dai, A. Kato and F. P. Chiang, "Fatigue monitoring by laser speckle," *International Journal of Fatigue,* vol. 13, no. 3, pp. 227-232 , 1991.

[20] B. V. Farahani, F. Direito, P. J. Sousa, P. J. Tavares and P. M. Moreira, "Electronic Speckle Pattern Interferometry for fatigue crack monitoring," *Procedia Structural Integrity,* vol. 37, p. 873–879, 2022.

[21] M. Kopec, A. Brodecki, D. Kukla and Z. L. Kowalewski, "Suitability of DIC and ESPI optical methods for monitoring fatigue damage development in X10CrMoVNb9-1 power engineering steel," *Archives of Civil and Mechanical Engineering,* vol. 21, no. 4, 2021.

[22] A. V. Osintsev, Y. P. Presnyakov and V. P. Shchepinov, "Application of Correlation Speckle Photography for Measuring Contact Pressures," *Optics and Spectroscopy,* vol. 95, no. 4, pp. 652-657, 2003.

[23] S. Pei, P. Chari, X. Wang, X. Yang, A. Kadambi and Y. Zhang, "ForceSight: Non-Contact Force Sensing with Laser Speckle Imaging," in *35th Annual ACM Symposium on User Interface Software and Technology*, New York, 2022.

[24] S. Shimadera, K. Kitagawa, K. Sagehashi, Y. Miyajima, T. Niiyama and S. Sunada, "Speckle-based high-resolution multimodal soft sensing," *Scientific Reports,* vol. 12, 2022.

[25] A. Oulamara, G. Tribillon and J. Duvernoy, "Biological activity measurement on botanical specimen surfaces using a temporal decorrelation effect of laser speckle," *JOURNAL OF MODERN OPTICS,,* vol. 36, no. 2, pp. 165-179, 1989.

[26] Z. Xu, C. Joenathan and B. M. Khorana, "Temporal and spatial properties of the time-varying speckles of botanical specimens," *Optical Engineering,* vol. 34, no. 5, 1995.

[27] M. Pajuelo, G. Baldwin, H. Rabal, N. Cap, R. Arizaga and M. Trivi, "Bio-speckle assessment of bruising in fruits," *Optics and Lasers in Engineering,* vol. 40, p. 13–24, 2003.

[28] G. F. Rabelo, R. A. Braga Júnior, I. M. D. Fabbro, M. R. Trivi, H. J. Rabal and R. Arizaga, " Laser speckle techniques in quality evaluation of orange fruits," *Revista Brasileira de Engenharia Agrícola e Ambiental,* vol. 9, no. 4, p. 570–575, 2005.

[29] A. Kurenda, A. Adamiak and A. Zdunek, "Temperature effect on apple biospeckle activity evaluated with different indices," *Postharvest ,* vol. 67, pp. 118-123, 2012.

[30] G. G. Romero, A. C. Monaldi, D. O. Dominguez, A. V. Blanc and L. Morana, "Bio-speckle for microalgae growth monitoring in laboratory scale photobioreactor," *ÓPTICA PURA Y APLICADA,* vol. 50, no. 2, pp. 127-133, 2017.

[31] W. Heeman, W. Steenbergen, G. M. van Dam and E. C. Boerma, "Clinical applications of laser speckle contrast imaging: a review," *Journal of biomedical optics,* vol. 24, no. 8, 2019.

[32] J. A. Pomarico, H. O. Di Rocco, L. Alvarez, C. Lanusse, L. Mottier, C. Saumell, R. Arizaga, H. Rabal and M. Trivi, "Speckle interferometry applied to pharmacodynamic studies: evaluation of parasite motility," *European Biophysics Journal,* vol. 33, no. 1, p. 694–699, 2004.

[33] S. E. Murialdo, G. H. Sendra, L. I. Passoni, R. Arizaga, J. F. Gonzalez, H. Rabal and M. Trivi, "Analysis of bacterial chemotactic response using dynamic laser speckle," *Journal of Biomedical Optics,* vol. 14, no. 6, 2009.

[34] I. Balmages, J. Liepins, S. Zolins, D. Bliznuks, R. Broks, I. Lihacova and A. Lihachev, "Tools for classification of growing/non-growing bacterial colonies using laser speckle imaging," *frontiers in microbiology,* vol. 14, no. 1, 2023.

[35] I. Balmages, J. Liepins, E. T. Auzins, D. Bliznuks, E. Baranovics, I. Lihacova and A. Lihachev, "Use of the speckle imaging sub-pixel correlation analysis in revealing a mechanism of microbial colony growth," *Scientific Reports,* vol. 13, no. 1, 2023.

[36] R. Silvennoinen, V. Hyvarinen, P. Raatikainen and K.-E. Peiponen, "Dynamic laser speckle pattern in monitoring of local deformation of tablet surface after compression," *International Journal of Pharmaceutics,* vol. 199, no. 1, pp. 205-208, 2000.

[37] D. D. Postnov, N.-H. Holstein-Rathlou and O. Sosnovtseva, "Laser speckle imaging of intra organ drug distribution," *BIOMEDICAL OPTICS EXPRESS,* vol. 6, no. 12, 2015.

[38] S. A. Pape, C. A. Skouras and P. O. Byrne, "An audit of the use of laser Doppler imaging (LDI) in the assessment of burns of intermediate depth," *Burns,* vol. 27, no. 1, pp. 233-239, 2001.

[39] C. Stewart, R. Frank, K. R. Forrester, J. Tulip, R. Linsday and R. C. Bray, "A comparison of two laser-based methods for determination of burn scar perfusion: Laser Doppler versus laser speckle imaging," *Burns,* vol. 31, no. 1, pp. 744-752, 2005.

[40] C. Crouzet, J. Q. Nguyen, A. Ponticorvo, N. P. Bernal, A. J. Durkin and B. Choi, "Acute discrimination between superficial-partial and deep-partial thickness burns in a

preclinical model with laser speckle imaging," *Burns,* vol. 41, no. 1, pp. 1058-1063, 2015.

[41] F. Lindahl, E. Tesselaar and F. Sjolberg, "Assessing paediatric scald injuries using Laser Speckle Contrast Imaging," *Burns,* vol. 39, no. 1, pp. 662-666, 2013.

[42] R. Mirdell, S. Farnebo, F. Sjoberg and E. Tesselaar, "Accuracy of laser speckle contrast imaging in the assessment of pediatric scald wounds," *Burns,* vol. 44, no. 1, pp. 90-98, 2018.

[43] K. Zheng, E. Middelkoop, M. Stoop, P. van Zuijlen and A. Pijpe , "Validity of laser speckle contrast imaging for the prediction of bourn wound healing potential," *Burns,* vol. 48, no. 1, pp. 319-327, 2022.

[44] B. Ruaro, A. Sulli, V. Smith, S. Paolino, C. Pizzorni and M. Cutolo, "Short-term follow-up of digital ulcers by laser speckle contrast analysis in systemic sclerosis patients," *Microvascular Research ,* vol. 101, no. 1, pp. 82-85, 2015.

[45] T. M. v. Vuuren, C. Van Zandvoort, S. Doganci, I. Zwiers, A. J. tenCate-Hoek, R. L. Kurstjens and C. H. Wittens, "Prediction of venous wound healing," *Phlebology,* vol. 32, no. 10, pp. 658-664, 2017.

[46] O. A. Mennes, J. J. van Netten, J. G. van Baal and W. Steenbergen, "Assessment of microcirculation in the diabetic foot with laser speckle contrast imaging," *Physiological Measurement,* vol. 40, no. 1, 2019.

[47] O. A. Mennes, M. Selles, J. J. van Netten, J. G. van Baal, W. Steenbergen and R. H. J. A. Slart, "Semi-Automatic Tracking of Laser Speckle Contrast Images of Microcirculation in Diabetic Foot Ulcers," *Diagnostics,* vol. 10, no. 1, 2020.

[48] M.-C. Hsieh, C.-Y. Chang, C.-H. Hsu, Y.-R. Lin, P.-Y. Hsieh, C. T.-S. Ching and L.-D. Liao, "Improvement of clinical wound microcirculation diagnosis using an object tracking-based laserspeckle contrast imaging system," *APL Bioengineering,* vol. 8, no. 1, 2023.

[49] K. Long, J. Liu, S. Shen, M. Thong, D. Wang and N. hen, "Light-sheet laser speckle imaging for cilia motility assessment," *Computational and Structural Biotechnology Journal,* vol. 21, no. 1, pp. 1661-1669, 2023.

[50] C. M. Waterman-Storer, A. Desai, J. C. Bulinski and E. Salmon, "Fluorescent speckle microscopy, a method to visualize the dynamics of protein assemblies in living cells," *Current Biology,* vol. 8, no. 1, pp. 1227-1230, 1998.

[51] D. Dormann and C. J. Weijer, "Imaging of cell migration," *EMBO Journal,* vol. 25, p. 3480–3493, 2006.

[52] S. Yamashiro and N. Watanabe, "Overview of Single-Molecule Speckle (SiMS) Microscopy and Its Electroporation-Based Version with Efficient Labeling and Improved patiotemporal Resolution," *Sensors,* vol. 17, p. 1585, 2017.

[53] K. A. Powers and A. S. Dhamoon, "Physiology, Pulmonary Ventilation and Perfusion," in *StatPearls [Internet]*, Treasure Island (FL), StatPearls Publishing, 2023.

[54] N. Charkoudian, "Skin Blood Flow in Adult Human Thermoregulation: How It Works, When It Does Not, and Why," *Mayo clinic proceedings,* vol. 78, no. 5, pp. 603-612, 2003.

[55] D. Matienzo and B. Bordoni, "Anatomy, Blood Flow," in *StatPearls [Internet]*, Treasure Island (FL), StatPearls Publishing, 2023.

[56] L. Østergaard, "Blood flow, capillary transit times, and tissue oxygenation: the centennial of capillary recruitment," *Journal of Applied Physiology,* vol. 129, p. 1413–1421, 2020.

[57] C. A. d. Uil, E. Klijn, W. K. Lagrand, J. J. Brugts, C. Ince, P. E. Spronk and M. L. Simoons, "The Microcirculation in Health and Critical Disease," *Progress in Cardiovascular Diseases,* vol. 51, no. 2, pp. 161-170, 2008.

[58] P. G. Camici and O. E. Rimoldi, "The Clinical Value of Myocardial Blood Flow Measurement," *THE JOURNAL OF NUCLEAR MEDICINE,* vol. 50, no. 7, pp. 1076-1087, 2009.

[59] J. Demeestere, A. Wouters, S. Christensen, R. Lemmens and M. G. Lansberg, "Review of Perfusion Imaging in Acute Ischemic Stroke From Time to Tissue," *Stroke,* vol. 51, no. 3, pp. 1017-1024, 2020.

[60] J. M. Falotico, K. Shinozaki, K. Saeki and L. B. Becker, "Advances in the Approaches Using Peripheral Perfusion for Monitoring Hemodynamic Status," *Frontiers in Medicine,* vol. 7, no. 1, 2020.

[61] J. V. Berggren, M. Stridh and M. Malmsjö, "Perfusion Monitoring During Oculoplastic Reconstructive Surgery: A Comprehensive Review," *Ophthalmic Plast Reconstr Surg,* vol. 38, no. 6, pp. 522-534, 2022.

[62] B. Li, Y. Dai, W. Cai, M. Sun and J. Sun, "Monitoring of perioperative tissue perfusion and impact on patient outcomes," *Journal of Cardiothoracic Surgery,* vol. 20, pp. 1-8, 2025.

[63] J. a. K and S. Narayanan, "MEASURING BLOOD FLOW: TECHNIQUES AND APPLICATIONS-A REVIEW," *International Journal of Recent Research and Applied Studies,* vol. 6, no. 2, pp. 203-216, 2011.

[64] K. F. Ma, S. F. Kleiss, R. C. Schuurmann, R. P. Bokkers, Ç. Ünlü and J.-P. P. De Vries, "A systematic review of diagnostic techniques to determine tissue perfusion in patients withperipheral arterial disease," *EXPERT REVIEW OF MEDICAL DEVICES,* vol. 16, no. 8, pp. 697-710, 2019.

[65] J. W. Goodman, "Statistical properties of laser speckle patterns," in *Laser Speckle and Related Phenomena*, Heidelberg, Springer Berlin, 1975, pp. 9-75.

[66] D. Briers, D. D. Duncan, E. Hirst, S. J. Kirkpatrick, M. Larsson, W. Steenbergen, T. Stromberg and b. ThompsonoLIBER, "Laser speckle contrast imaging: Theoretical and practical limitations," *Journal of Biomedical Optics,* vol. 6, no. 18, pp. 4-5, 2013.

[67] J. W. Goodman, in *Some effects of target-induced scintillations on optical radar performance*, IEEE, 1965, p. 1688–1700.

[68] D. D. Duncan and S. J. Kirkpatrick, "Can laser speckle flowmetry be made a quantitative tool?," *Journal of the Optical Society of America,* vol. 25, no. 8, pp. 2088-2094, 2008.

[69] J. W. Goodman, Statistical Optics, New York: Wiley & Sons, 1985.

[70] H. Cheng and T. Q. Duong, "Simplified laser-speckle-imaging analysis method and its application to retinal blood flow imaging," *Optics Letters,* vol. 32, no. 15, pp. 2188-2190, 2007.

[71] A. Fercher and J. Briers, "Flow visualization by means of single-exposure speckle photography," *OPTICS COMMUNICATIONS,* vol. 37, no. 5, 1981.

[72] D. Briers and S. Webster, "Laser Speckle Contrast Analysis (Lasca): A Nonscanning, Full-Field Technique For Monitoring Capillary Blood Flow," *JOURNAL OF BIOMEDICAL OPTICS,* vol. 1, no. 2, 1996.

[73] S. YORDANOV, M. DRUCKER, H.-J. BUTT and K. KOYNOV, "Real-time monitoring of biomechanical activity in aphids by laser speckle contrast imaging," *Optics Express,* vol. 29, no. 18, pp. 28461-28480, 2021.

[74] H. Cheng, Q. Luo, S. Zeng, S. Chen, J. Cen and H. Gong, "Modified laser speckle imaging method with improved spatial resolution," *Journal of Biomedical Optics,* vol. 8, no. 3, p. 559–564, 2003.

[75] P. Li, S. Ni, S. Zeng and Q. Luo, "Imaging cerebral blood flow through the intact rat skull with temporal laser speckle imaging," *Optics Letters,* vol. 31, no. 12, pp. 1824-1826, 2006.

[76] Y. K. Tan, W. Z. Liu, Y. S. Yew, S. H. Ong and J. P. Suresh, "Speckle image analysis of cortical blood flow and perfusion using temporally derived contrasts," in *Proceedings / ICIP ... International Conference on Image Processing*, Singapore, 2004.

[77] N. KONISHI, Y. TOKIMOTO, K. KOHRA and H. FUJII , "New Laser Speckle FIOWgraphy System Using CCD Camera," *OPTICAL REVIEW,* vol. 9, no. 4, pp. 163-169, 2002.

[78] A. B. Parthasarathy, J. W. Tom, A. Gopal, X. Zhang and A. K. Dunn, "Robust flow measurement with multi-exposure speckle imaging," *Ptics Express,* vol. 16, no. 3, 2008.

[79] A. Rege, J. Senarathna, N. Li and N. V. Thakor, "Anisotropic Processing of Laser Speckle Images," *IEEE TRANSACTIONS ONBIOMEDICALENGINEERING,* vol. 59, no. 5, pp. 1272-1280, 2012.

[80] C. E. Perez-Corona, H. Peregrina-Barreto, J. Rangel-Magdaleno, R. Ramos-Garcia and J. C. Ramirez-San-Juan, "Space-directional Laser Speckle Contrast Imaging to Improve

Blood Vessels Visualization," in *2018 IEEE International Instrumentation and Measurement Technology Conference*, Houston, TX, USA, 2018.

[81] C. E. Perez-Corona, . H. Peregrina-Barreto and J. C. Ramirez-San-Juan, "Space-directional approach to improve blood vessel visualization and temporal resolution in laser speckle contrast imaging," *Journal of Biomedical Optics,* vol. 25, no. 3, 2019.

[82] G. Han, D. Li, J. Wang, Q. Guo, J. Yuan, R. Chen, J. Wang, H. Wang and J. Zhang, "Adaptive window space direction laser speckle contrast imaging to improve vascular visualization," *Biomedical Optics Express,* vol. 14, no. 6, pp. 3086-3099, 2023.

[83] D. Briers, . G. J. Richards and . X.-W. He, "Capillary blood flow monitoring using laser speckle contrast analysis (LASCA)," *Journal of Biomedical Optics,* vol. 4, no. 1, 1999.

[84] S. Yuan, A. Devor, D. A. Boas and A. K. Dunn, "Determination of optimal exposure time for imaging of blood flow changes with laser speckle contrast imaging," *Applied Optics,* vol. 44, no. 10, 2005.

[85] A. C. Volker, P. Zakharov, B. Weber and F. Scheffold, "Laser speckle imaging with an active noise," *Optics Express,* vol. 13, no. 24, 2005.

[86] J. Wang, D. Zhu, M. Chen and X. Liu, "ASSESSMENT OF OPTICAL CLEARING INDUCED IMPROVEMENT OF LASER SPECKLE CONTRAST IMAGING," *Journal of Innovative Optical Health Sciences,* vol. 3, no. 3, p. 159–167, 2010.

[87] J. Wang, R. Shi, Y. Zhang and D. Zhu, "Ear skin optical clearing for improving blood flow imaging," *Photonics and Lasers in Medicine,* vol. 2, no. 1, p. 37–44, 2013.

[88] J. Wang, R. Shi and D. Zhu, "Switchable skin window induced by optical clearing method for dermal blood flow imaging," *Journal of Biomedical Optics,* vol. 18, no. 6, 2013.

[89] R. Shin, M. Chen, V. V. Tuchin and D. Zhu, "Accessing to arteriovenous blood flow dynamics response using combined laser speckle contrast imaging and skin optical clearing," *BIOMEDICAL OPTICS EXPRESS,* vol. 6, no. 6, 2015.

[90] S. Yordanov, "LSCI," 2023. [Online]. Available: https://github.com/stoyan-yordanov/LSCI. [Accessed 2025].

[91] S. Brezas, E. Kaselouris, Y. Orphanos, M. Tatarakis, M. Bakarezos, A. N. Papadogiannis and V. Dimitriou, "Vibrational Analysis of a Splash Cymbal by Experimental Measurements and Parametric CAD-FEM Simulations," *Vibration,* vol. 7, no. 1, pp. 146-160, 2024.

[92] S. Lamprou, N. Koletsos, I. Zografou and A. Lazaridis, "Skin Microvascular Dysfunction in Type 2 Diabetes Mellitus Using Laser Speckle Contrast Analysis and Association with Carotid Intima-Media Thickness," *Journal of Clinical Medicine,* vol. 13, no. 16, 2024.

[93] Humeau-Heurtier, P. Abraham, S. Durand and G. Mahe, "Excellent inter- and intra-observer reproducibility of microvascular tests using laser speckle contrast imaging," *Clinical hemorheology and microcirculation,* vol. 58, 2013.

[94] L. Markwalder, R. Gush, F. Khan, C. E. Murdoch and N. Krstajić, "In vivo laser speckle contrast imaging of microvascular blood perfusion using a chip-on-tip camera," *iScience,* vol. 27, no. 3, 2024.